UNIVERSITY OF OKLAHOMA

GRADUATE COLLEGE

STUDIES OF COSMIC RAYS AND MINIMUM BIAS MEASUREMENTS IN PROTON-PROTON COLLISIONS AT $\sqrt{s} = 0.9$ and 7 TeV WITH THE ATLAS DETECTOR AT THE LHC

A DISSERTATION

SUBMITTED TO THE GRADUATE FACULTY

in partial fulfillment of the requirements for the

Degree of

DOCTOR OF PHILOSOPHY

By

MOHAMED RAZZAK M MEERA LEBBAI
Norman, Oklahoma
2011

STUDIES OF COSMIC RAYS AND MINIMUM BIAS MEASUREMENTS IN PROTON-PROTON COLLISIONS AT $\sqrt{s} = 0.9$ and 7 TeV WITH THE ATLAS DETECTOR AT THE LHC

A DISSERTATION APPROVED FOR THE HOMER L. DODGE DEPARTMENT OF PHYSICS AND ASTRONOMY

BY

Dr. Patrick Skubic, Chair

Dr. Deborah Trytten

Dr. Braden Abbott

Dr. Phillip Gutierrez

Dr. Richard Henry

Dr. Ronald Kantowski

Contents

List of Tables

List of Figures

Abstract

The first measurement of lower momentum charged particle multiplicities made by the ATLAS experiment at the LHC are presented. The charged particle multiplicities are measured as a function of transverse momentum, pseudorapidity, and charged particle multiplicity. These measurements are made in three different phase-space regions of at least two charged particles in the kinematic range of $|\eta| < 2.5$ and $p_{\mathrm{T}} > 100$ MeV, at least one charged particle in the kinematic range of $|\eta| < 2.5$ and $p_{\mathrm{T}} >$500 MeV, and at least six charged particles in the kinematic range of $|\eta| < 2.5$ and $p_{\mathrm{T}} > 500$ MeV. The relation between average transverse momentum and pseudorapidity with charged particle multiplicity are also measured. Two different center-of-mass energies, 0.9 TeV and 7 TeV, are used to measure the charged particle multiplicities. The measured distributions are compared to predictions from Monte Carlo models. All the Monte Carlo models predict the charged particle multiplicity lower than the measured in all three phase-space regions. Using these results, the Monte Carlo models are updated, and the updated models predict a better description of properties of charged particles at the LHC.

Chapter 1

Introduction

Modern day experimental particle physics research studies the nature of fundamental forces and matter. In the current period, the complexity of particle physics experiments has grown rapidly. The world's largest particle accelerator, the Large Hadron Collider (LHC), is built to fulfill the current experimental expectations. The Large Hadron Collider (LHC), at the European Organization for Nuclear Research (CERN) located in Geneva, Switzerland, took more than ten years of hard work by engineers, physicists, and others to record its first collisions.

The first collisions from the LHC were recorded on the 6^{th} December 2009 at a center-of-mass energy of $\sqrt{s} = 0.9$ TeV. Since then, the commissioning of the LHC has progressed continuously. The world's highest energy collisions at the LHC were first recorded on December 13, 2009 at a center-of-mass energy of $\sqrt{s} = 2.36$ TeV (the previous highest energy was $\sqrt{s} = 2.0$ TeV at Fermilab in Batavia, ILL, USA). The first collisions at the center-of-mass energy of $\sqrt{s} = 7$ TeV, the current highest energy in the world, were achieved on March 30, 2010. The LHC is expected to deliver

an integrated luminosity of 100 pb^{-1} $-$ 5fb^{-1} by the end of 2011. There will be several Standard Model physics goals that can be achieved with these high energy beams at the LHC. The LHC era is going to be a very exciting period for high energy physicists.

In order to achieve these goals, the detectors should be understood at an optimum level. The LHC is designed to achieve an instantaneous luminosity of 10^{34} $cm^{-2}s^{-1}$ at its nominal center-of-mass energy of 14 TeV and it has an interaction rate of 40 MHz. Most of these interactions are soft which is described as Minimum Bias events (MB).

The soft interactions, minimum bias events, cannot be explained by the perturbative theory of Quantum Chromodynamics (QCD) since the perturbative theory fails for higher QCD coupling constant (low momentum transfer will have bigger QCD coupling constant). Furthermore, there is no proper phenomenological explanations for non-perturbative processes such as soft QCD interactions (Minimum Bias events).

Yet, it is extremely important to understand the detector response to these events in order to search for higher transverse momentum physics. Therefore, the parameters in the current phenomenological models, PYTHIA and PHOJET, must be tuned to experimental data in order to simulate and hopefully understand the non-perturbative QCD processes. The measurements of basic properties of charged particles from minimum bias events will be the main topic of this thesis.

The charged particle multiplicities, the number of primary charged hadrons from an event, are basic observables from hadron-hadron high energy collisions. Charged particles with small momentum transfer (soft interaction), are directly produced in a

pp interactions. These soft interactions lack robust Monte Carlo theoretical predictions. In the ATLAS experiment at the LHC, the charged particle multiplicities were measured using two different thresholds for transverse momenta (p_{T}) and for three different center-of-mass energies. The previous analyses [1], [2] are measured with the threshold of $p_{\mathrm{T}} \geq 500$ MeV, and the second analysis was carried out with the transverse momentum threshold of 100 MeV.

This dissertation mainly discusses the charged particle multiplicity measurements, with $p_{\mathrm{T}} \geq 100$ MeV with the ATLAS detector for two different center-of-mass energies of $\sqrt{s} = 0.9$ and 7 TeV.

Since a large number of particles are produced at very low transverse momentum, it is very important to detect them with as low a transverse momentum as possible. Charged particle multiplicities consist of four different distributions: the charged particle multiplicity, the multiplicity as a function of pseudorapidity, the multiplicity as a function of the transverse momentum, and the average transverse momentum as a function of the multiplicity. There are several corrections that were measured during the charged particle measurements such as the reconstruction efficiency of charged particles using the Monte Carlo simulation, trigger efficiency, non-primary particles, etc. The corresponding systematic uncertainties were also measured. Three different selections are discussed by varying cuts on both transverse momentum and the number of charged particles per event.

In addition to the charged particle multiplicity measurements, the detection efficiency of the pixel detector using the sensor overlap region with cosmic rays and pixel commissioning are also discussed in this dissertation. The detection efficiency of the

ATLAS pixel detector in the overlap region is consistent with the detection efficiencies of the pixel detector using whole detector volume [3]. The final detection efficiencies of the pixel detector in the overlap region for magnetic field ON and magnetic filed OFF were measured to be:

$(99.746 \pm 0.0438(\text{sta}) \pm 0.0654(\text{sys}))\%$ and $(99.738 \pm 0.0251\ (\text{stat}) \pm 0.0110(\text{sys}))\%$ respectively.

The charged particle multiplicity per event and unit of pseudorapidity at $\eta = 0$, for tracks with $p_{\text{T}} > 100$ MeV is measured to be [4]:

$3.483 \pm 0.009\ (\text{stat}) \pm 0.106\ (\text{syst})$ at $\sqrt{s} = 0.9$ TeV and

$5.630 \pm 0.003\ (\text{stat}) \pm 0.169\ (\text{syst})$ at $\sqrt{s} = 7$ TeV.

This is the first ATLAS measurement of charged particle multiplicities with low transverse momentum threshold and the first published results at a center-of-mass energy of 7 TeV. The results show that phenomenological models, PYTHIA and PHOJET, predict the charged particle multiplicities to be lower than the data. These results provide a very crucial input to tune the Monte Carlo phenomenological models in these kinematic regions.

Chapter 2

Standard Model Theory

2.1 Standard Model

The Standard Model of Particle Physics (SM) is a broadly accepted theory which describes all known elementary particles and their interactions. This model mainly relies on two major factors such as matter and the forces which can be explained accurately by quantum fields. The constituents of matter are called spin 1/2 fermions [5]. The fermions can be subdivided into quarks, which carry color charge and leptons. The fermions are arranged into three different groups or generations according to their quantum numbers. These groups of generations are also known as "families," and each generation contains two quarks, an up-type and a down-type, and two leptons, charged and neutral. Figure 2.1 shows us the three groups of generations of the up-type quarks (with electric charge of +2/3) and down-type (with electric charge of -1/3), as well as charged and neutral leptons.

The first generation of fermions contains the up quark, down quark, electron

and electron neutrino (u,d,e,ν_e). The second generation of fermions contains the charm quark, strange quark, muon and muon neutrino (c,s,μ, ν_μ) while the third generation of fermions contains the top quark, bottom quark, tau and tau neutrino (t,b,τ, ν_τ). The masses of these fermions increase with the order of the generation. This mass hierarchy allows for decays from higher to lower order generations of matter particles. Therefore the first order generations of fermions are always stable. Each particle in all generations has a corresponding "antiparticle," with the same mass but opposite quantum charges such as electric charge, baryon number, lepton number, flavor charges, and weak isospin.

There are three fundamental forces in the SM such as the electromagnetic force, the strong force, and the weak force. These forces are mediated through exchange of integer spin (spin-1) bosons. Photons, γ, mediate the electromagnetic force, and the gluons, g, mediate the strong force. Both both photons and gluons are massless. On the other hand, W and Z bosons mediate the weak interactions with correctly predicted masses using the SM [6]. The gravitational force should be mediated by a spin-2 graviton hypothetically, but there is no evidence of existence of the graviton currently. The SM does not explain the gravitational interaction. There is another boson, known as the Higgs, which has never been observed. In the SM, the electroweak Lagrangian cannot be gauge invariant without the existence of massless gauge bosons. In reality, the weak gauge bosons have mass. The Higgs mechanism [7–9] was invoked as a solution to this problem. This spontaneously breaks the symmetry with an electroweak doublet of complex scalar fields. The SM bosons are shown in Figure 2.1 along with the fermions.

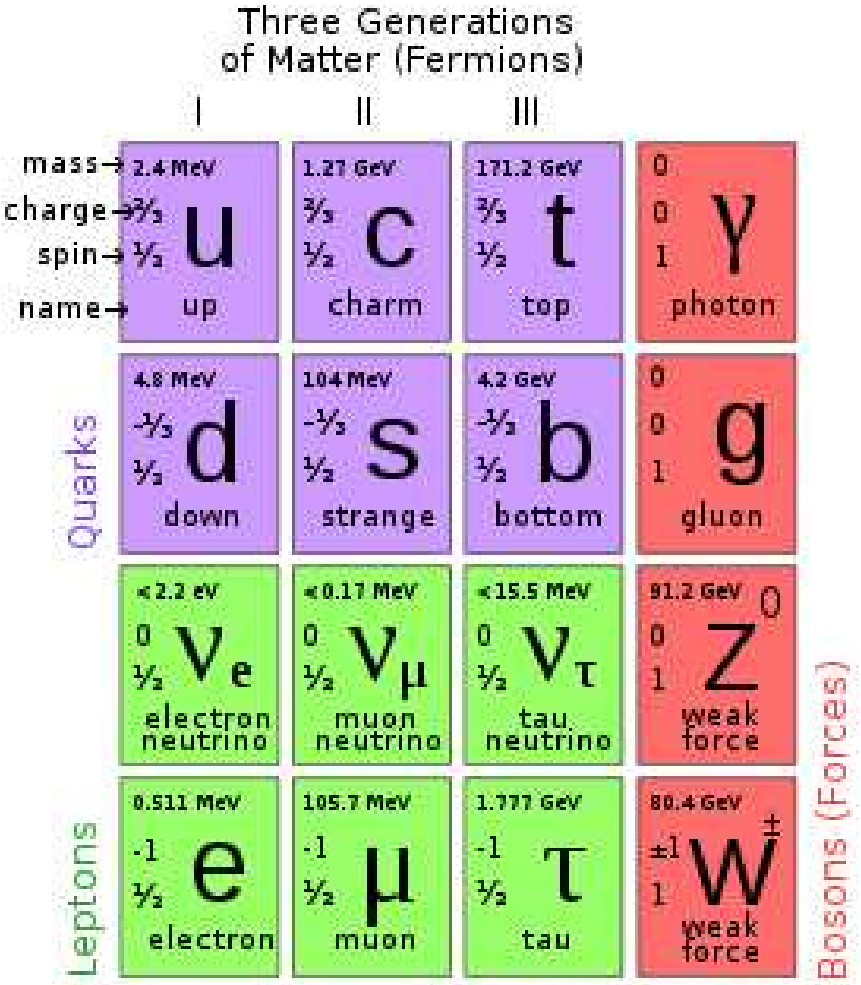

Figure 2.1: Fermions and Bosons

Electroweak	Mass (Gev/c_2)	Electric charge (e)	Hypercharge (e)
Photon(γ)	0	0	0
W bosons ($W^{\pm}$)	80.4	± 1	0
Z bosons ($Z^{\pm}$)	90.1	0	0
Gluon (g)	0	0	0
($Z^{\pm}$)	90.1	0	0

Table 2.1: The electroweak particles and their mass, electric charges and hypercharges.

2.1.1 Electroweak interactions

The electroweak interaction is the unified theory of both electromagnetic and weak interactions. In 1800, Maxwell's equations unified electricity and magnetism. The description of the electromagnetic interaction using quantum field theory is known as Quantum Electrodynamics (QED) [10]. This is the very first quantum field theory employing gauge symmetry.

The weak force is described as changing the flavor of quarks involved in a reaction. The QED and weak interactions, electroweak interactions, is unified using an unbroken $SU(2)_L XU(1)_Y$ theory where SU(2) gauge symmetry applies to the left-handed fermions, and weak isospin T is conserved, which expresses the chiral [1] nature of the fermions. The $U(1)_Y$ is a symmetry which describes the conservation of the *hypercharge*. This electroweak theory introduces the mediators for both weak and electromagnetic interactions that we have discussed in section 2.1. Table 2.1 shows all electroweak particles, their masses, charges and hypercharges. The weak isospin can be calculated by $Y = 2(QT3)$ where T3 is the third component of weak isospin T.

[1] In quantum field theory, chiral symmetry is a possible symmetry of the Lagrangian under which the left handed and right handed parts of Dirac fields transform independently.

2.1.2 Quantum Chromodynamics (QCD) and the Strong Interaction

Quantum Chromodynamics (QCD) is one of the major theories in the SM, in addition to electroweak theory, which describes strong interactions of colored quarks and gluons. This behaves under the SU(3) local non-Abelian gauge transformation symmetry. The new quantum number from QCD, color, forms three color flavors red, green, and blue. These colors transform under the gauge SU(3) group.

The hadrons, baryon and mesons, consist of bound states of three (baryon) and two (meson) quarks and ant-quark, are color singlets even though they have colored quarks because of possible color arrangement. The meson, a bound state of a quark and antiquark ($q\bar{q}$), has a color-anticolor state, and the baryon, a bound state of three quarks (qqq), has three different colors, one for each quark. So the effective color of hadrons becomes colorless. The hadron with its constituents, valance quarks, contains a cloud of virtual quarks and gluons that are known as partons. The models involving partons are known as parton models. The QCD model is good successor of earlier the parton models.

The Lagrangian of QCD for strong interactions is given by Equation (2.1).

$$\mathcal{L}_{\mathcal{QCD}} = \bar{\psi}_j(i\gamma^\mu(D_\mu)_{jk} - m\delta_{jk})\psi_k - \frac{1}{4}F^a_{\mu\nu}F^{\mu\nu}_a \tag{2.1}$$

$$D^\mu_{jk} = \delta_{jk}\partial^\mu + ig(T^a)_{jk}G^\mu_a \tag{2.2}$$

$$F_a^{\mu\nu} = \partial_\mu G_a^\nu + g f_a^{bc} G_b^\mu G_c^\nu \tag{2.3}$$

Where $\forall_{abc} \in [1,8]$ and $\forall_{j,k} \in [1,8]$ represent eight color degrees of freedom of the gluon and three color degrees of freedom of the quark fields respectively.

m is the mass, D_{jk}^μ is the covariant derivative of the quark field (in Equation 2.1), $F_a^{\mu\nu}$ is the field tensor of the spin-1 gluon field, G_a^μ are the SU(3) generations, T^a are the Gell-Mann matrices, and the numbers f_a^{bc} (a,b,c $\in$[1,8]) are the structure constants of the SU(3) group where $[T_a, T_b] = i f_{abc} T^c$. The QCD coupling constant for strong interactions is $\alpha_s \equiv \frac{g^2}{4\pi}$ where the g is the coupling parameter from Equation 2.3. In electroweak interactions, the free particles can be observed but the dynamics of quarks and gluons are different since they are confined inside the bound states. Therefore, a property of QCD is known as *confinement*. The QCD coupling constant, α_s, depends on energy scale, the scale of interactions, as in QED. The leading order running coupling constant is given by:

$$\alpha_s(Q^2) = \frac{12\pi}{(33 - 2n_f) ln(Q^2/\Lambda_{QCD}^2)} \tag{2.4}$$

Where Q^2 is the 4-momentum transferred between the hard scattering partons (interactions with low momentum transfer are known as soft scattering), n_f is the number of quark flavors, and Λ_{QCD}^2 is the QCD normalization scaling factor, when $\alpha_s(Q) \to \infty$ as $Q \to \Lambda$.

In the strong interactions, the coupling constant α_s behaves inversely and decreases with energy (increases with distance). The latest theoretical comparisons of

coupling constant with experimental results are shown in Figure 2.2 [11] . The strong coupling constant is very small at high Q^2, or at low distances. On the other hand, the coupling constant is large when Q^2 is small, or at large distances. Since the coupling constant is very small at high Q^2, the perturbation theory can be used to calculate the QCD interactions. At low Q^2, when the coupling constant is big, the perturbation theory cannot be used.

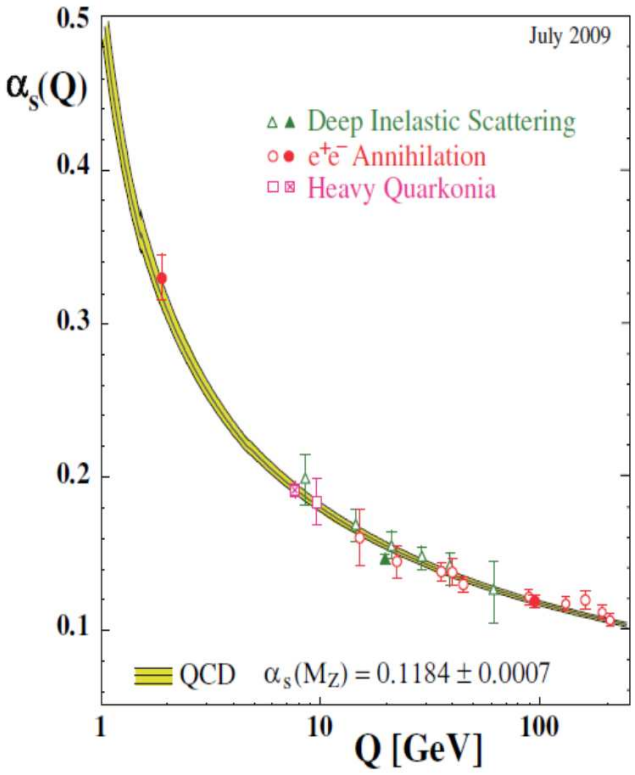

Figure 2.2: Summary of measurements of α_s as a function of the energy scale Q. The curves are QCD predictions for the combined world average value. Full symbols are results based on N3LO QCD, open circles are based on NNLO, open triangles and squares on NLO QCD. The cross-filled square is based on lattice QCD. The filled triangle at Q = 20 GeV (from DIS structure functions) is calculated from the original result which includes data in the energy range from Q =2 to 170 GeV

2.2 Proton-Proton Collisions

Proton-Proton collisions, hadronic collisions, are very complicated since the proton with three quarks and parton constituents changes continuously. Figure 2.3 shows the complication of the proton-proton collisions. At higher energies, as the coupling constant is small, the structure of the proton becomes visible since the interactions fall into perturbative QCD processes. At lower energies, soft scattering, the process is much more complicated. At the LHC, most of the physics interests, such as searches for Higgs and supersymmetry, are involved with higher momentum transfer. Therefore, the high energy physics expectations for the LHC will not be effected due to these extremely complex proton-proton collisions. The particles of interest are not related to the soft parton scattering process responsible for the underlying events. However, understanding the underlying events is a precondition for most of the flagship research topics of the LHC such as the measurement of the properties of the the top quark and searches for new physics.

2.2.1 Total Cross Section and its Components

The total proton-proton cross section (σ_{tot}) at LHC is a sum of the elastic cross section (σ_{elas}), where both protons emerge intact without any additional particle and the inelastic cross section (σ_{inel}), where one of the protons will be destroyed and different particles will be produced. The inelastic interactions can further be divided into three categories such as non-diffractive (ND), single-diffractive (SD), and double-diffractive (DD) interactions. The total cross section of the pp scattering can be written as the

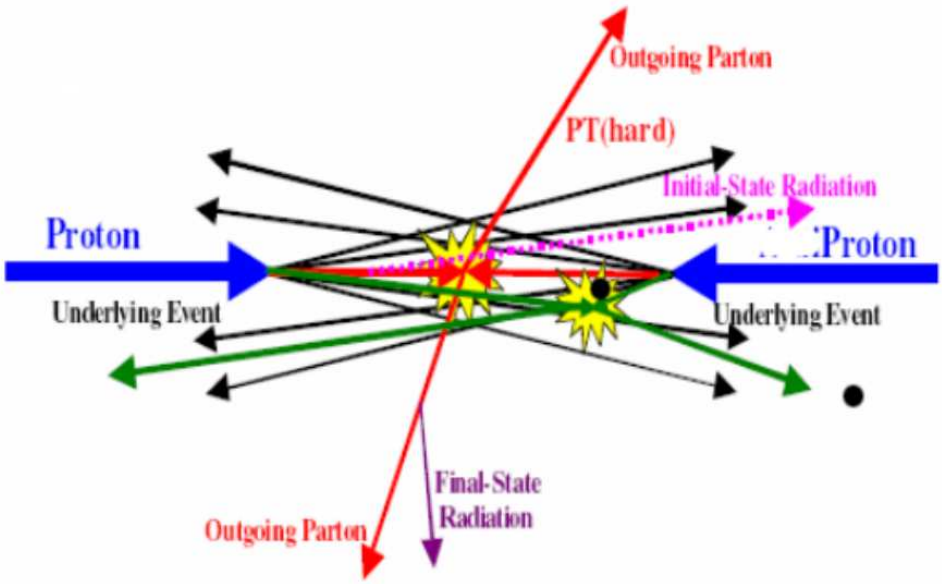

Figure 2.3: The complicated hadron-hadron collision

sum of all the above components as follows:

$$\sigma_{tot} = \sigma_{elas} + \sigma_{nd} + \sigma_{sd} + \sigma_{dd} \tag{2.5}$$

$$\sigma_{inel} = \sigma_{nd} + \sigma_{sd} + \sigma_{dd} \tag{2.6}$$

Figure 2.4 shows the elastic single-diffractive and double-diffractive processes in the phase space of $\phi - \eta$. Figure 2.5 shows the Feynman diagram for non-diffractive interactions. The non-diffractive component comes from color exchange between two protons. In the case of single diffraction , a pomeron (is a Regge trajectory, a family of particles with increasing spin, postulated by Pomeranchuck in 1961 to explain the slowly rising cross section of hadronic collisions at high energies [12]), is exchanged between two protons and one of the protons takes part in diffraction while both incoming protons form a diffractive system.

As we see in the Figures 2.4 and 2.5 each of these three inelastic diffractive events have three different topologies. Since non-diffractive particles are produced by color, exchange large numbers of particles are produced in the central pseudorapidity region. In the case of single diffractive interactions, a large number of particles are produced in the high pseudorapidity forward direction. On the other hand, in the double diffractive events, the particles are produced mostly in both forward and backward pseudorapidity regions and a very small fraction of the particles are produced in the central region. Therefore, the majority of the inelastic cross section comes from the non-diffractive events. Figure 2.6 shows that the majority of the the charged particles

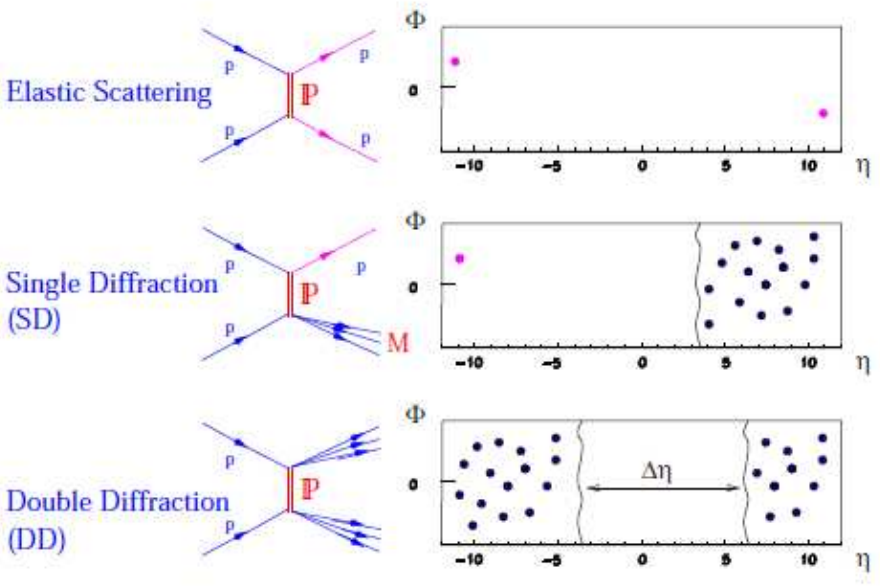

Figure 2.4: The Feynman diagrams and the Schematic view of elastic, single-diffractive and double-diffractive processes in the phase space of $\phi - \eta$

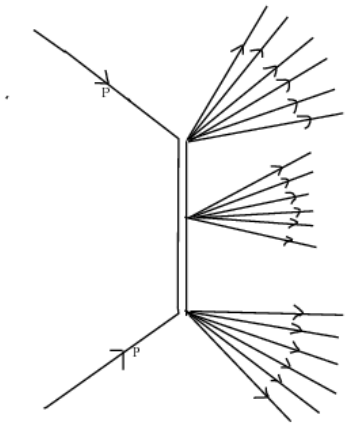

Figure 2.5: The Feynman diagrams for non-diffractive scattering

are coming from non-diffractive events. n_{ch} is the number of charged particles in an event and $\frac{1}{N_{\mathrm{ev}}} \cdot \frac{\mathrm{d}N_{\mathrm{ev}}}{\mathrm{d}n_{\mathrm{ch}}}$ is the charged particle multiplicity distribution where N_{ev} is the number of events, and Nch is the total number of charged particles.

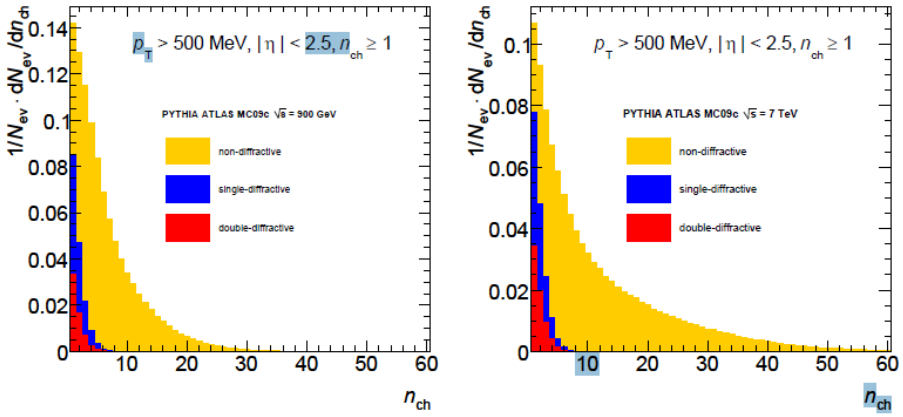

Figure 2.6: Number of charged particle distributions in ATLAS phase space at 900 GeV and 7 TeV split into non-diffractive (light), single-diffractive (dark) and double-diffractive (medium dark) processes.

2.3 Summary

This chapter discusses the standard model theory behind the minimum bias events.

Chapter 3

ATLAS Experiment at LHC

3.1 The Large Hadron Collider

The Large Hadron Collider (LHC) [13] at CERN near Geneva, Switzerland, is the world's newest and most powerful tool for particle physics experiments. It is designed to achieve proton-proton collision at center-of-mass energy of 14 TeV and the unprecedented luminosity of $10^{34}\ cm^{-2}s^{-1}$ once it has been fully commissioned. The first operation started on September 2008 and the current highest center-of-mass energy is 7 TeV.

The Large Hadron Collider (LHC) made of two rings of superconducting hadron accelerator and is installed in the existing 26.7 km tunnel which was used for the Large Electron-Positron (LEP) collider. This tunnel has a total of eight straight sections and eight arcs, and it can have maximum of eight collision points. It has depth ranging from 45 m to 170 m below the ground surface and it is inclined at 1.4% to the vertical sloping towards the Leman lake. All four experiments of LHC,

ATLAS, CMS, ALICE and LHCb, are located at four different collision points out of eight possible points as illustrated in Figure 3.1 [13].

ATLAS and CMS are, newly built, located at point 1 and point 5 respectively while the ALICE and LHCb are located at point 2 and point 8 respectively and they were originally built for LEP. The two large experiments, ATLAS [14] and CMS [15], are mainly designed to search for physics beyond the standard model while the other two experiments are designed for some specific SM research. The ALICE [16] experiment is designed to study the properties of lead-lead ion collisions and LHCb [17] is designed to study physics using bottom quarks. Two proton beams travel in opposite direction around the ring and they will collide at the above four LHC experiment collision points.

To get the highest center-of-mass energy to do the important research on physics beyond the standard model at the LHC, the accelerator must produce collisions at the highest possible energy. The number of events per second is determined by:

$$N_{event} = L\sigma_{event} \tag{3.1}$$

where L is the luminosity of the machine and σ_{event} is event cross section that determines the interaction probability. The luminosity of the accelerator only depends on beam parameters and can be written for a Gaussian beam distribution as:

$$L = \frac{N_b^2 n_b f_{rev} \gamma_\gamma}{4\pi\sigma_x\sigma_y} F \tag{3.2}$$

where

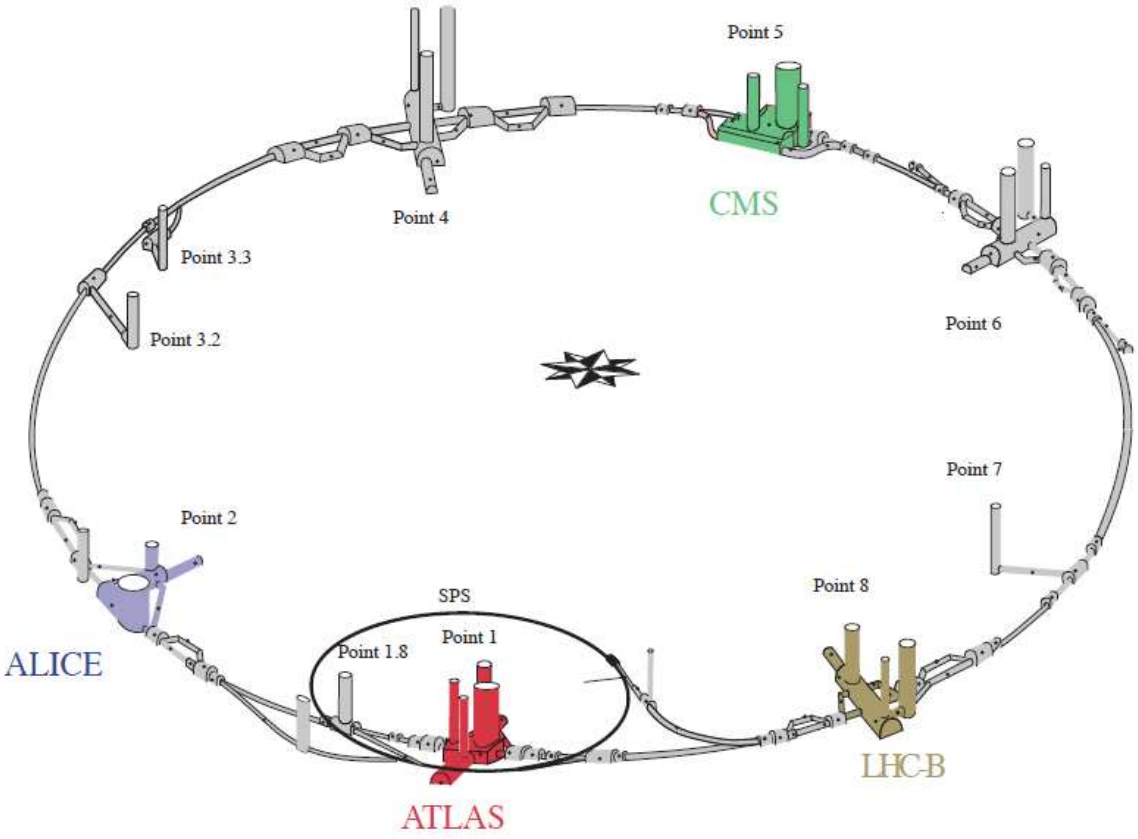

Figure 3.1: Schematic diagram of the Large Hadron Collider (LHC). The four large LHC experiments are located at four different collision points: ATLAS (Point 1), ALICE (Point 2), CMS (Point 5), and LHCb (Point 8) are colored.

- N_b is the number of particle per bunch.
- n_b is the number of bunches per beam.
- f_{rev} is the revolution frequency of the ring.
- γ_γ is the relativistic gamma factor.
- F is the geometric luminosity reduction factor due to the crossing angle at the interaction point.
- σ_x, σ_y characterize the transverse beam profile in the horizontal (bend) and vertical directions.

The large experiments at the LHC, ATLAS and CMS, are aiming to do physics discovery at the peak instantaneous luminosity of $L = 10^{34}$ cm^{-2}s^{-1}. However, at present, the highest luminosity of 1.8×10^{33} cm^{-2}s^{-1} is available at the center-of-mass energy of 7 TeV.

The first proton beam injection in the LHC occurred on September 10, 2008. During this injection, just over a week on September 19, 2008, a number of magnets underwent mechanical damage and a large amount of helium gas was released inside the tunnel due to an electrical bus connection fault between dipole and quadrupole magnets. This incident made more than one year of delay in LHC operation. At the mean time, the damaged magnets were either replaced or repaired.

The LHC's most important moment of first proton-proton collisions were recorded on November 23, 2009 at the center-of-mass energy of 900 GeV. However, the first collision beams were not stable which causes lower data quality. On November 30,

2009, the first stable beam collisions were recorded at $\sqrt{s} = 0.9$ TeV and ran for 10 days. On December 8, 2009, the world's highest collision energy at that time were recorded at the center-of-mass energy of 2.36 TeV. The current world highest center-of-mass energy of 7 TeV collisions were first recorded on March 30, 2010.

3.2 ATLAS Detector

ATLAS (A Toroidal LHC ApparatuS) is, the largest detector of any LHC experiment, a multi-purpose detector designed for a wide range of particle physics studies at the LHC. The detector is a cylindrical in shape with a total length of 44 m and a diameter of 25 m. It has full azimuthal angle coverage and very good pseudorapidity acceptance. The coordinate system of ATLAS is a right-handed coordinate system and is explained in Appendix A.1. A cut-way view of the ATLAS detector is shown in Figure 3.2 [14].

The ATLAS detector is divided into three active sub-detectors systems:

- The **Inner Detector (ID)**: is the innermost sub-detector designed to measure the trajectories of charged particles.
- The **Calorimeter**: measures the energy of particles and jets specially for electromagnetic and hadronic particles. It is built around the Inner Detector.
- The **Muon Spectrometer**: is designed to measure the trajectories of muons.

In addition to these three sub-detectors, there is a magnetic system which is designed to bend the charged particles to measure their momentum. A summary of ATLAS

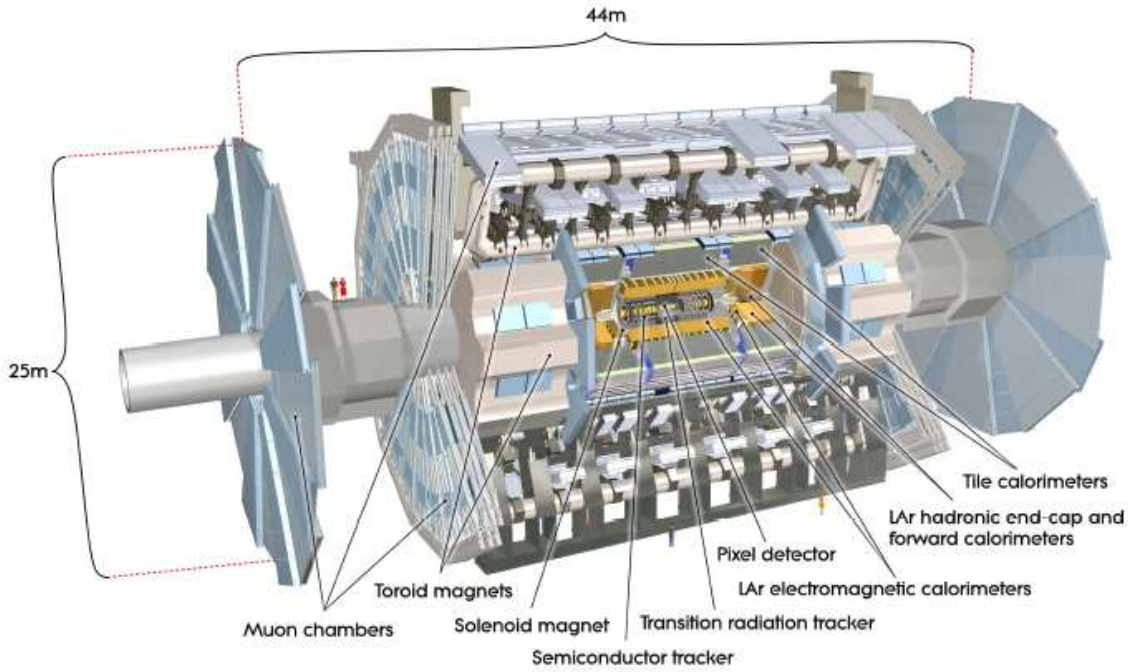

Figure 3.2: The inside view of the ATLAS detector and its components.

detector parameters is given in Table 3.1 [14].

Detector Components	Required Resolution	η coverage	
		Measurements	Trigger
Tracking	$\frac{\sigma_{p_T}}{p_T} = 0.05\%\ p_T \oplus 1\%$	± 2.5	
EM Calorimeter	$\frac{\sigma_E}{E} = 10\%\ \sqrt{E} \oplus 0.7\%$	± 3.2	± 2.5
Hadronic Calorimeter (jets)			
Barrel and end-cap	$\frac{\sigma_E}{E} = 50\%\ \sqrt{E} \oplus 3\%$	± 3.2	± 3.2
forward	$\frac{\sigma_E}{E} = 100\%\ \sqrt{E} \oplus 10\%$	$3.1 < \eta < 4.9$	$3.1 < \eta < 4.9$
Muon Spectrometer	$\frac{\sigma_{p_T}}{p_T} = 10\%\ p_T = 1$ TeV	± 2.7	± 2.4

Table 3.1: General performance goals of the ATLAS detector. Note that, for high-p_T muons, the muon-spectrometer performance is independent of the inner-detector system. The units for E and p_T are in GeV.

3.2.1 The Inner Detector

The Inner Detector (ID) [18,19] is a sub-detector of ATLAS which is closest to the interaction point. The Inner detector reconstructs the trajectories, or tracks, of charged particles that are coming from the collision. Approximately 1000 particles are expected from the collision point every 25 ns within the ID volume of $|\eta|$ <2.5, creating a large track density in the detector [14]. The Inner detector, is a combination of three high resolution tracking sub-detectors, the silicon pixel detector [14,18,19] (pixel), the silicon microstrip detector (SCT) [14, 18, 19], and the Transition Radiation Tracker (TRT) [14,18,19], and is immersed in the central solenoid (CS) magnetic field with 2 T nominal strength. Figure 3.3 [14] shows the cut-view diagram of all sub-detectors of the Inner Detector. Each sub-detector has the highest precision to measure the charge, the momentum, the impact parameters and the track direction. The tracks that are used to study the minimum bias measurements in Chapter 6 were reconstructed using all three components of ID.

3.2.1.1 Pixel Detector

The silicon pixel detector is the innermost layer of the ATLAS experiment tracking system and it provides the highest granularity around the vertex region with significant contribution to the ATLAS track and vertex reconstruction. It contains three barrel layers, concentric with the beam line, and three disks on each side of the endcaps or forward region. Therefore, the pixel detector is able to make at least three measurements per track. Figure 3.4 [14] shows the position of all three barrel layers of pixel detector. The innermost barrel layer is located, from the beamline, at a radius

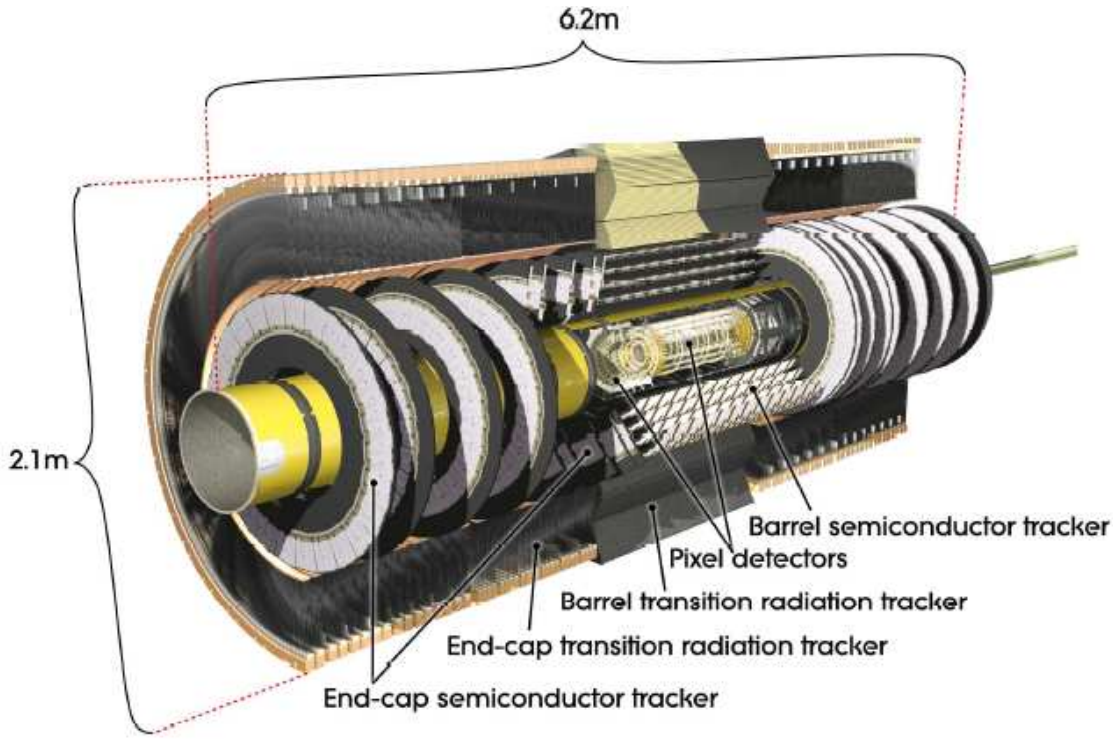

Figure 3.3: The view of the ATLAS inner detector.

of 50.5 mm, and the other two layers are located at radii of 88.5 mm and 122.5 mm respectively. The three disks, on both sides of the end-cap, are located at $|z| = 49.5$ cm, 58.0 cm and 65.0 cm respectively. The pixel detector has a total of 1744 modules, each module has 16 readout chips and more than 46,080 pixels (most of them have a size of 50$\times$ 400 μm).

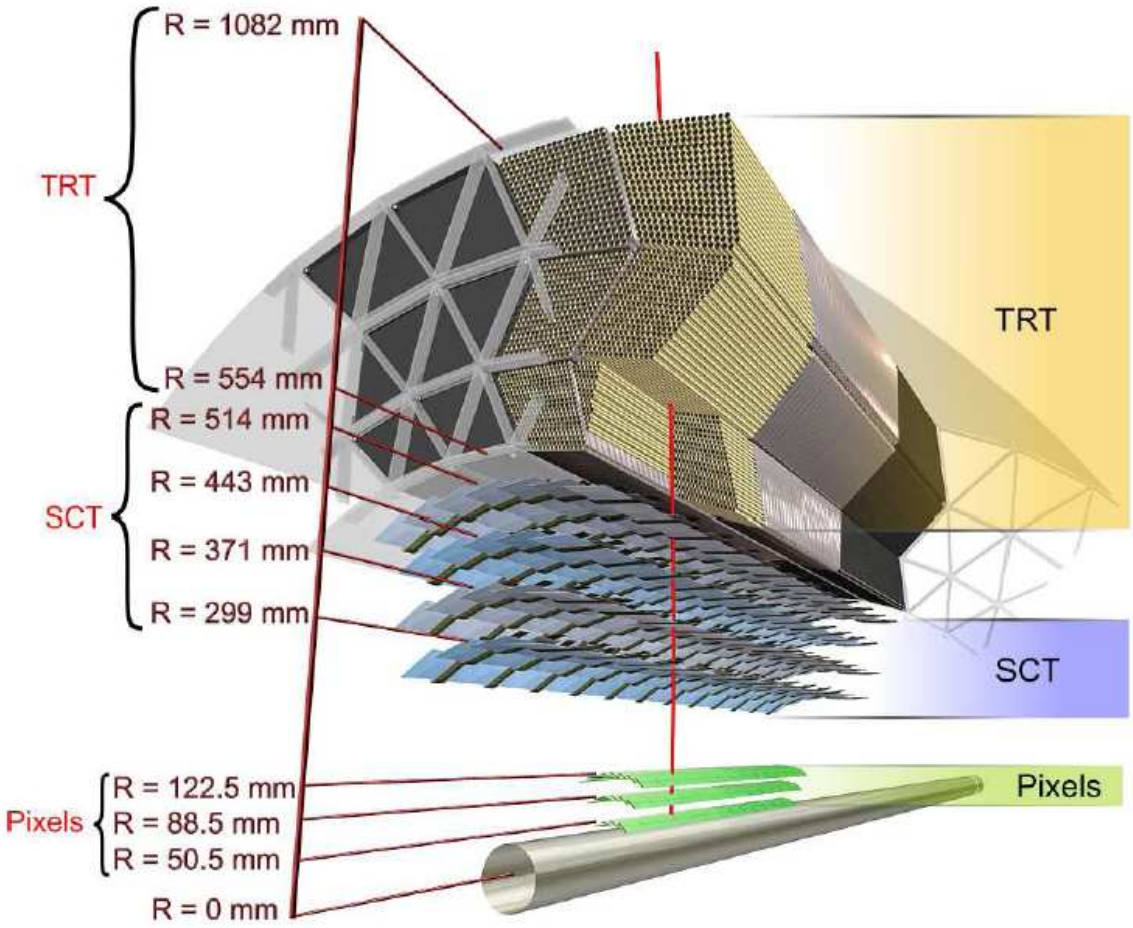

Figure 3.4: The drawing showing the location of all three sub-detector layers.

When the particles pass through the pixel sensor they deposit charge in the pixel sensor. The deposited charge can be measured using pixel readout electronics. The

pixel detector has a total of 80 million readout channels. The pixel detector and it's function are explained more fully in Section 3.3.

3.2.1.2 SCT Detector

The SemiConductor Tracker (SCT) [14, 18], is the middle component of the inner detector, and surrounds the pixel detector. The concept of SCT charge detection is similar to that of the pixel detector but silicon strips (long) are used instead of pixels (small) since the density of the particles decreases as a function of radial distance from the beam line or interaction point. The SCT modules, like the pixel modules, are arranged in cylindrical layers and two end-caps. There are four barrel layers and nine disks in each side of the end-cap. In the barrel region, the SCT module consists of four single sided sensors. Pairs of sensors are configured together to form 12.8 cm long strips with a wedge shape. Two of these wedge shaped pairs of sensors are glued, on a 380 mm thick thermal pyrolitic graphite (TPG) base-board, back-to-back with a small stereo angle of 40 mrad. In the end-cap region, the modules use tapered strips with front-end electronics that is attached to either inner or outer end. SCT has a total of 4088 modules, 2112 modules from the barrel with intrinsic accuracy of 17 μm in $R-\phi$ direction and 580 μm in z direction, 1976 modules from the two end-caps disks with intrinsic accuracy of 17 μm in $R-\phi$ direction and 580 μm in R direction. The SCT has approximately 6.3 million read-out channels. Table 3.2 [14] lists some basic parameters of all three inner detectors.

Item		**Radial Extension (mm)**	**Length (mm)**
Overall ID envelope		$0 < R < 11500$	$< \|z\| < 3512$
Beam Pipe		$29 < R < 36$	
Pixel	**Overall envelope**	$45.5 < R < 242$	$0 < \|z\| < 3092$
3 cylindrical layers	Sensitive barrel	$50.5 < R < 122.5$	$0 < \|z\| < 400.5$
2×3 disks	Sensitive end-cap	$88.8 < R < 149.6$	$495 < \|z\| < 650$
SCT	**Overall envelope**	$255 < R < 549$ (barrel)	$0 < \|z\| < 805$
		$215 < R < 610$ (end-cap)	$810 < \|z\| < 2797$
4 cylindrical layers	Sensitive barrel	$299 < R < 514$ (end-cap)	$0 < \|z\| < 749$
2×9	disks Sensitive end-cap	$275 < R < 560$	$839 < \|z\| < 2735$
TRT	**Overall envelope**	$554 < R < 1082$ (barrel)	$0 < \|z\| < 780$
		$617 < R < 1106$ (end-cap)	$827 < \|z\| < 2744$
73 straw planes	Sensitive barrel	$563 < R < 1066$ (end-cap)	$0 < \|z\| < 712$
160 straw planes	Sensitive end-cap	$644 < R < 1004$	$848 < \|z\| < 2710$

Table 3.2: Major parameters of the inner-detectors.

3.2.1.3 TRT detector

The Transition Radiation Tracker (TRT), is the outermost sub-detector of the inner detector, is divided into barrel and two end-caps like Pixel and SCT , and surrounds the SCT detector. This is the last tracking sub-detector with acceptance of $|\eta|$ <2.0 using 4 mm diameter straw tubes. These tubes, with a gold-plated tungsten wire in the middle, are filled with a non-flammable gas mixture of Xenon(70%), CO_2 (27%) and O_2 (3%). The "straw" tubes are 144 cm in length in the barrel region while 37 cm in length in the end-cap region and arranged radially in the wheel. Therefore, TRT only provides measurements in $R-\phi$ direction and it has a resolution of 130 μm. There are a total of 351,000 TRT channels, with 176 modules, which can typically

provide around 36 measurement points per track, which is very large compared to the other inner sub-detectors' measurements. When the electrons pass through a radiator, polypropylene foils or fibers, between the straws the photons will be created through transition radiation. Since TRT has the ability to give the information only in the $R-\phi$ direction, the reconstruction of tracks must combine with silicon measurements.

3.2.1.4 Calorimeters

Particle and jet energies are measured in the ATLAS detector using calorimeters. The calorimeters can also measure the missing transverse energy from the energy deposited by particles and jets. Calorimeters consist of electromagnetic and hadronic calorimeters which cover a wide range of $|\eta|$ <4.9, using different techniques suited to the widely varying requirements of the physics processes of interest and of the radiation environment over this large η-range [14]. Figure 3.5 shows the cut-way view of the ATLAS Calorimeter system.

3.2.1.4.1 Electromagnet (EM) Calorimeter

EM calorimeters are specifically designed to measure the energy of electrons and photons that interact via the electromagnetic interaction. The EM calorimeter is divided into two segments: a barrel part ($|\eta| < 1.475$) and two end-cap components ($1.375 < |\eta| < 3.2$), within different cryostats. In order to reduce the material effect to achieve excellent calorimeter performance, the central solenoid is located in front of the EM calorimeter so that they both are able to share the space. The barrel part of EM calorimeter is divided into two half barrels at $z = 0$ by a small separation of 4

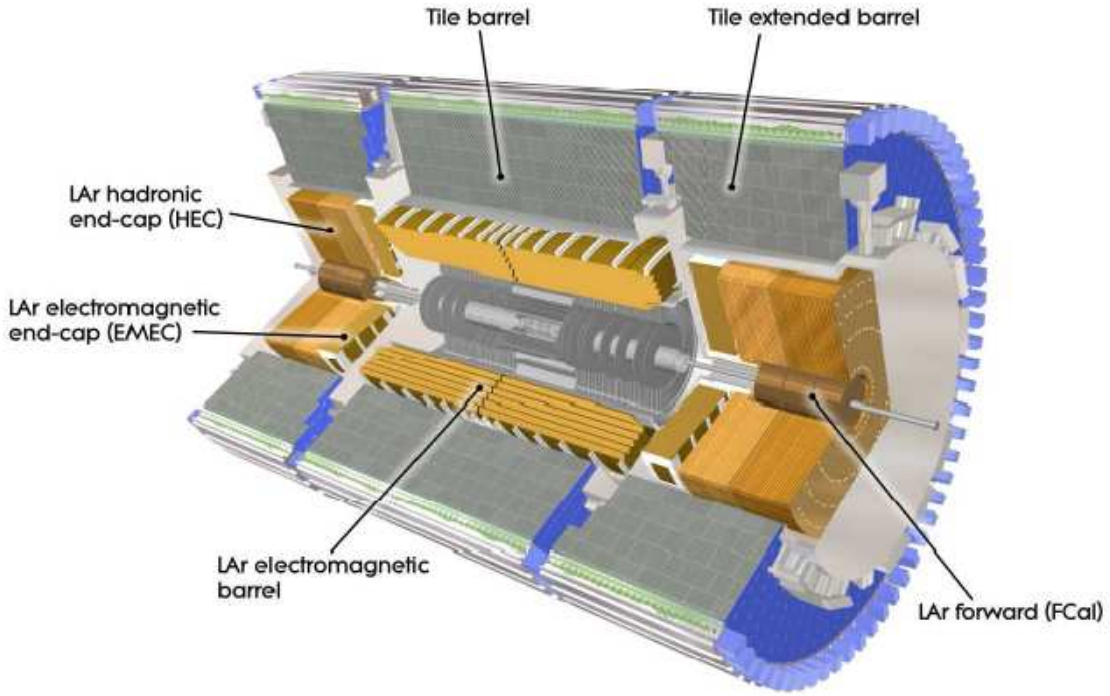

Figure 3.5: The cut-away view of electromagnetic and hadronic (TileCal, HEC and FCAL) components of the ATLAS calorimeter system

mm. The end-cap part further splits into inner wheel in the region of $1.375 < |\eta| < 2.5$ and the outer wheel in the region of $2.5 < |\eta| < 3.2$. The EM calorimeter is a lead and liquid argon calorimeter with an accordion-shape of kapton electrodes and plates of lead absorber. The EM Calorimeter has symmetry of ϕ without azimuthal cracks due to the accordion geometry. The overall thickness of EM calorimeter (a module) is between $22X_0$ and $33X_0$, and is shown in Figure 3.6 [14], where X_0 is the radiation length [1], in the barrel part and between $24X_0$ and $33X_0$ in the end-cap region.

The EM calorimeter is divided into three longitudinal layers or components in terms of samplings or measurements over the range of $|\eta| < 2.5$. The first and innermost region separate the γ/π_0 and e/π. The second layer is designed such that the electrons and photons will lose most of their energies. The last component measures the shower energy that extend past the second compartment to distinguish between electromagnetic and hadronic showers.

3.2.1.4.2 Hadronic Calorimeter (HC)

The hadronic calorimeter [14] is designed to measure particle jets, which are produced from hadronization of quarks and gluons, as well as hadronically-decaying τ-leptons, and missing transverse energy of an event. The ATLAS hadronic calorimeter surrounds the EM calorimeter from the radius 2.28 m to 4.23 m from the beam line. Since the hadronic jets create hadronic showers that are much longer and wider than electromagnetic showers, due to the interaction length [2] λ of hadronic jets that is

[1] The energy deposited in the EM calorimeter is defined by $\mathrm{E} = \mathrm{E}_0 \exp(-x/X_0)$ where X_0 is the radiation length, E_0 is the original energy and x is the thickness of the EM calorimeter module

[2] Interaction length is the length of mean free path of a particle undergoing a strong interaction.

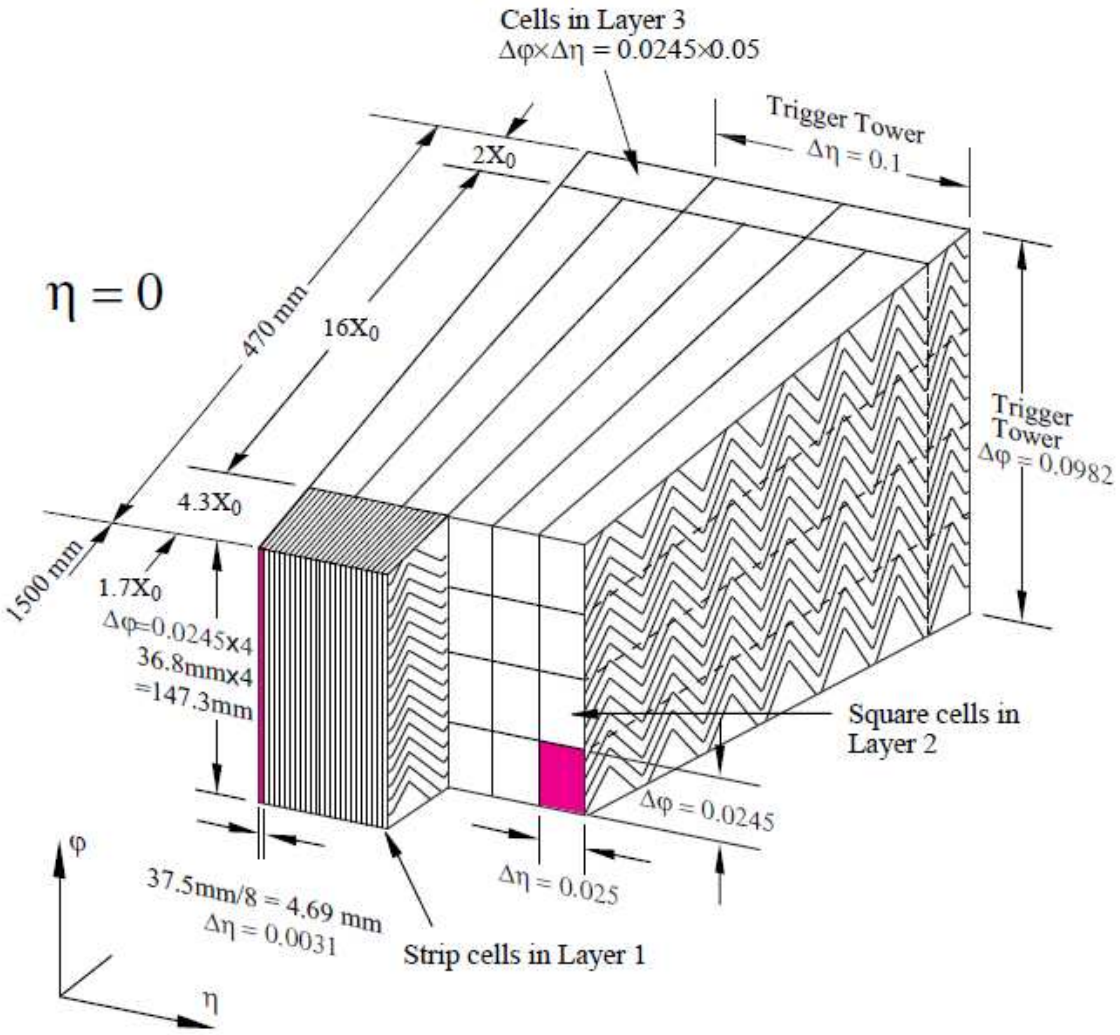

Figure 3.6: Sketch of a barrel module where the different layers are clearly visible with the ganging of electrodes in ϕ. The granularity in η and ϕ of the cells of each of the three layers and of the trigger towers is also shown.

bigger by factor of 10 than that of electromagnetic magnetic jets, the thickness of the hadronic calorimeter is large. The HC consists of three components such as the central barrel part or tile calorimeter(TileCal), the hadronic end-cap calorimeter (HEC), and forward calorimeter (FCAL). The tile calorimeter covers a η region of $|\eta| < 1.0$, and the two extended barrel covers the η region between 0.8 and 1.7. The hadronic end-cap calorimeter is responsible for the $|\eta|$ coverage from 1.5 to 3.2 and the FCAL covers the region of $3.1 < |\eta| < 4.9$. Thus, there is a small overlap between HEC and FCAL.

The TileCal uses scintillating tiles as the active material and has steel plates as the absorber. The active medium of HEC and FCAL are liquid argon, due to higher radiation tolerance, and the absorber material of HEC and first module of FCAL are copper plates while the rest of the FCAL modules use tungsten as an absorber.

3.2.1.4.3 Muon Spectrometer (MS)

The Muon Spectrometer [14], shown in Figure 3.7 [14], is outermost and the biggest sub-detector of the ATLAS detector. It covers the pseudorapidity range of $|\eta| < 2.7$, and the trigger coverage is $|\eta| <$2.4. This is designed to identify the high-p_{T} muons, a major signature of physics interest and it is instrumented with separate trigger and high-precision tracking chambers. The muon system measures the muons with the minimum energy of roughly 6 GeV which pass through the inner detector and the calorimeter with little interaction, while the low energy muons are absorbed before they reach the muon spectrometer. The muon spectrometer would be able to achieve a momentum resolution of 10% for muons with transverse momentum of 1 TeV.

In order to measure the momentum of the muons using magnetic bending a magnetic field is used. The large barrel toroid magnets are used to provide magnetic bending over the range of $|\eta|$ <1.4. In the region of $1.6 < |\eta| < 2.7$, to bend the muon tracks, two smaller end-cap toroid magnets are inserted into both ends of barrel toroid. For the transition region, $1.4 < |\eta| < 1.6$, a combination of barrel and end-cap field are used to get magnetic deflection. The magnetic toroids have air-filled cores, and provide a magnetic field which is in general orthogonal to the muon trajectories while it minimizes the degradation of resolution which is caused by multiple scattering.

In the barrel region, three chambers are arranged as cylindrical layers around the beam axis, and there are three planes in the end-cap region perpendicular to the beam axis. There are four different types of detection technologies that are used in the MS: The Monitored Drift Tubes (MDTs) and Cathode Strip Chambers (CSCs) are used for precision measurement and Resistive Plate Chambers (RPCs) and Thin Gap Chambers (TGCs) are used for trigger measurement. The drift tubes, are made of gas filled aluminum tubes with a radius of 15 mm and have an average resolution of 80 μm for a tube or 35 μm for a chamber, measure the precise muon trajectory in the magnetic field bending direction. The MDTs cover the η region of $|\eta| < 2.7$ except the innermost end-cap layer where they cover up to $|\eta| < 2.0$. The CSCs are used, in the large η region ($2 < |\eta| < 2.7$), in the innermost most end-cap tracking layer instead of MDTs due to their finer granularity and high rate of time resolution. The CSCs are multiwire proportional chambers with cathode planes segmented into orthogonal strips [14]. The CSCs have resolution of 40 μm in the bending plane (the tracks are

bent by the magnetic field) and around 5 mm in the transverse plane. In the case of the trigger system, the acceptance of trigger chambers is in the range of $|\eta|$ <2.4. Resistive Plate Chambers and Thin Gap Chambers are trigger elements for barrel and end-cap regions respectively. They provide a fast momentum measurement of muons for the hardware based trigger (L1) and they also provide the timing information of MDTs.

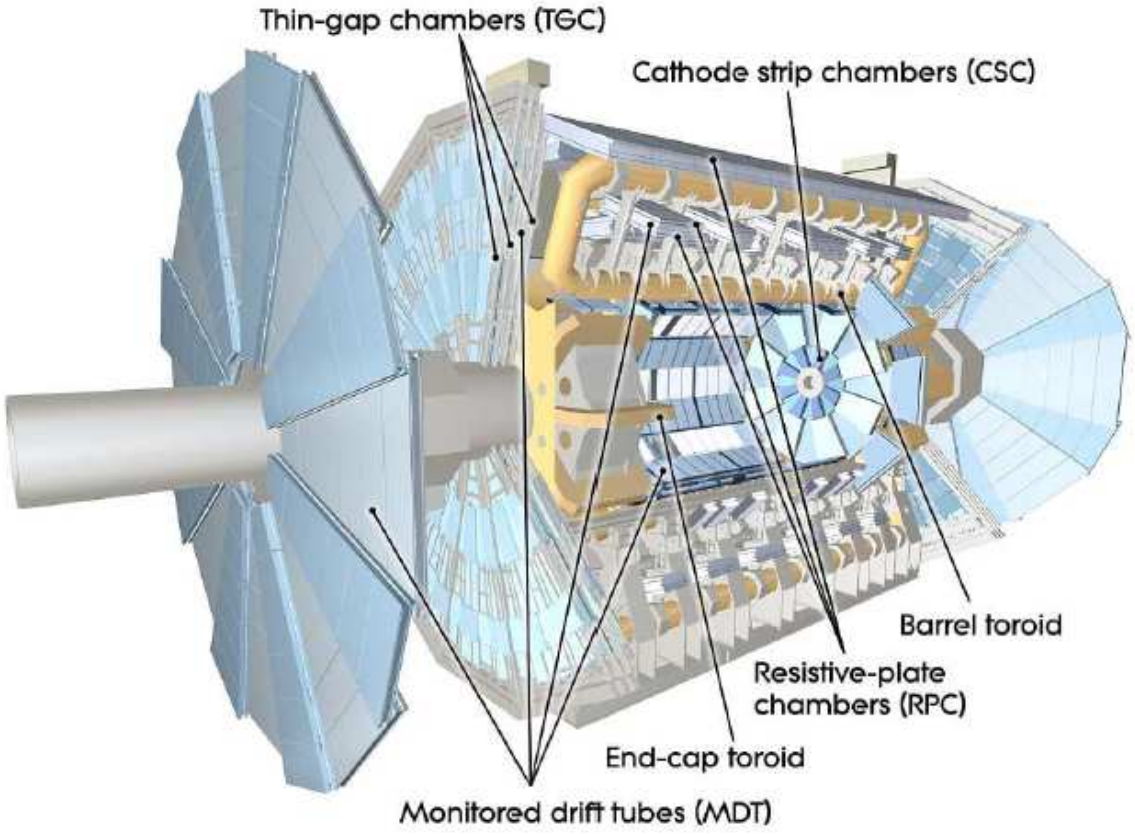

Figure 3.7: The ATLAS Muon system with toroid magnet.

3.2.1.4.4 Forward Detector (FD)

In addition to the ATLAS detector system, three small detectors, shown in Figure 3.8 [14] are positioned in the forward region. Two of the detectors measure the luminosity which is delivered to the ATLAS detector. The first detector of FD is known as LUCID (LUminosity measurement using Cerenkov Integrating Detector) and it is located at $z = \pm$ 17 m from the interaction point. LUCID detects the inelastic scattering in the forward region and it monitors the relative-luminosity for ATLAS. The second detector ALFA (Absolute Luminosity for ATLAS) is located at $z = \pm$ 240 m. It measures the absolute luminosity at small angles. The Zero Degree Calorimeter (ZDC), the third system, is located at $z = \pm$ 140 m, determines the centrality of the heavy-ion collisions.

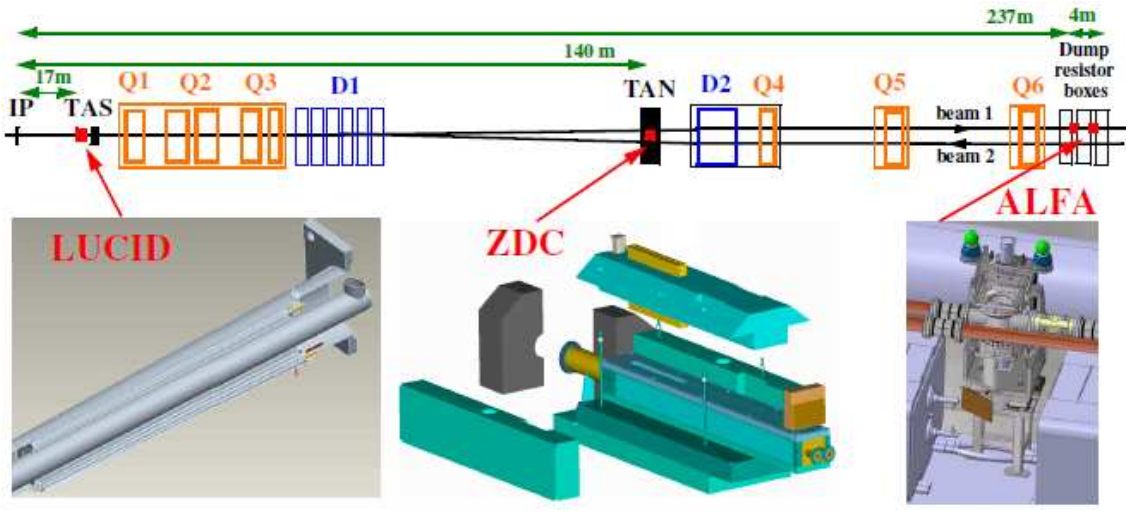

Figure 3.8: The forward detectors along the beam-line around the ATLAS interaction point.

3.2.1.4.5 Trigger System and Data Acquisition

The size of data in each collision is in the order of 1 MB with the bunch crossing rate of 40 MHz. This makes a volume of data that cannot be stored using current technologies. Therefore, the ATLAS trigger system is used to minimize the rate of candidate collisions from 40 MHz to 200 Hz without losing any interesting physics phenomena. The trigger system consists of three levels:

- Level-1 (L1)
- Level-2 (L2)
- Event Filter (EF)

The last two levels, L2 and EF, are collectively referred as the High-Level Trigger (HLT). The level 1 (L1) is based on hardware of the detector [20]. It uses a limited amount of the detector information. The Level 1 trigger collects information from the calorimeter with reduced granularity and from the muon trigger RPCs and TGCs. From the collected information, the L1 trigger system will decide whether the event should be selected or rejected within a very short period of time of 2 μs. The target rate of data will be reduced from 40 MHz to 75 kHz by the L1 trigger. Another major goal of the L1 trigger is to define the "region of interest" (RoI) [3] for each event. After the selection of an event, the L1 trigger passes the event information to the L2 trigger. The level 2 (L2) trigger is a software based trigger and it is seeded by the information from L1 trigger. It uses full granularity and precision of the detector in the RoI. The data target rate of L2 trigger is below 3.5 kHz with an average processing time

[3]The RoIs are the regions where the physics interesting object might be present.

of approximately 40 ms [14] for an event. After selection of an event using all L2 requirements, the L2 trigger passes the event to the third level trigger (Event Filter).

The EF is the last trigger which makes the final decision of accepting an event for further analysis. The Event Filter is designed to reduce the event rate to 200 Hz. The event filter is also a software based trigger and it runs on a dedicated computer farm near the ATLAS detector. The event processing time is relatively high, on the order of seconds. The EF has full access to the event with high granularity and more detailed algorithms are used for EF selection.

3.3 Pixel Detector

The ATLAS Pixel Detector is the innermost sub-detector of the inner detector (ID). This is one of the major components of the inner tracking system. The pixel detector consists of identical modules in both the barrel and the disks. There are approximately 80 million channels in the pixel detector and it provides excellent pattern recognition ability to reconstruct the tracks at the luminosity of the LHC of $L = 10^{34}\text{cm}^{-2}\text{s}^{-1}$. This detector is also one of the most important detectors is used to identify and reconstruct secondary vertices created by the decay of particles with a b-quark. This also has excellent spatial resolution capability for reconstructing the primary vertex from pp collisions.

The pixel detector is subdivided into three barrel layers and six disks (three disks on each side of the forward direction). In the barrel layers, 13 pixel modules are mechanically mounted together in a structure known as a stave. In the disks, 6 pixel

modules are mounted together on a support plate known as sector. There are 22 staves in the innermost layer (L0 or B-layer), 38 staves in the second layer (L1) and 52 staves in the final layer (L2). Each disk consists of eight sectors. A total of 112 staves and 48 sectors form the whole pixel system (a total of 1744 modules with 1.7 m^2 active area).

3.3.1 Pixel Silicon Sensors

The silicon sensors are the active part of the pixel modules and are used to detect charged particles. The Pixel sensors consist of bipolar diodes which are placed in an array on a high resistivity n-type bulk material. The pixel silicon sensor is implanted by high positive (p+) and negative (n+) dose regions on both sides of the sensor. An depletion region is produced at the p^+-n junction in reverse bias mode over the whole sensor bulk volume. In the pixel detector, the sensor has a 256 $\pm\mu$m thick n-bulk material which contains n^+ implants on the readout side and a p-n junction on the back side [21]. A pixel sensor consists of 47232 pixels which are arranged in 144 columns and 328 rows. The charge produced by ionized particles is collected on n^+ implants when the charge passes through the active volume, which allows longer life time for the sensor after radiation.

3.3.2 Pixel Modules

The basic components of a pixel module of the ATLAS pixel detector is shown in Figure 3.9 [14]. The Atlas Pixel module contains an oxygenated silicon sensor, 16 front end (FE) chips, and a flex hybrid which contains the control circuits [21]. The

pixel detector has 1744 pixel modules, is described in section 3.3, and each module has sensitive area of 60.8×16.4 mm^2. Each sensor of the pixel detector contains 47,232 pixels (with some exceptions) as described in Section 3.3.1.

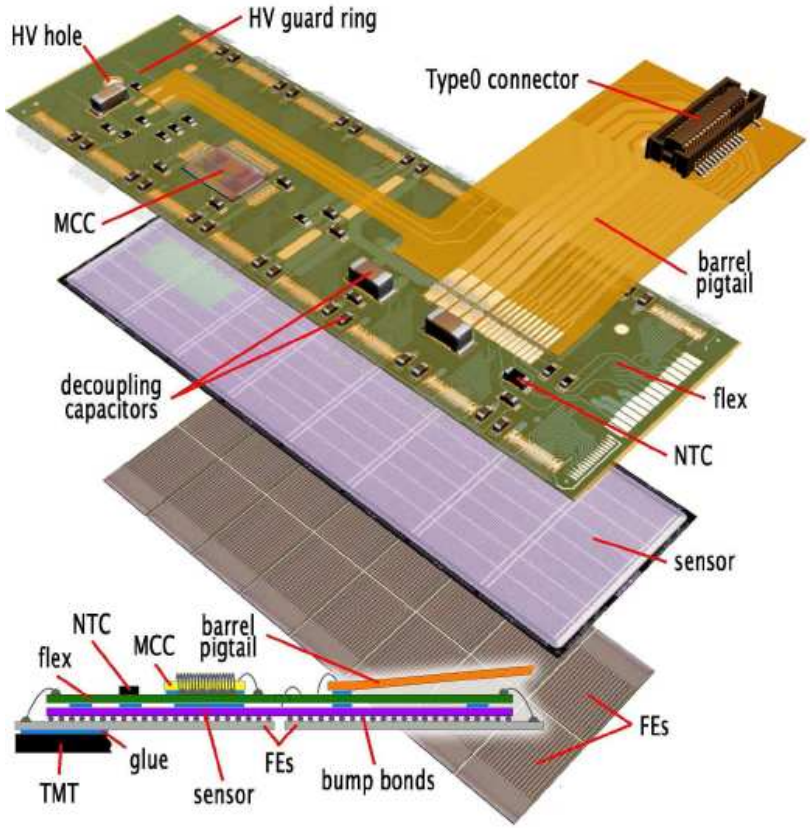

Figure 3.9: Schematic view of a barrel pixel module: The pixel hybrid control circuits (top), sensor elements, including the MCC (module-control chip), the front-end (FE) chips, the NTC thermistors, the high-voltage (HV) elements and the Type0 signal connector.

Each pixel module consists of sixteen front end (FE) chips. Each FE chip contains 2880 pixel cells 50×400 μm^2 size arranged in a 18×160 matrix with amplifying circuits. The single FE chip components are shown in Figure 3.10 [21]. These FE chips (electronics) are connected to the sensor through bump bonds, which is shown

in Figure 3.11 [21], to form a bare module. Each readout cell contains an analog and a digital block. In the analog block, the charge signal from the sensor is amplified and compared to a discriminating threshold which is programmable. The digital readout transfers the pixel hit address, a time stamp of leading edge (LE) and digitized trailing edge (TE) to buffers at chip periphery and stored for 3.2 μs. The Time over Threshold (ToT) is calculated by subtracting the time stamp of the trailing edge (TE) from the time stamp of the leading edge (LE). Around 89% of the pixels (128 columns of pixels) have the size of 50×400 μm^2 and are referred as normal pixels. The rest of the 11% of the pixel, from the 16 columns, have the size of 50×600 μm^2 and are known as *long* pixels. There is a gap of 400 μm between two neighboring FE chips. The long pixels of 600 μm length are used for a contiguous sensitive area between chip boundaries in the long pixel direction. In the short pixel direction, there are eight pixels, four pixels from each of the two adjacent columns of the chips, which cannot be connected directly to the FE chip through bump bonds. These pixels are ganged to one of the neighboring pixels through metal lines to connect to FE chips as illustrated in Figure 3.12. These pixels are known as *ganged* pixels. The pixels between two ganged pixels are referred as inter-ganged pixels. This type of connection strategy leads to 46080 channels.

The charge sensitive amplifier has a feedback circuit to discharge current at high output signal amplitudes. The return to baseline is, therefore, approximately linear and a discriminator pulse width is proportional to the input charge [22]. Therefore, the width of the discriminatory output, Time over Threshold (ToT), can be used to measure the amplitude of the output signal. The ToT duration is measured in the

units of 40 MHz MCC clock which is the same frequency as the LHC bunch crossing frequency (BC).

Each FE chip channel has a local 14-bit control register. Several parameters in each pixel can be tuned through this 14-bit control register. These bits are mainly used to control the Digital-to-Analog-Converter (DAC) parameters. This control logic provides 3 bit feedback current trim (FDAC) to tune the ToT response and 7-bit threshold trim (TDAC) to tune the threshold. In addition to the local control register, there are 231-bit global DACs in each FE chip, which tune the feedback current (IFDAC) scale and threshold (GDAC) for pixels on a single FE chip.
Each pixel module has a Module Controller Chip (MCC) which is glued to the flex hybrid [4]. Signal and power are routed by the flex hybrid. The MCC controls the digital readout of all sixteen FE chips.

3.3.3 Pixel Readout System

The pixel readout system architecture is shown in Figure 3.13. Figure 3.13 shows that the off-detector readout system consists of the Back of Crate (BOC) cards, the Read Out Drivers (RODs) and the Read Out Systems (ROSs). The communication between on-detector optoboards, which converts electrical MCC signals from pixel modules, and BOC occurs through optical fibers. The optoboards are located at the Patch Pannel 0 (PP0) region. The read out drivers of the pixel detector are located at 9UVME64 crates at the counting room. Each 9UVME64 crate contains up to 16 BOC and each BOC is paired with a ROD, a Trigger, Timing and Control Interface

[4]The flex hybrid is a double sided flexible printed circuit with 100 μm thickness.

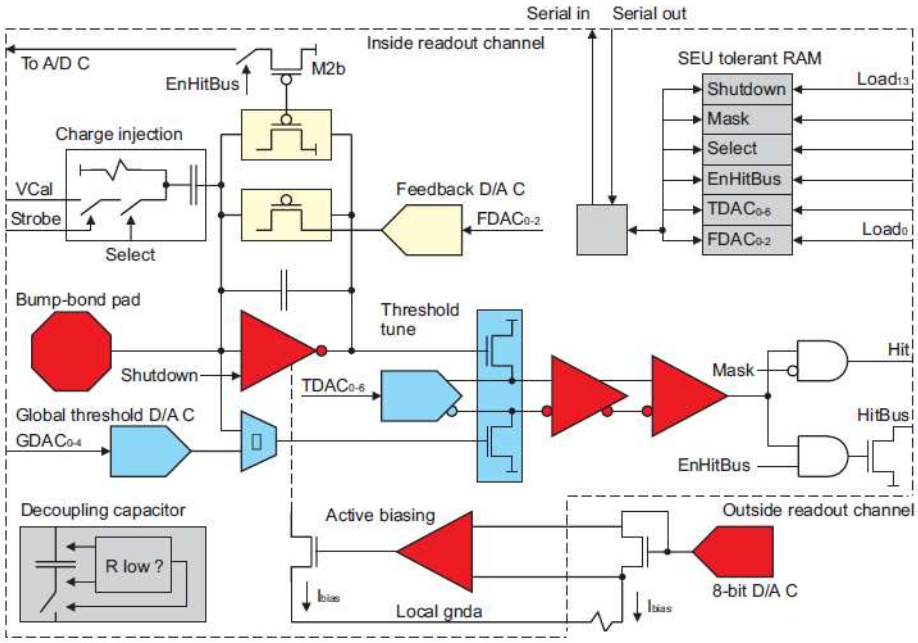

Figure 3.10: The components of single FE chip cell.

Module (TIM) and a single board computer (SBC), which controls all the components of the crate. The major function of the readout system is to transfer the data from the module to an offline system.

3.3.4 Pixel Detector Services

The services of the the ATLAS pixel detector is known as the Detector Control System (DCS). The DCS controls the powering and monitoring of the pixel detector. Figure 3.14 [22] shows an overview of the pixel detector control system (DCS). The pixel power supply system has five major components: Low Voltage (LV), Wiener, power supply, High Voltage (HV), ISEG, power supply, Regulator station, Supply and Control for the Opto Link (SC-OLink) and the optoboard-board heater power supplies. There are two low voltage supplies such as the analog voltage (V_{DDA}) and

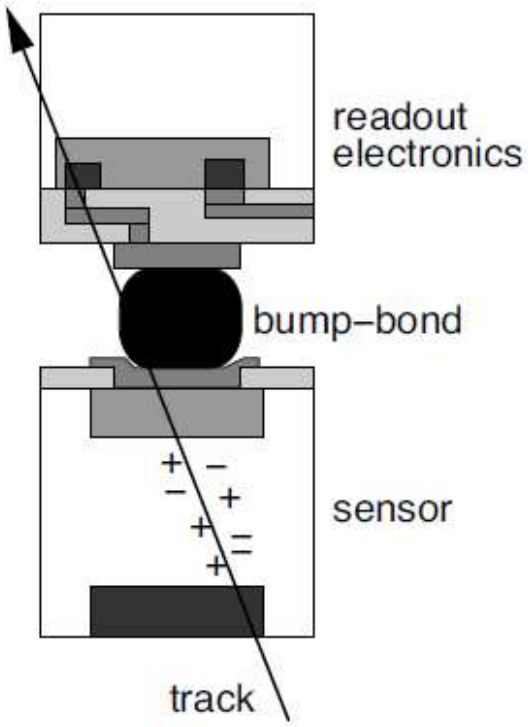

Figure 3.11: The cross section of a hybrid pixel detector, showing one connection between a sensor and an electronics pixel cell (not scaled).

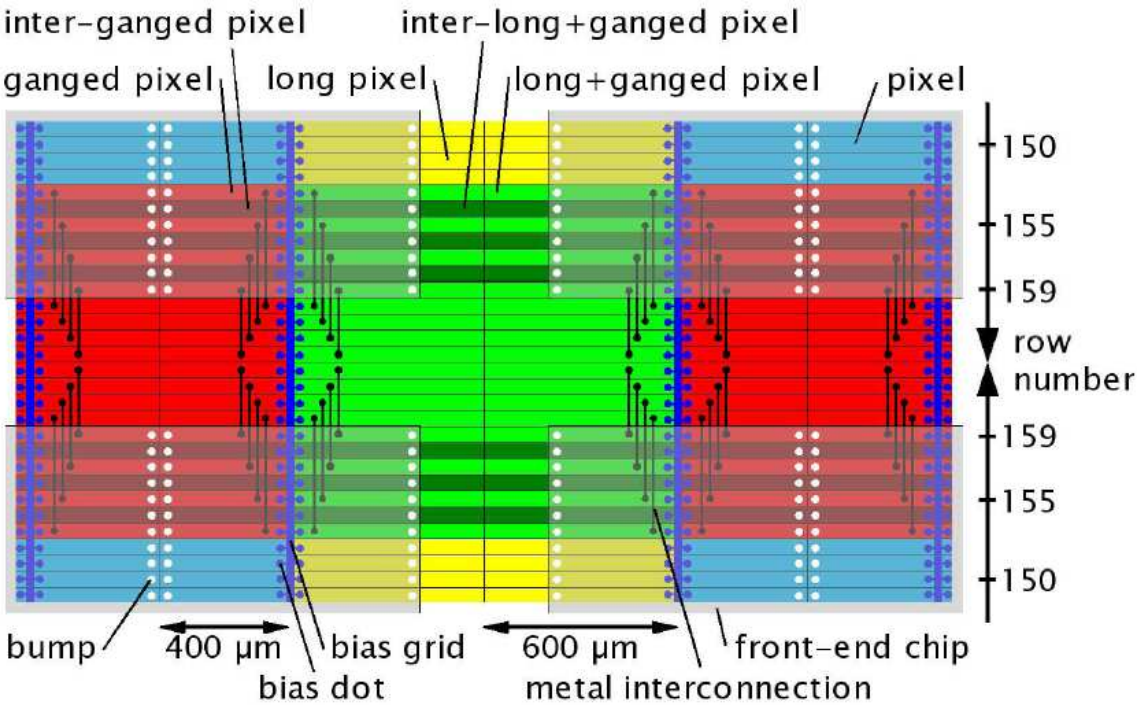

Figure 3.12: Layout of the different pixel types in the adjacent FE chip region.

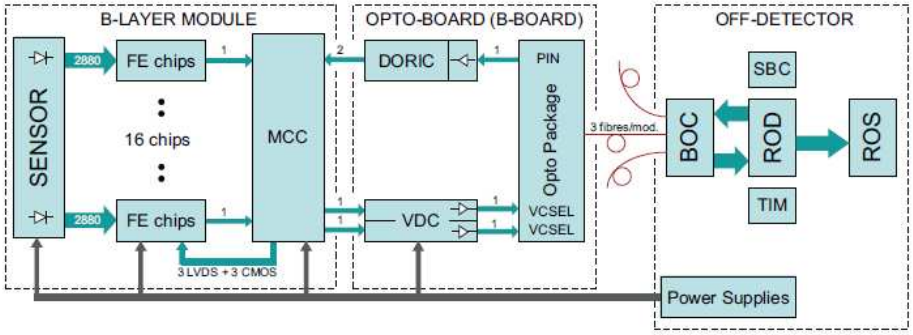

Figure 3.13: The readout system architecture of the ATLAS pixel detector.

digital voltage (V_{DD}) of the FE chip. The pixel low voltage (LV) Wiener power supply delivers the power to both the analog low voltage (V_{DDA}) and the digital low voltage (V_{DD}) supplies. The power from the low voltage Wiener supply is regulated by the low voltage Patch Panel 4 (LV PP4) and transmitted to the regulator station which is installed as close as possible to the detector (10 m) in order to minimize the voltage drop (and to protect the sensitivity of FE chips). The regulator stations provide the individual power output to both V_{DDA} and V_{DD}. The pixel sensors are biased by high voltage (V_{DET}) through high voltage (HV) ISEG power supply. The HV power supply is connected through a High Voltage Patch Panel 4 (HV PP4). In general, a pixel module obtains a low voltage of 2.1 V for V_{DD} and 1.7 V for V_{DDA} and the sensor bias voltage (V_{DET}) can varies between 150 V to 600 V.

The optoboards are powered by the SC-Olink. This delivers a low voltage power supply (V_{VDC}) for the VCSEL Driver Chip (VDC) and Digital Opto-Receiver Integrated Circuit (DORIC). The SC-Olink also provides a PIN diode bias voltage (V_{PIN}) for the optoboards. The typical values of V_{VDC} and V_{PIN} are 6 V and 10 V respectively. The next part of the services is to monitor temperature and humidity. This monitoring system is performed by Building Block Monitoring (BBM) and Building Block Interlock and Monitoring (BBIM). The BBM reads the values of the temperature and humidity and BBIM creates a logical signal and these messages are fed into the Interlock System.

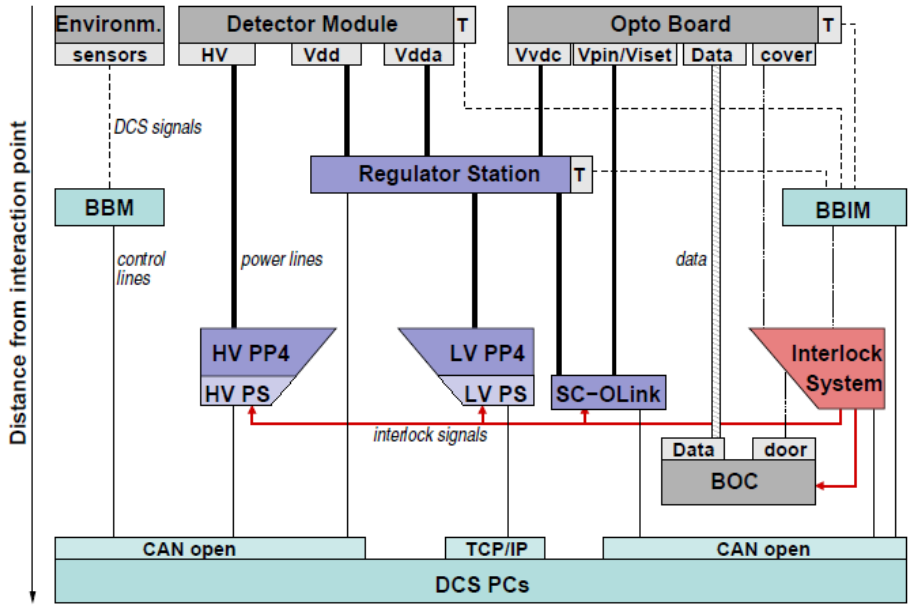

Figure 3.14: Overview of the Detector Control System of the Atlas pixel detector

3.3.5 Pixel Detector Calibration

The pixel detector is continuously exposed to a high radiation dose during its operation. This radiation effect can change the performance of the both sensor and electronics detector. It is very important to keep the initial performance through out its lifetime. Therefore, the pixel detector is tuned and calibrated regularly. The calibration procedure consists of optical readout tuning in order to establish error free optical communication, the signal threshold tuning for pixel uniformity and the ToT tuning to adjust the charge response for a minimum ionizing particle. The first calibration was performed at the end of 2008, which is considered as the reference for baseline performance.

3.3.5.1 Optical Tuning

A reliable and error free optical communication is required to ensure stable detector operation. In order to establish a good optical communication between modules and electronics the optical links need to be tuned [23]. The optical tuning procedure consists of three steps:

- Confirming that information can be transmitted to the modules (downlink).
- Confirming that information can be received from the modules (uplink).
- Tuning the parameters of received information from modules.

The transmission (downlink) is verified by sending a light pulse from the Tx plugin on the BOC through the fiber link and measuring the current of the optoboard PIN diode. The uplink verification is accomplished by setting the module to send a 20 MHz test clock pattern through uplink fibers to the BOC. The received signal is measured by the PIN diode in the Rx plugin on the BOC. The optical tuning includes signal threshold and delay of Rx plugin and varying the output power of the VCSELs on the optoboards. The signal threshold and delay are obtained by scanning through a set of values to find out the error free region with a 20 MHz clock pattern. Figure 3.15 [23] shows a typical scan result. The white area represents the error free region and the remaining region indicates non-zero error rates. The output power of the VCSELs is tuned to keep within the limits set by the off-detector threshold and to obtain a stable transmission signal. Certain channels, those in which the VCSEL on the detector are exhibiting a slow power turn on, require a second pass of tuning. In the

second round tuning, the modules are required to send back a known pseudo-random data pattern, which is received by the Rx plugin inside the BOC. The new correct values for threshold and delay are chosen in the error free region for these channels.

To verify the success of the optical tuning a digital pulse is injected into each readout channel beyond the discriminator and checking whether the BOC receives the signal. This verifies the optical tuning of the digital part of the FE chip. A similar procedure is carried out to test the analog functionality by injecting a charge into each readout channel after the discriminator. If the hit is registered by the BOC, this verifies analog functionality of the FE chip.

3.3.5.2 Threshold Tuning

In the pixel readout, each pixel has an adjustable threshold charge which is measured in electrons (e). A pixel can only read out if the signal is larger than the corresponding threshold. The threshold charge limits the noise. The threshold scan provides the corresponding threshold charge of each pixel. In a threshold scan, a fixed number of charges is injected into pixel preamplifier for each step of the threshold scan and the number of read out hits received by the BOC, are counted versus the injected charge. The resulting turn-on curve (S-curve) is fitted by a Gaussian Error function as illustrated in Figure 3.16 [24]. The corresponding threshold is defined as the charge at which the hit efficiency of the injected charge is 50%. The width of the fit, defined as the difference between the charge values that correspond to 16.5% and 83.5% hit efficiency, is regarded as the noise of the pixel.

The threshold charge of each pixel is tuned by injecting the charge correspond-

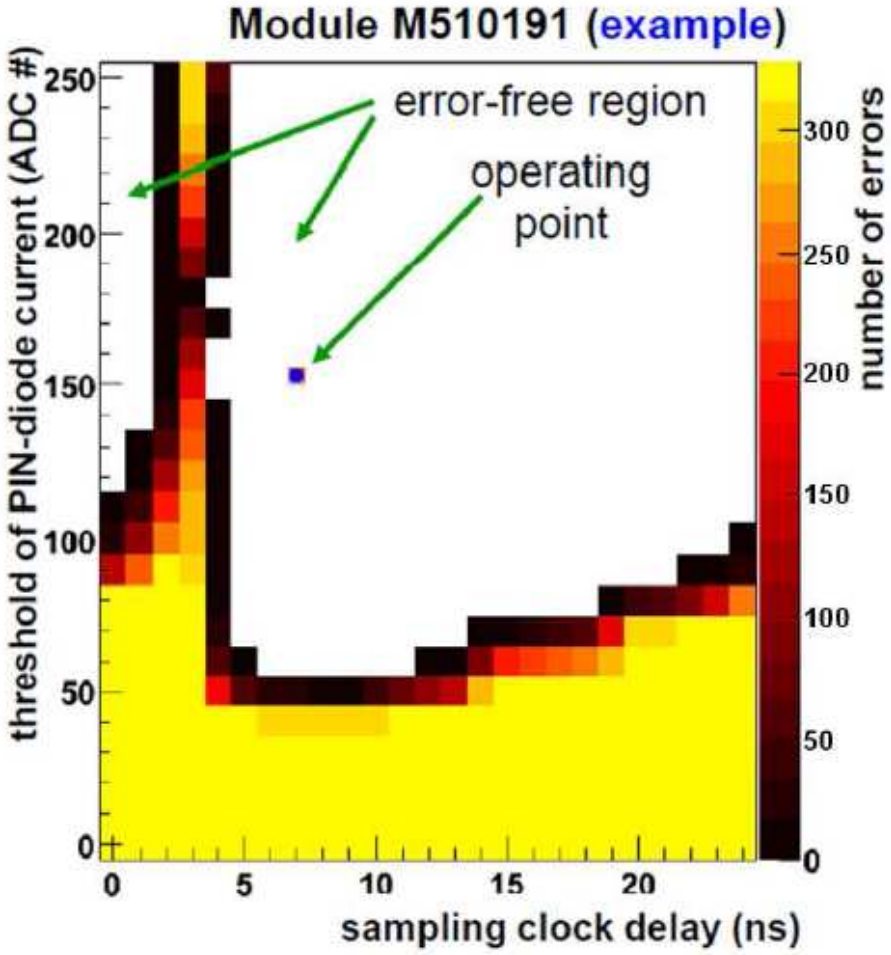

Figure 3.15: Scan of the optical link. The arrows indicate the error free region (white) and a possible set point for threshold and delay.

ing to the desired threshold and various FE chip parameters until the efficiency of reconstructed hits is 50%. Typical values for the threshold and noise are shown in Figure 3.17 which was done during the 2008 tuning period [24]. The initial tuning threshold charge was 4000 electrons.

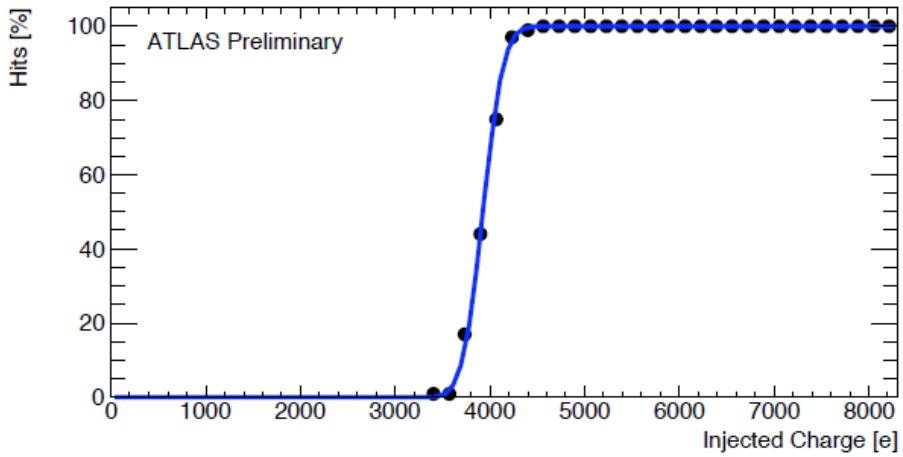

Figure 3.16: A typical turn-on curve or S-curve that results from a threshold scan of one pixel. This curve is fitted by a Gaussian error function.

3.3.5.3 Time over Threshold (ToT) Tuning and Calibration

The difference in the time between the trailing and leading edge is known as Time over Threshold (ToT) as described in Section 3.3.2, which is measured in units of bunch crossings (BC), equivalent to 25 ns at the 40 MHz LHC clock. The TOT pulse width is linearly proportional to the signal charge through a programmable constant-current in the feedback loop of the pixel preamplifier. The ToT parameters are currently tuned for each pixel to ensure that the ToT value of 30 BC corresponds to 20,000 electrons and the dispersion of the ToT is around 0.7 BC. Figure 3.18 [25]

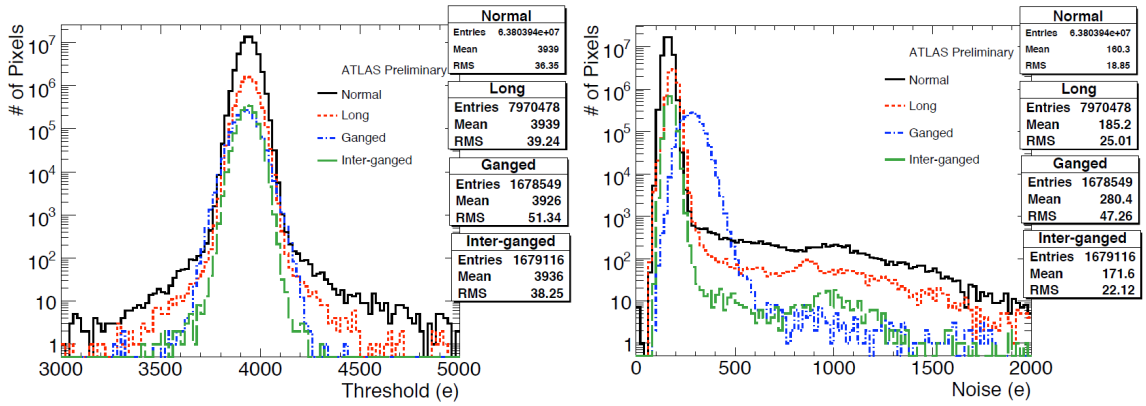

(a) (b)

Figure 3.17: Threshold (a) and noise (b) distributions for normal, long, ganged, and inter-ganged pixels on 1642 modules with the 2008 tuning

shows the ToT distribution which was produced during module production tuning and after the 2008 tuning.

3.4 Summary

This chapter discusses all the components of the ATLAS detector briefly and their functions. A detailed explanation of ATLAS pixel detector, its function, its operation, and its calibrations are also discussed.

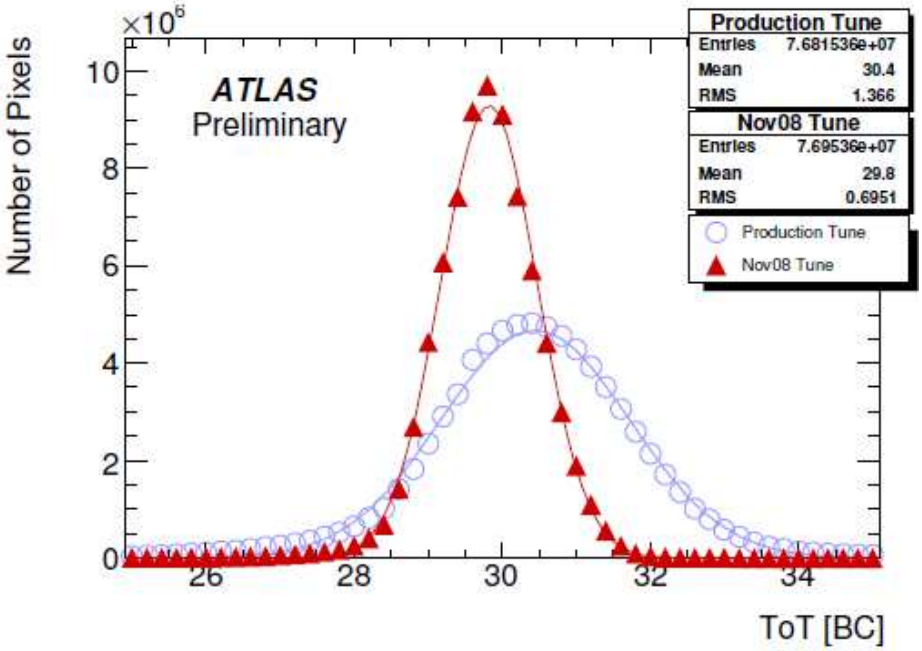

Figure 3.18: The time-over-threshold (ToT) distribution for pixels are produced with an injected charge of 20,000 electrons with the tuning performed during module production (open) and after the 2008 tuning (closed)

Chapter 4

Detection efficiency of the Atlas pixel detector using sensor overlap region with Cosmic Rays

4.1 Introduction

The Pixel Detector is the innermost detector in ATLAS, one of the sub-detectors that is most crucial for vertex reconstruction. The pattern recognition for track-finding is also seeded using the pixel detector (see Chapter 5). The efficiency of track-finding mainly depends on the single hit efficiency of the pixel detector when particles pass through the pixel sensors. The sensors are connected to amplifiers that have the ability to measure the charge deposited by the particle in the silicon sensor. It is therefore extremely important to calculate the single hit efficiency of the pixel detector accurately. The pixel barrel has regions in which a track will pass through

two neighboring modules on the same layer along the ϕ direction . This region is known as overlap region. In this Chapter, the single hit efficiency is measured only in the overlap region.

In this overlap region there is one extra cluster on the same layer for a track. So It is very important to use this region to calculate the single hit efficiencies for the second hit on the neighboring modules. We are able to use cosmic rays to calculate detection efficiencies to calibrate the detector. We are able to measure the single hit efficiency of the second hit on the same layer in the overlap region very accurately and precisely using cosmic-rays. The global χ^2 aligned geometry has been used for our analysis.

The results from this Chapter can be compared with the detection efficiency of the full pixel detector and also can be compared with the results obtained once p-p collisions occurs in a high multiplicity environment.

4.2 Data Sample

We have used both magnetic (solenoid) field ON and magnetic (solenoid) field OFF runs. The data were recorded in two periods. The first period was during September-October and the second period was during November. The first period runs include both magnetic field ON and OFF data sets while the second period has only magnetic field OFF runs. We have selected the magnetic field ON data from first period and the magnetic OFF data from second period.

The runs that we have used for our analysis are as follows:

First run period, magnetic field ON: 91885, 91888, 91890, 91891 and 91900.

Second run period,magnetic field OFF: 96538, 96542,96544, 96582, 96644, 96659, 96696, 96672, 96732, 96858, 96884, 96895, 96903, 96906, 96913 and 96982.

The total tracks that we used for the magnetic field ON and OFF are 56838 and 83666 respectively.

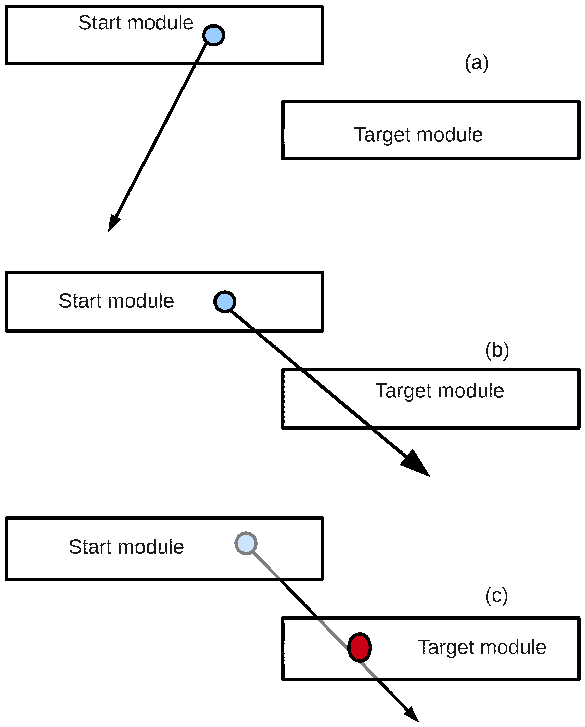

Figure 4.1: The track extrapolation from start module to target module.

4.3 Procedure

When the muons coming from cosmic rays pass through the pixel detector the pixel sensors can detect a charge pulse. Charge pulses that are collected by one or more adjacent pixels form a cluster. The tracks associated with these clusters are reconstructed using the measurements from the Transition Radiation Tracker (TRT), the Semiconductor Central Tracker (SCT) and pixel detectors in order to select high quality tracks. The expected number of clusters is calculated by a straight line extrapolation of the track associated with the start cluster to the plane of the target module. A fiducial cut was applied to the intersection point of track and target module to predict expected clusters.

The efficiency of the target module (second hit on the same layer) can be defined as:

$$\epsilon = \frac{\mathrm{N_{clusters}}}{\mathrm{N_{expected\ clusters}}} \tag{4.1}$$

where $\mathrm{N_{Clusters}}$ is the number of reconstructed target clusters and $\mathrm{N_{expectedclusters}}$ is number of expected clusters. The main purpose of this study was to calculate the single hit efficiency of good modules so we did not consider the endcap region where the extrapolation is more complex.

4.3.1 Track Extrapolation

The track extrapolation is needed to calculate the expected number of clusters. The track starts from a module (start module) and can be extrapolated to the target module plane as shown in Figure 4.1. We expect three possible cases on the plane of the target module.

1. Case 1: The extrapolated track from the start module never reaches the target. In this case, neither numerator nor denominator of Equation 4.1 are incremented (see Figure 4.1(a)).

2. Case 2: The extrapolated track from the start module reaches the target module but there is no real cluster on the target module. In this case, the denominator of Equation 4.1 is incremented but the numerator of Equation (1) is not incremented (see Figure 4.1(b))

3. Case 3: The extrapolated track from the start module reaches the target module and It does have a cluster. In this case, both the numerator and the denominator of Equation 4.1 are incremented (see Figure 4.1(c)).

Since the distance between start module and the target module are extremely small, the straight line extrapolation method has been used to calculate the inter-subsection points of the track and the module. In the overlap region we would expect a second cluster in the same layer on an adjacent stave while the module number remains the same. If the local intersection point of the track and the module is inside the active fiducial region of the pixel modules we will expect a second cluster.

4.4 Track and Cluster Selections

4.4.1 Primary track selection

Selection cuts were made on the tracks to reduce biases due to, for example, cases where the tracks are extrapolated through an active sensor even though the real muons may not have passed through it. Such muons either missed the entire detector or passed through dead or inactive pixels.

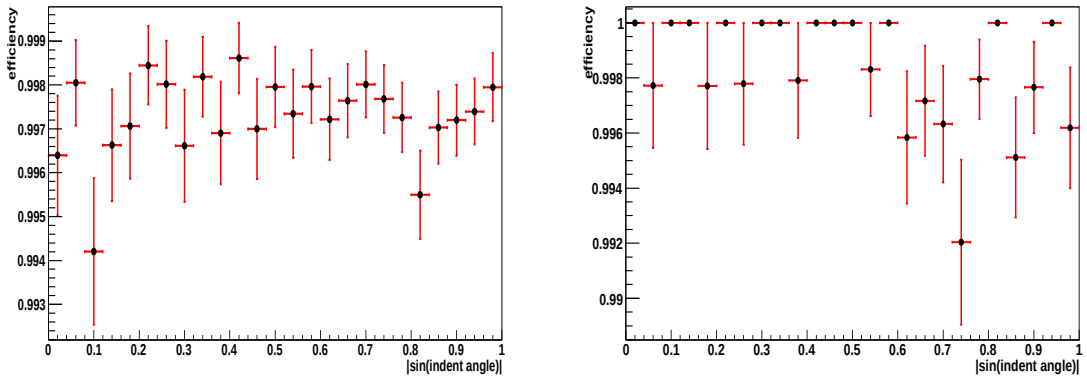

(a) (b)

Figure 4.2: The efficiency versus sin(incidence angle) where the incidence angle is the angle between the track and the normal to the module (in r-ϕ plane), with solenoid OFF (a) and the solenoid ON (b) in the local co-ordinate system.

The quality of the tracks is selected to reduce the biases discussed above. The selection criteria of the tracks are as follows: We required tracks with at least 30 TRT hits and 8 SCT hits. Since the overlap region is entirely in the barrel, the endcaps

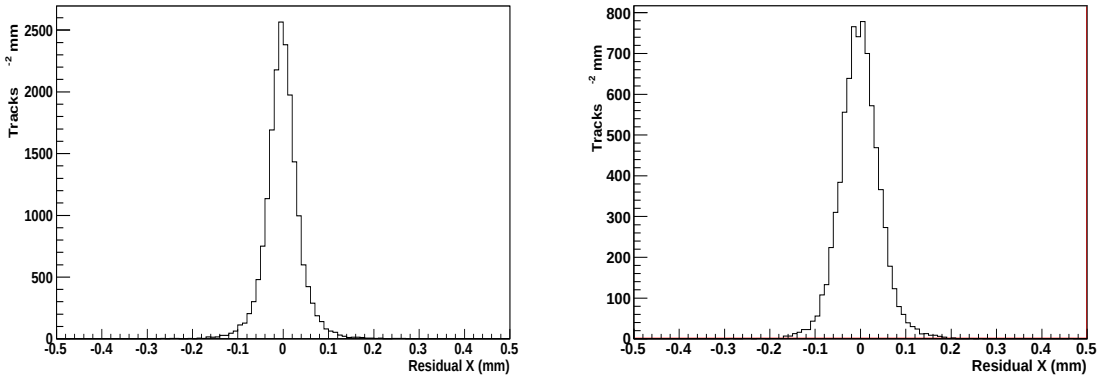

(a) (b)

Figure 4.3: The Residual distribution in X: The distance between expected cluster position and real cluster position with solenoid OFF (a) and the solenoid ON (b) in the local co-ordinate system.

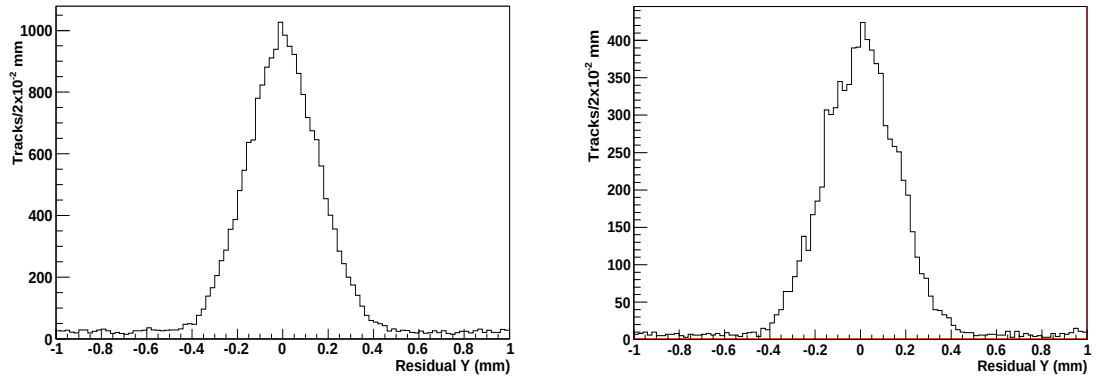

(a) (b)

Figure 4.4: The Residual distribution in Y: The distance between expected cluster position and real cluster position with solenoid OFF (a) and the solenoid ON (b) in the local co-ordinate system.

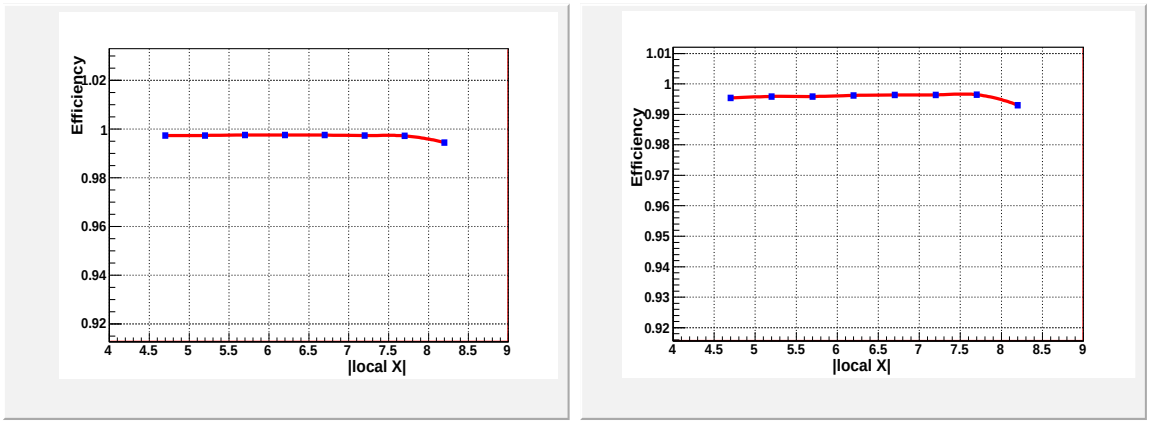

(a) (b)

Figure 4.5: Efficiency versus distance from the center of the module to cluster position in X direction with solenoid OFF (a) and solenoid ON (b) .

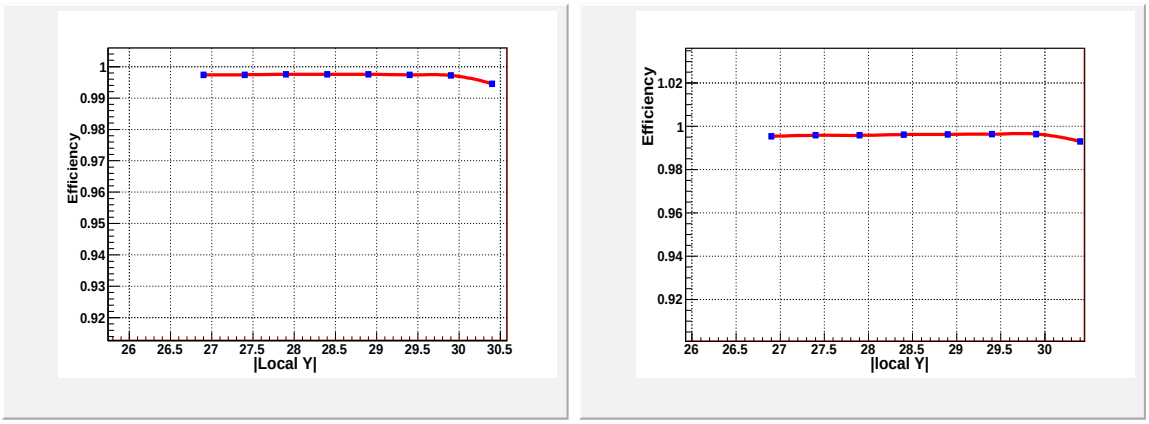

(a) (b)

Figure 4.6: Efficiency versus distance from the center of the module to cluster position in Y direction with solenoid OFF (a) and solenoid ON (b).

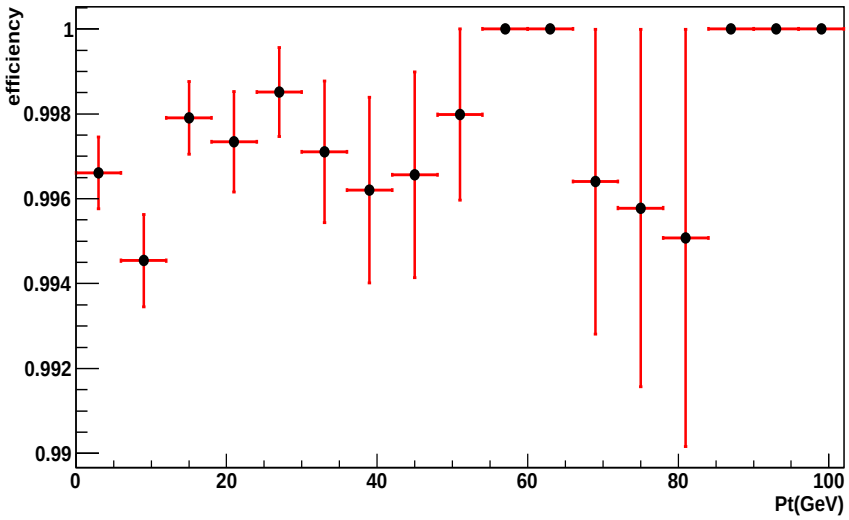

Figure 4.7: Efficiency versus transverse momentum of the tracks with solenoid ON.

were not included in this selection. We also required the sin$\alpha < 0.7$, where α is the incidence angle between the track and the normal to the module (in r-ϕ plane) as shown in Figure 4.2. In real p-p collisions the typical incidence angle is smaller than the 45°. So we require the incidence angle to be similar to that expected from p-p collisions since the tracking algorithm does not perform well at high incidence angles. The expected numbers of clusters from the intersection point is selected inside the fiducial region. The fake rate of the hits on the target modules can be excluded using selection cuts on residual distances. But the fake rate and the inefficiency of the measurements are 0.002717 and 0.002622, respectively. So the probability of having a noise module due to this fake hit is fake rate*(1-efficiency) is 0.000007 (7/1000000). We could expect one noisy module for each 140000 tracks. This value is extremely small so that we can neglect this effect by not making any cut on residual distances. To check the behavior of these fake hits we used a cut on residual distances, as illustrated

in Figures 4.4.1 and 4.4.1 with $|residual\ X| < 0.300$ mm and $|residual\ Y| < 0.900$ mm. Another major selection cut that we have used requires clusters within the fiducial region (the distance between the center of the module and the intersection point between extrapolated track and target module). Fiducial cut in the XY plane have been chosen where $|Local\ X| < 7.5$ mm and $|Local\ Y| < 29.5$ mm (see Figures 4.5 and 4.6). For the magnetic field ON tracks we have put a cut on the transverse momentum with p_{T} 10 GeV (see 4.7).

4.4.2 Exclusion of Dead Modules and Dead FE Chips

During cosmic ray data taking, some of the modules (dead modules) had problems with High Voltage and for other reasons could not be read out, and some of the front end chips (FE) were corrupted. Since our analysis intended to measure the detection efficiency of good modules, we decided to exclude all these dead modules and dead FE chips. The number of dead modules depended on the run numbers (most of the dead modules are common for all runs but there were some differences between). Therefore all dead modules were exclude in each run. Our present focus is the single hit efficiency of working channels *not* the single hit efficiency averaged over the full detector. The two quantities differ because of dead modules and dead front end chips. To isolate the quantity of interest, we do not increment $N_{expectedclusters}$ when the track extrapolates to a dead region.

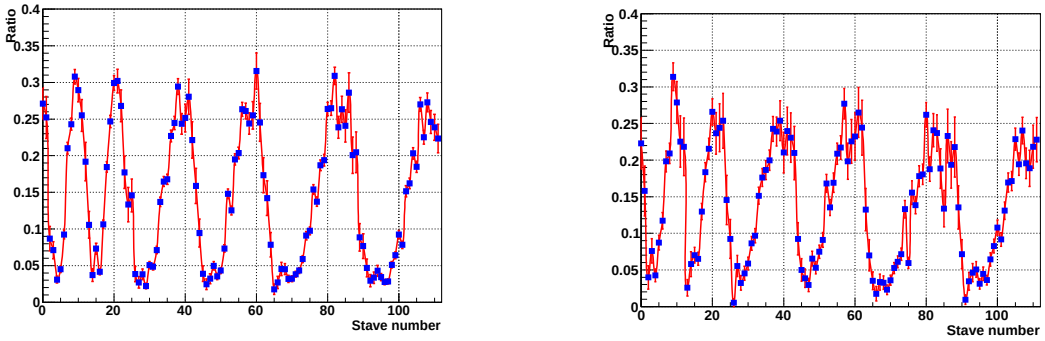

(a) (b)

Figure 4.8: The ratio of the number of tracks having two clusters on the same layer to the number of all tracks versus stave number with solenoid OFF (a) and solenoid ON (b).

Table 4.1: The comparison of single hit efficiencies with incident angle and without incident angle

Efficiency Selection	Solenoid ON(%)	Solenoid OFF (%)
Without incident angle selection	99.681 ± 0.0439	99.726 ± 0.0251
With incident angle selection	99.746 ± 0.0439	99.738 ± 0.0251
Statistical Error	0.0654	0.0110

4.4.3 Determination of Efficiencies

The detection efficiency was calculated using the number of good tracks that have two associated clusters in the same layer. The ratio of the number of tracks having two clusters on the same layer to the number of all tracks versus stave number is shown in Figure 4.8. The ratio changes with stave number. There are a total of 112 staves in the pixel detector. Even though the average ratio is about 13% for both solenoid ON and OFF samples there is a huge variation along the ϕ direction. There is higher ratio of around 25% in the region of top and bottom of the barrel while we have very low ratio at both sides of the barrel. This behavior is clearly due to the variation of incident angles. The top and bottom of the barrel region have very small incident angle while there is a bigger incident angle in the side region. We can have higher probability of having second hit when the incident angle is small because the distance between start and the target module is extremely small. When we determine the efficiency we have checked the efficiency without the incident angle cut and with incident angle cut as listed in the Table 1. Since we are dealing with a small extrapolation distance (< 1 mm), we might expect the efficiency of both solenoid ON and solenoid OFF to be very similar. One can clearly see from the Table 4.1 that the efficiencies for solenoid ON and solenoid OFF data are equal within errors.

4.4.4 Systematic Uncertainties

There is one dominant systematic error due to the incident angle. The final result of the efficiencies has been calculated by selecting the tracks in the region where the

incident angle is less than 45 degrees. Since the region is between two close modules, we would not expect a large systematic error due to material since there should be no material in this gap. The systematic errors of this analysis included only this incident angle effect with the errors of 0.0654 and 0.0110 for solenoid ON and solenoid OFF respectively.

4.4.5 Summary and Conclusion

The efficiency of the pixel detector in the overlap region has been calculated very accurately with a straight line extrapolation method. The final detection efficiencies of the pixel detector in overlap region for magnetic field ON and magnetic filed OFF are:

(99.746 ± 0.0438(sta) ±0.0654(sys))% and (99.738 ± 0.0251 (stat) ± 0.0110(sys))% respectively. This result is consistent with the results obtained by calculating detection efficiencies of the pixel detector using the whole detector [3].

Chapter 5

Minimum Bias

5.1 Minimum Bias Events

The definition of minimum bias events arises from the trigger which is used to accept the inelastic events. This trigger uses Minimum Bias Trigger Scintillators (MBTS) located on the detector end caps. Minimum bias events generally refer to events selected by a loose trigger using the MBTS that is able to accept a large fraction of the inelastic cross section. However, this definition can be slightly different in different types of experiments.

Most of the previous experiments' minimum bias studies were non-single-diffractive (NSD) measurements where the minimum bias trigger requires MBTS hits on both sides of the detector. The above trigger requirement will remove most of the single-diffractive events. But the current studies at the ATLAS experiment uses a single arm trigger to keep more diffractive events.

In practice, the minimum bias events are usually associated with the non-diffractive

(ND) portion of the total cross section, σ_{ND}, from Equation 2.5.

5.1.1 Minimum Bias Observables

Minimum bias events come from soft interactions with many low momentum charged particles. Therefore, the properties of the charged particle multiplicity of these soft interactions are studied. The typical minimum bias measurements are: number of charged particles per event, n_{ch}, charged particle pseudorapidity density, $\frac{dN_{\mathrm{ch}}}{d\eta}$, and transverse momentum spectrum, $\frac{dN_{\mathrm{ch}}}{dp_{\mathrm{T}}}$. The charged particle multiplicity distributions are the very first measurements of any experiment since the production cross section of charged particles is very high even for small luminosities.

The pseudorapidity density distribution, $\frac{dN_{\mathrm{ch}}}{d\eta}$, is strongly correlated with the rate of parton-parton scattering. This is due to the fraction of the collision energy that is converted into soft, low-p_{T}, particles which are produced in the central pseudorapidity region. The rate of multiple parton interactions increases with collision energies, with a large fraction of the particles produced in the central region. Therefore, the multiplicity pseudorapidity density will be more centralized at higher collision energies.

Figure 5.1 [26] shows the charged particle multiplicity produced by two different MC models (explained in Section 5.1.3) for 900 GeV collisions.

5.1.2 Primary and Secondary Particles

Particles that originate at the primary vertex where the proton-proton collisions occur are called primary particles. Examples of primary particles include pions, charged

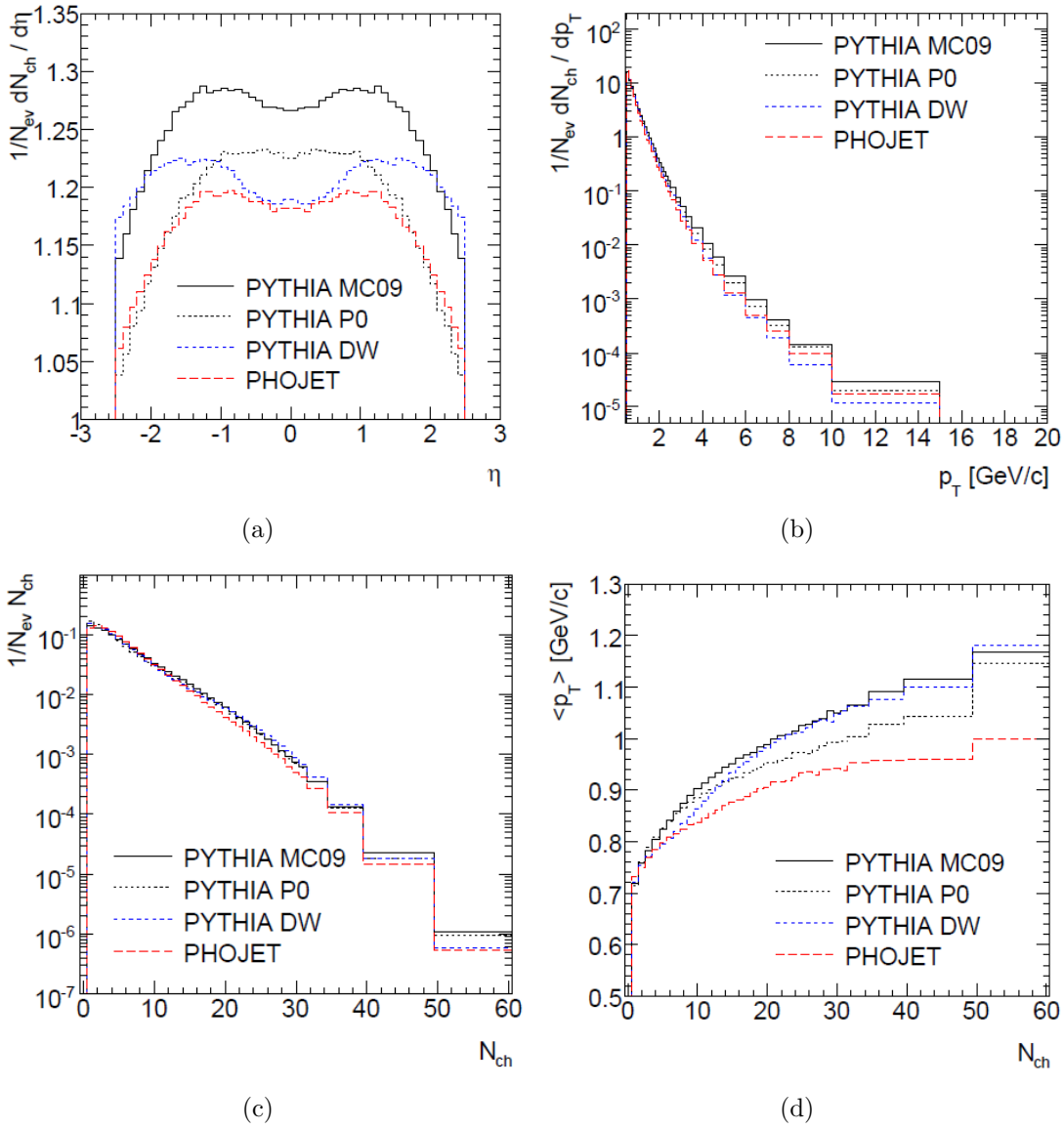

Figure 5.1: Predictions of the PYTHIA 6.421 generator using the ATLAS MC09 tune (full line), the Perugia0 tune (dotted line), the DW tune (short-dashed line) and of the PHOJET 1.12 generator (dashed line). Spectra contain both non-diffractive and diffractive components.

kaons and the decay products of bottom and charmed hadrons (a primary particle has a life time of more than $3 \times 10^{-9} s$). Secondary particles are those originating from different sources such as hadronic decays, decays of pions and kaons in flight, photon conversions, and particle decays in the detector volume. The particles other than primary particles are known as non-primary particles which includes both secondaries and fakes.

5.1.3 Monte Carlo Simulation for Minimum Bias Events

Minimum bias events are mainly dominated by soft, low p_{T}, scattering processes. Even though the soft interactions are not well described by QCD, they are still described by the Monte Carlo event generators by applying some appropriate tuning on their free parameters. These free parameters in the Monte Carlo generators control the properties of the generators.

Two major event generators, PYTHIA and PHOJET, are currently used to describe the minimum bias events.

5.1.3.1 PYTHIA Model

The PYTHIA [27] MC event generator was developed by the Lund group and is one of the major MC event generators that is frequently used in high energy physics experiments. PYTHIA has been mainly developed for high p_{T} physics using perturbative Quantum Chromodynamics (pQCD) $2 \rightarrow 2$ parton-parton scatterings. PYTHIA contains a large variety of different scenarios and steerable parameters which have an impact on the properties of generated minimum bias events. For the soft interac-

tions, the PYTHIA generator attempts to extend the high p_{T} pQCD process of parton interactions down to the low p_{T} region. In this transition process, a tunable cut-off parameter of p_T^{min} is introduced to regulate the divergence of the 2→ 2 parton-parton perturbative interaction cross section at $p_{\mathrm{T}} \to 0$. The p_T^{min} effectively controls the number of parton-parton interactions. The interaction cross section at the center-of-mass energy of $\sqrt{s}$ is given by:

$$\sigma_{int}(p_T^{min}) = \int_{p_T^{min}}^{\frac{s}{4}} \frac{d\sigma}{dp_T^2} dp_T^2 \tag{5.1}$$

where the $\frac{d\sigma}{dp_T^2}$ is the differential cross section of a 2→ 2 parton-parton scattering. In addition to p_T^{min}, some other effects such as interactions with beam remnants or color reconnection are also applied to generate events. PYTHIA has a large number of tunable free parameters which have significant impact on the generated distributions with different PYTHIA versions.

Two different strategies have been used to describe the parton showers in PYTHIA: Q^2-ordered parton shower (PYTHIA6) and p_{T}-ordered parton shower (PYTHIA6.4 - 8). Most of the recent tunes of PYTHIA use p_{T}-ordered showering which allows hard interactions to occur first.

5.1.3.2 PHOJET Model

The PHOJET [28] Monte Carlo even generator is used to model minimum bias events with both diffractive and the non-diffractive processes. PHOJET is described as a two compound model to describe the soft and hard scatterings. The Dual Parton Model

(DPM) [29–32] approach is used to describe the soft process while the perturbative QCD approach is used to describe the hard scatterings. Inelastic events are understood using cut pomerons [1], and each cut pomeron corresponds to the exchange of a soft gluon, which results in two strings being drawn between the two beam remnants. The uncut pomerons give virtual corrections to preserve unitarity. Since the pomerons can have both hard and soft behavior in PHOJET, the PHOJET generator provides an ideal smooth transition between soft and hard processes.

5.1.3.3 The Cross Section for Inelastic Scattering

Table 5.1 lists the cross sections that are predicted by PYTHIA 6.4 and PHOJET for all three inelastic processes at three different center-of-mass energies at the LHC. PHOJET predicts a total cross section that is 5 - 10% higher than that of by PYTHIA. The cross section of the non-diffractive part is the largest in all three center-of-mass energies. The single and double-diffractive components take second and third places respectively. Since PYTHIA does not simulate the central-diffractive component, there is no central-diffractive component prediction by PYTHIA. However, PHOJET predicts the cross section for the central-diffractive component. This cross section is one third of the double-diffractive component.

5.1.4 Tuning Monte Carlo Generators

The PYTHIA and PHOJET generators use several phenomenological models to describe the inelastic interactions, or soft hadronic interactions which contain several free

[1] cutting the transverse momentum of pomeron. A cut Pomeron may be either hard, when there are large pt partons in the final state, or soft, when no large pt parton is present in the final state

Process Type	0.9 TeV [mb]	2.36 TeV [mb]	7 TeV [mb]
PYTHIA			
Non-diffractive	34.4	40.2	48.5
Single-diffractive	11.7	12.7	13.7
Double-diffractive	6.4	7.7	9.3
Total	52.5	60.6	71.5
PHOJET			
Non-diffractive	39.9	50.3	61.5
Single-diffractive	10.5	10.6	10.7
Double-diffractive	3.5	3.9	3.9
Central-diffractive	1.1	1.2	1.3
Total	55.0	66.0	77.4

Table 5.1: Cross sections for the inelastic components of the minimum bias sample at $\sqrt{s}$ = 900 GeV, 2.36 TeV and 7 TeV as predicted by PYTHIA6 and PHOJET.

parameters. These free parameters can be tuned to give agreement with different measurements of inelastic collisions such as at CERN, the ISR and S$\bar{\text{p}}$S, as well as the Tevatron. At the LHC, in particular, due to large uncertainties extrapolating parameters from one center-of-mass energy to another a wide range of tuning has been performed. This dissertation explains the recent tunes of the PYTHIA generator in the next sections.

5.1.4.1 Overview Monte Carlo Tuning at ATLAS

The PYTHIA [27] MC event generator parameters previously have been tuned to describe charged-hadrons and the underlying event in pp and p$\bar{\text{p}}$ data at center-of-mass energies between 200 GeV and 1.96 TeV for LEP, HERA and the Tevatron. This tuning will improve the description of the various aspects of particle production such as cross sections, particle spectra, and fragmentation in various types of experiments.

For the MC sample production starting in 2009, a specific set of optimized parameters, the ATLAS MC09 tune, was introduced with inclusion of the MRST LO* parton density functions [27] which provide a better description of processes using leading-order MC generators like PYTHIA and p_{T}-ordered parton showering. There were three types of MC samples that were produced by this tuning such as single-diffractive, double-diffractive and non-diffractive samples [2] for our analysis. The parameters of ATLAS MC09 tune were derived by tuning to the underlying event and minimum-bias data from the Tevatron at 630 GeVand 1.8 TeV. The MC samples generated with this tuning were used to determine detector acceptances and efficiencies and to determine corrections to the data. MC samples were produced at all three center-of-mass energies considered in this paper. The non-diffractive, single-diffractive, and double-diffractive contributions in the generated samples were mixed according to the theoretical cross sections to fully describe the inelastic scattering.

All the events were processed through the ATLAS detector simulation program [33], which is based on Geant4 [34]. They were then reconstructed and analyzed by the same program chain used for the data. Particular attention was paid to the description in the simulation of the size and position of the collision beam spot and of the detailed detector conditions during data taking. The fully simulated MC09 PYTHIA6 samples are used to derive the detector corrections for these measurements. Particular care is taken to ensure that these corrections are not dependent on the particular generated distributions. A technique to emulate the impact of operating the SCT in standby was developed in simulation; this corrects the Monte Carlo method

[2] PYTHIA version 6.4.21

without re-simulation by modifying the hit-cluster algorithm during reconstruction of the silicon detector data.

In order to compare the current (using ATLAS MC09 tune) measurements with different phenomenological models describing minimum-bias events, some additional MC samples were generated using different tunes:

- the new ATLAS Minimum Bias Tune 1 (AMBT1) PYTHIA6 tune.
- the DW [35] PYTHIA6 tune, which describes the CDF RUN II underlying event and Drell-Yan data. This tune uses the old virtually ordered shower algorithm.
- the PYTHIA8 generator [3] was used for comparison with the default tune. It is used as the diffraction model to produce much harder p_{T} and n_{ch} spectra for the single- and double-diffractive contributions.
- the PHOJET generator [4] [28] is used as an alternative model to PYTHIA. This model describes the low-p_{T} physics using the the Dual Parton Model (DPM) [29–32] with perturbative QCD in order to describe hard and soft processes in an unified way. It describes low-p_{T} physics using the two-component PHOJET generator but relies on PYTHIA [5] to simulate the fragmentation of partons.

[3] PYTHIA version 8.130
[4] PHOJET version 1.12.1.35
[5] PYTHIA version 6.1.15

5.1.4.2 Tuning Parameters

5.1.4.2.1 Multiple parton interactions (MPI)

The multiple parton interaction rate is allowed to be changed in PYTHIA by the user. The selection of MPI is connected to the showering strategy of the event generator such as virtually ordered showering or (the newer) interleaved p_{T}-ordered showering. The size of the MPI component in PYTHIA 6 is modeled by a cut-off parameter (new model) for the p_{T} of the $2\rightarrow 2$ scattering process in addition to the hard interactions. This cut-off parameter is fixed at a reference energy, in general 1.8 TeV. The cut-off parameter at this reference energy scale is called PARP(82). The cut-off parameter is then rescaled for other center-of-mass energies using an additional parameter PARP(90). PARP(90) is calculated using Equation 5.2. The MPI prediction rate in LHC collisions is still one of the major uncertainties in the PYTHIA model.

$$p_T^{min} = PARP(82)(\frac{\mathrm{E}}{1.8\mathrm{TeV}})^{\mathrm{PARP(90)}} \tag{5.2}$$

5.1.4.2.2 Color Reconnection

The average of charged particles' transverse momentum, $< p_{\mathrm{T}} >$, might be expected to be independent of the number of charge particles, N_{ch}. In reality, the tracks in high-multiplicity events have higher mean p_{T} than those of low-multiplicity events. This is due to Color Reconnection (CR) where color reconnection occurs between parton interactions and beam remnants. Therefore, by adding a parameter in the PYTHIA model that is very sensitive to the correlation between p_{T} and charged particle mul-

tiplicity, an appropriate tuning can be applied for color reconnection. Figure 5.2 [26] shows the mean p_{T} distribution after the tuning is applied.

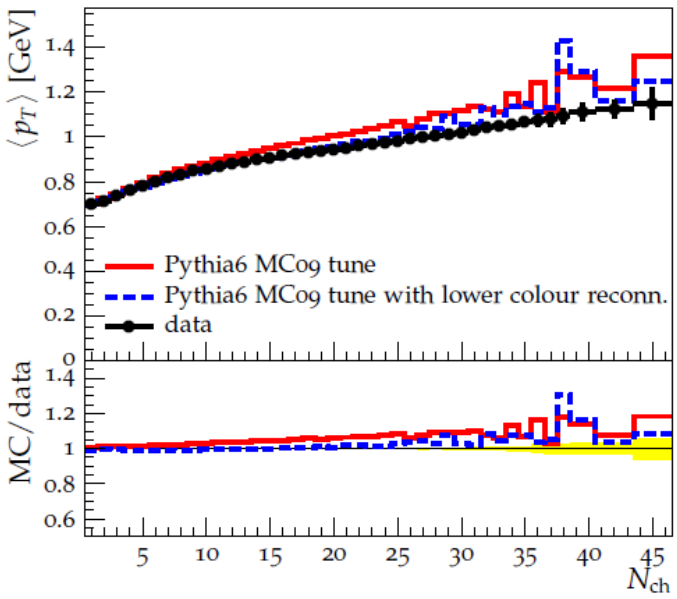

Figure 5.2: Mean transverse momentum of charged particles $< p_{\mathrm{T}} >$ as a function of the multiplicity N_{ch} predicted by PYTHIA with the ATLAS MC09 tune (red solid line) and the MC09c tune (blue dashed line) with a lowered color reconnection probability.

5.1.4.2.3 Initial and Final State Radiation (ISR and FSR)

Parameters describing the final state radiation, hadronization and fragmentation are not tuned, but are constrained by many LEP results. For the initial state radiation, the cut-off scale parameter, PARP(62), and the cut-off scale for momentum smearing in primordial kT, PARP(93), were considered and tuned using the Drell-Yan p_{T} spectrum. This tuning did not have a large impact on multiplicity or underlying event distributions.

5.1.4.3 Recent Tuning

The above discussed parameters are tuned to make better agreement between measured distributions and predicted distributions, and there are several tunes that have been applied for various experiments. The charged particle multiplicity distributions of the ATLAS experiment can be compared to six such tuning strategies. The Perugia0 tune [36] was introduced by tuning PYTHIA 6.4 to minimum bias measurements from UA5 and CDF. This tune uses the p_{T}-ordered (new model) parton shower algorithm which is used in the current MPI model. The DW tune was tuned using PYTHIA 6.2 to describe the CDF RUN II underlying and Drell-Yan events. It uses the old model of virtually-ordered showering. Minimum bias measurements were not used in DW tune and underlying events measurements were not used in the Perugia0 tune. Thus, both Perugia0 and DW tunes collectively describe the properties of both underlying event and minimum bias measurements for the same process. The DW and Perugia0 tunes successfully describe the properties of underlying event and minimum bias event respectively.

Recently ATLAS introduced a number of tunes using the PYTHIA MC generator such as MC09, MC09c and AMBT1. All the tunes are based (before introducing specific tunes MC09, MC09c and AMBT1) on underlying event and minimum bias measurements from CDF (Run I and Run II) and D0 di-jet angular correlations. There were 16 parameters used to tune but there was very little impact from many of these parameters. The new ATLAS tune of Monte Carlo 2009 (MC09) [37] was derived in 2009 prior to LHC real data. This tune has a big impact due to adjustments to

parameters PARP(82) and PARP(90) for charged particle multiplicity distributions. There is another tune (MC09c) that was introduced right after introduction of the CDF measurements of the dependence of $< p_{\mathrm{T}} >$ on N_{ch} [38]. The CDF measurements were sensitive to the color reconnection parameter. So the tune MC09c is very similar to MC09 except in the introduction of $< p_{\mathrm{T}} >$ vs. n_{ch} which reduced the tuned value of PARP(78). There is a latest tune, AMBT1, using PYTHIA, introduced after the measurements of the charged particle multiplicity at 900 GeV and 7 TeV from LHC data. A new parameter, PARP(77), was introduced in the AMBT1 tune which improves the $< p_{\mathrm{T}} >$ vs. n_{ch} distribution by suppressing the color reconnections. Table 5.2 [39] summarizes the parameter values in different tunes.

Parameter	Related model	MC09c value	scanning range	AMBT1 value
PARP(90)	MPI (energy extrapolation)	0.2487	$0.18 - 0.28$	0.250
PARP(82)	MPI (p_T^{min})	2.31	$2.1 - 2.5$	2.292
PARP(84)	MPI (core of matter overlap)	0.7	$0.0 - 1.0$	0.651
PARP(83)	MPI (matter fraction in core)	0.8	fixed	0.356
PARP(78)	CR strength	0.224	$0.2 - 0.6$	0.538
PARP(77)	CR suppression	0.0	$0.25 - 1.15$	1.016
PARP(93)	Primordial kt	5.0	fixed	10.0
PARP(62)	ISR cut-off	1.0	fixed	1.025

Table 5.2: Comparison of MC09c and new optimized parameters (AMBT1). The range for parameter variations in AMBT1 are also given.

5.1.5 Data and Event Selection

The data used in this analysis were recorded during December 6 -15, 2009 at $\sqrt{s}$ = 0.9 TeV and between March 30 and April 7, 2010 at $\sqrt{s}$ = 7 TeV. During the data taking, the inner detector was fully operational, with more than 97% of the Pixel detector, 99% of the SCT and 98% of the TRT functioning normally with the solenoid magnet on.

Events were collected from colliding proton bunches in which the MBTS trigger recorded one or more counters above threshold in either end cap. During the running periods mentioned above, an integrated luminosity of approximately 7 μb^{-1} at $\sqrt{s}$ = 0.9 TeV and 190 μb^{-1} at $\sqrt{s}$ = 7 TeV was accumulated. The maximum instantaneous luminosity was approximately 1.9×10^{27} cm^{-2} s^{-1}. The probability of additional interactions in the same bunch crossing was estimated to be of the order of 0.1%. In order to perform an inclusive-inelastic measurement, no further requirements beyond the MBTS trigger and inner detector information were applied in the event selection. In order to compare the tracking performance with the SCT fully operational and at standby, the SCT was kept in standby for part of a run at $\sqrt{s}$ = 0.9 TeV. [6]

5.1.5.1 Track Selection in Different Phase-Space Regions

There are three different track selections (phase-space regions), listed below, that are used in this analysis to provide different track contributions. These different selections are also used to investigate different relative amounts of non-diffractive events.

[6] The rest of the run, in which the SCT was at nominal voltage was used in the $\sqrt{s}$ = 0.9 TeV analysis and was included in the first ATLAS publication.

1. At least one charged particle in the kinematic range $|\eta| < 2.5$ and $p_{\mathrm{T}} > 500$ MeV.

2. At least two charged particles in the kinematic range $|\eta| < 2.5$ and $p_{\mathrm{T}} > 100$ MeV.

3. At least six charged particles in the kinematic range $|\eta| < 2.5$ and $p_{\mathrm{T}} > 500$ MeV.

The first selection allows us to see the evolution as a function of center-of-mass energy since it is used for all three energies: $\sqrt{s} = 0.9$, 2.36 and 7 TeV. (Since there was only one run at the center-of-mass energy of $\sqrt{s} = 2.36$ TeV it will not be discussed further). It also allows us to tune the MC parameters that determine the energy extrapolation method. Since the second selection has a very loose cut on p_{T} it is used to measure the most inclusive charged particle spectra. The second selection is also used to extrapolate to p_{T} =0.

The third selection is very similar to the first one but requires a higher number of charged particles. The requirement of more charged particles in the third selection reduces the fraction of diffractive events in the sample. This third selection is the one used to produce the new AMBT1 tune.

The second and third selections are used only for $\sqrt{s} = 0.9$ and 7 TeV center-of-mass energies.

The fraction of diffractive events varies widely for different Monte Carlo models and highly depends on the above selection criteria. The fraction of diffractive events at $\sqrt{s} = 7$ TeV are 21% and 14% for PYTHIA6 and PYTHIA8 respectively and 14% for PHOJET using the default cross sections of the generators for the most inclusive

selection of $n_{\mathrm{ch}} \geq 2$, $p_{\mathrm{T}} > 100$ MeV, $|\eta| < 2.5$. For the selection where less diffraction is expected, for $n_{\mathrm{ch}} \geq 6$, $p_{\mathrm{T}} > 500$ MeV, $|\eta| < 2.5$, the fractions vary significantly between the models; PYTHIA6 predicts 0.4%, PYTHIA8 10.1% and PHOJET predicts 7.9% diffractive events passing our event selection. The large difference in the number of diffractive events for different models motivates us not to make model-dependent corrections.

5.1.6 Event Selection

The events are selected to reduce background events and non-primary tracks contributions. The following criteria are required for a good event:

- A single-arm, single counter L1 MBTS trigger,
- A primary vertex [40] reconstructed using beam spot and at least two tracks, each with:
  - $p_{\mathrm{T}} > 100$ MeV,
  - The transverse impact parameter (transverse distance of closest approach to the beam-spot) $|d_0^{\mathrm{BS}}| < 4$ mm,
- a minimum number of tracks, depending on the particular phase-space, as explained in Section 5.1.7.

5.1.7 Track Selection Criteria

The track selection consists of several components of track reconstruction variables and also mainly depends on the track transverse momentum. The following criteria were required for good track selection:

- In addition to the primary vertex selection where at least two tracks are needed, we required a minimum number of tracks depending on the transverse momentum:
  - $p_{\mathrm{T}} > 100$ or 500 MeV,
  - $|\eta| < 2.5$,
  - a hit in the inner-most layer of the Pixel detector (B-layer, layer 0) if a hit is expected [7],
  - a minimum of one Pixel hit,
  - a minimum of two, four or six SCT hits for tracks with momentum $p_{\mathrm{T}} <$ 200, $200 < p_{\mathrm{T}} < 300$ and $p_{\mathrm{T}} > 300$ MeV, respectively ,
  - transverse and longitudinal impact parameters calculated with respect to the event primary vertex $|d_0| < 1.5$ mm and $|z_0| \cdot \sin\theta < 1.5$ mm, respectively,
  - a χ^2 probability larger than 0.01 for tracks with $p_{\mathrm{T}} > 10$ GeV to remove tracks with mis-measured track p_{T} due to alignment and nuclear interactions.

[7] A hit is expected if the extrapolated track crosses an active region of a Pixel module that has not been disabled.

These track selections are used in measuring multiplicity distributions. The track multiplicity of these selected tracks within an event is defined to be n_{sel}. Table 5.3 shows the total number of events and tracks for all selections considered.

Phase-space		$\sqrt{s} = 0.9$ **TeV**		$\sqrt{s} = 7$ **TeV**	
n_{ch}	**min** p_{T} **(MeV)**	**Events**	**Tracks**	**Events**	**Tracks**
2	100	357,523	4,532,663	10,066,072	209,809,430
1	500	334,411	1,854,930	9,619,049	97,224,268
6	500	124,782	1,287,898	5,395,381	85,587,104

Table 5.3: Number of events and tracks for the three selections and energies considered in this paper.

5.1.7.1 Tracking Algorithms for $\sqrt{s} = 0.9$ TeV and $\sqrt{s} = 7$ TeV

There are several tracking algorithms in ATLAS that have been used to reconstruct the tracks. The final track collection can be due to a single tracking algorithm or can come from combinations of more than one tracking algorithms. There are two basic fundamental algorithms that have been used in ATLAS software [41] such as *Inside-Out* and backtracking. The *Inside-Out* algorithm reconstructs the tracks from the collision point by adding the hits from each inner sub-detector where tracks move in an outwards direction. The backtracking algorithm adds the hits from TRT while moving toward the center of the detector. The *Inside-Out* algorithm reconstructs the primary particles more efficiently while the backtracking algorithms reconstruct the non-primaries (secondary and fakes) more efficiently.

In the previous ATLAS measurement of charged particle multiplicities at $\sqrt{s} =$

0.9 TeV [1,2,42], where $p_{\mathrm{T}} \geqslant 500$ MeV was required, the tracks were reconstructed by the standard *Inside-Out* pattern recognition sequence [41,43,44].

For this analysis, the transverse momentum requirement was lowered to $p_{\mathrm{T}} \geqslant 100$ MeV. In addition to using the previous algorithm with lower momentum threshold, another new reconstruction algorithm, the *LowPt* algorithm, was also used to recover some low-p_{T} tracks that were not found by the standard *Inside-Out* algorithm.

The table 5.4 shows the main pattern recognition settings for the *Inside-Out* and *LowPt* algorithms. The *LowPt* algorithm was able to reconstruct around 60% of the tracks from 100 MeV to 150 MeV. This is mostly due to the tracks having too low transverse momentum to go far enough in the SCT detector to satisfy the silicon hit requirements of the original algorithm. The fraction of reconstructed tracks by the *Inside-Out* algorithm decreases rapidly with lower transverse momentum, reaching less than 2% at 200 MeV. Figure 5.3 [45] shows the tracking reconstruction efficiency using the *Inside-Out* and *LowPt* tracking algorithms as a function of transverse momentum, p_{T}, of the tracks for $\sqrt{s} = 0.9$ TeV.

In addition to both *Inside-Out* and *LowPt* algorithms another algorithm, *VeryLowPt* algorithm, was introduced that reaches down to a minimum transverse momentum of 50 MeV. The *LowPt* (down to 100 MeV) and *VeryLowPt* (down to 50 MeV) algorithms run with relaxed requirements on the number of hits and holes to allow for the low track radii that can be reached at these low momenta. In this study, the *VeryLowPt* tracking algorithm has not been used since the minimum transverse momentum of the tracks is 100 MeV.

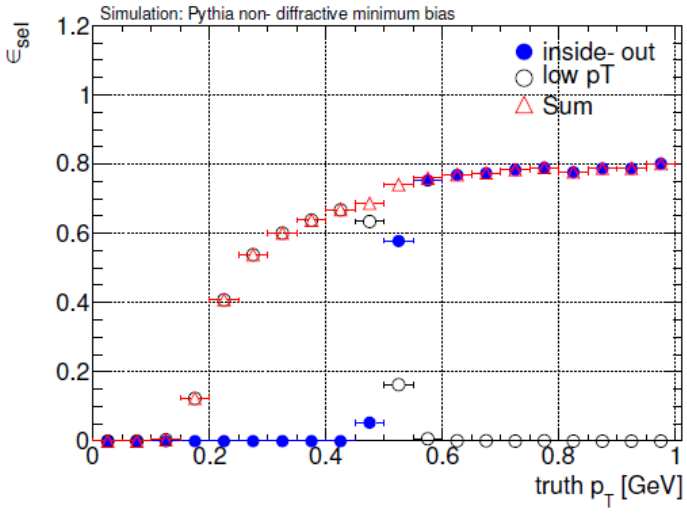

Figure 5.3: The tracking efficiency as a function of primary p_{T} for the *Inside-Out* and *LowPt* tracking algorithms for $\sqrt{s} = 0.9$ TeV.

Tracking Parameter	*Inside-Out*	*LowPt*
p_{T} threshold	100 MeV	100 MeV
z	≤ 250 mm	≤ 250 mm
η	≤ 2.7	≤ 2.7
d_0	≤ 10mm	≤ 100mm
$N_{\mathrm{Si\ Hits}}$	≥ 7	≥ 5
$N_{\mathrm{Pixel\ Hits}}$	No cut	≥ 2
$N_{\mathrm{Shared\ Hits}}$	≤ 3	≤ 2
$N_{\mathrm{Pixel\ Holes}}$	≤ 2	≤ 1
$N_{\mathrm{SCT\ Holes}}$	≤ 2	≤ 2
$N_{\mathrm{Double\ Holes}}$	≤ 1	≤ 1

Table 5.4: The major parameter selection cuts for *Inside-Out* and *LowPt* tracking algorithms.

5.1.8 Validation of new Tracking algorithms

The new tracking algorithms were used in this experiment as explained in Section 5.1.7.1. We have validated the new tracking algorithms by comparing the transverse momentum (p_{T}) and the transverse momentum resolution at high p_{T}in the data

with MC simulations. The transverse momentum and impact parameters of the tracks are shown for $p_{\mathrm{T}} >$ 500 MeV at $\sqrt{s} = 7$ TeV in the Figure 5.4 [2].

Figure 5.4 shows that the distribution of silicon hits clearly is in good agreement between data and MC simulation. Since this analysis has the threshold transverse momentum of 100 MeV, we also validated the tracks with $100 < p_{\mathrm{T}} < 500$ MeV at both $\sqrt{s} = 7$ TeV and $\sqrt{s} = 0.9$ TeV [39]. Figure 5.5 [39] compares the data and the simulation for basic parameters of the tracks such as SCT hits (a), pixel hits (b), the transverse impact parameter (c) and the longitudinal impact parameter multiplied by $sin\theta$ (d). All these variables have very good agreement between data and simulation. Figure 5.5 ($100 < p_{\mathrm{T}} <$500 MeV) and Figure 5.4 ($p_{\mathrm{T}} > 500$ MeV) show similar behavior.

The χ^2 cut mentioned in Section 5.1.7 is used to remove the mis-aligned tracks. The performance of the χ^2 cut was verified by comparing generated p_{T} verses the reconstructed p_{T} using Monte Carlo samples. Figure 5.6(a) shows that most of the tracks transverse momenta are highly correlated while some of the low p_{T} tracks are poorly reconstructed. The effect of the uncorrelated tracks comes from non-Gaussian tails of the track momentum resolution. Since the number of the events in the tail region is very small compared to the total number of events, the p_{T} spectrum falls steeply. In the high p_{T} region ($30 < p_{\mathrm{T}} <$50 GeV) this tail constitutes about 30% of the tracks. As no Monte Carlo models can be trusted to describe such non-Gaussian tails with accuracy, it was necessary to find a cut that could remove most of such mis-measured tracks [39]. χ^2 probability turned out to be a good variable to remove

these mis-aligned tracks as shown in Figure 5.6(b). Figure 5.6(b) clearly shows that the χ^2 probability of the mis-aligned tracks is very low. So a very low χ^2 probability cut of 0.01 was good enough to remove the most mis-aligned tracks in MC as shown in Figure 5.7. There were only 6% of mis-aligned tracks in the reconstructed p_{T} regions between 30 and 50 GeV after the χ^2 probability cut was applied.

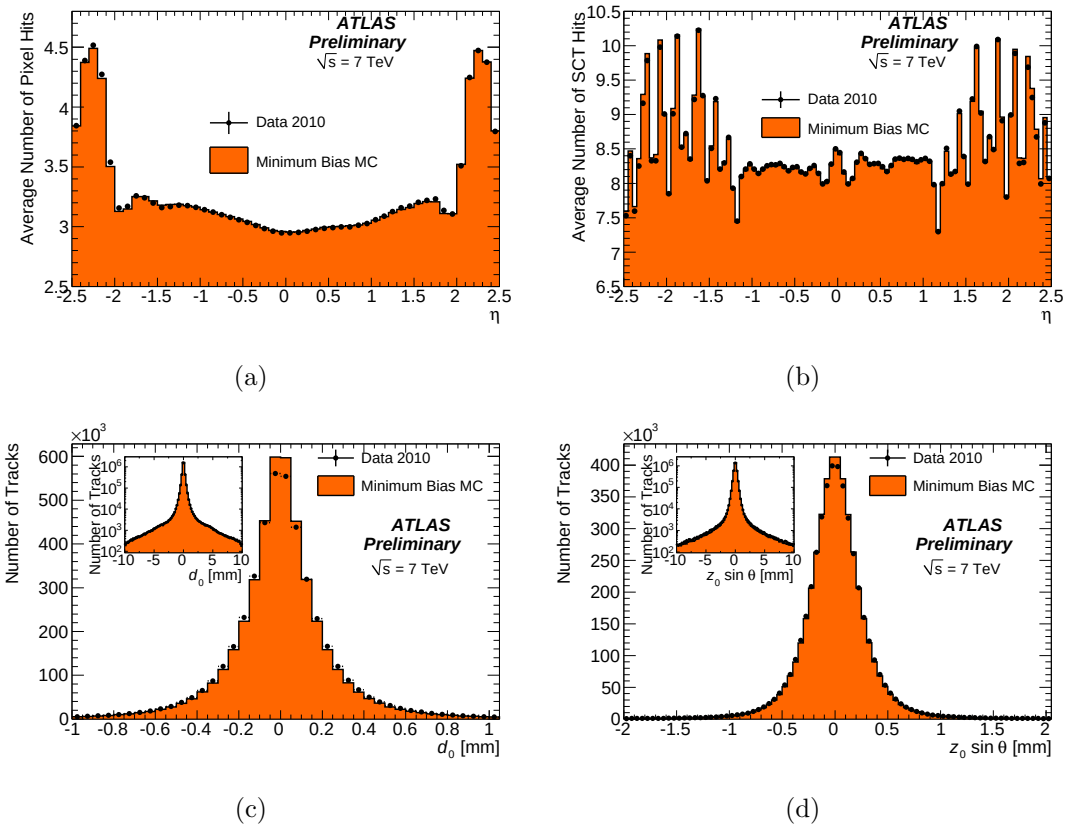

Figure 5.4: The number of SCT hits (top right) and number of Pixel hits (top left) as a function of *eta* at $\sqrt{s} = 7$ TeV with $p_{\mathrm{T}} > 500$ MeV. The bottom plots compare the traverse(left) and longitudinal(right) impact parameters in data and simulations at $\sqrt{s} = 7$ TeV with $p_{\mathrm{T}} > 500$ MeV

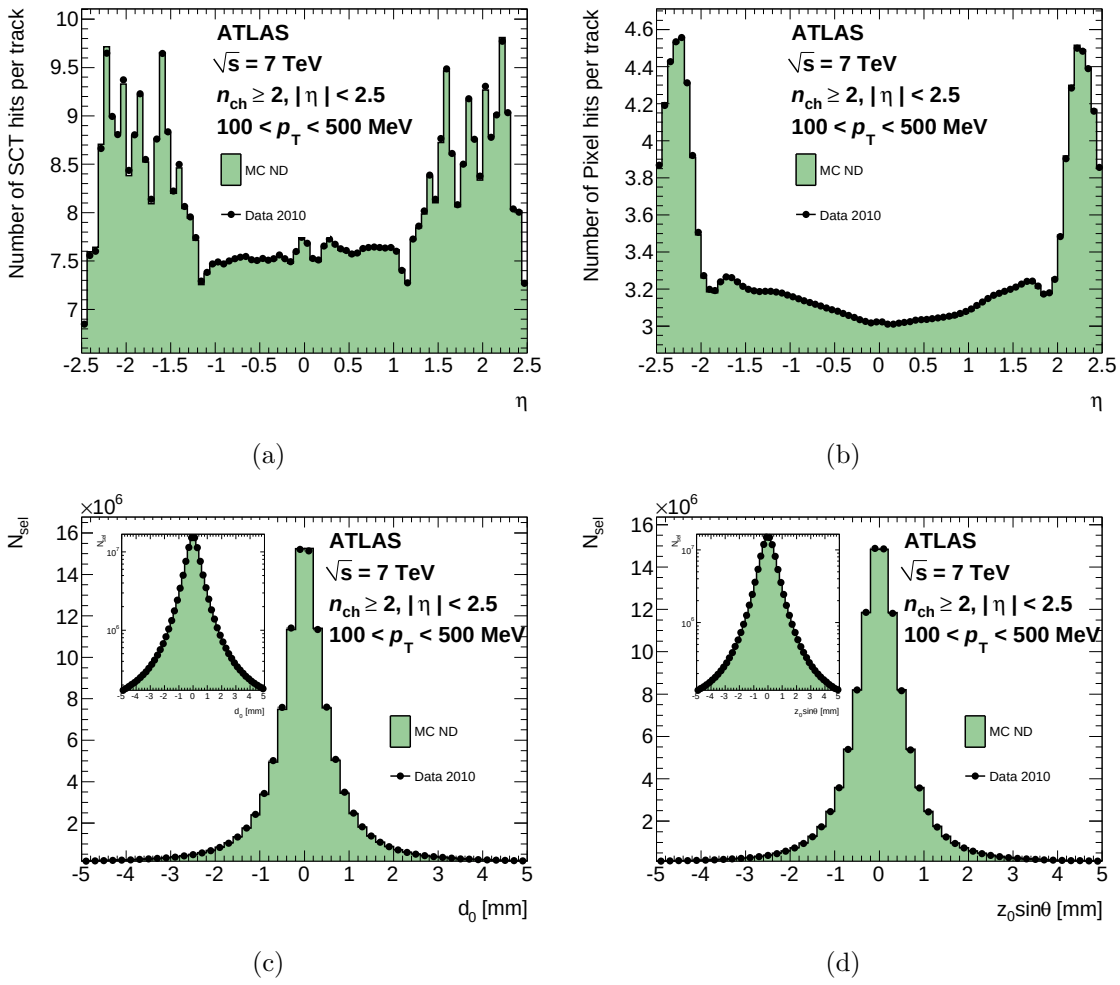

Figure 5.5: Comparison between data and simulation at $\sqrt{s} = 7$ TeV for tracks with transverse momentum between 100 and 500 MeV: the average number of silicon hits on track as a function of η in the SCT (a) and Pixel (b) detectors, the transverse impact parameter (c) and longitudinal impact parameters multiplied by $sin\theta$ (d). The inserts for the impact parameter plots show the log-scale plots. The p_{T} distribution of the tracks in non-diffractive (ND) MC is re-weighted to match the data and the number of events is scaled to the data.

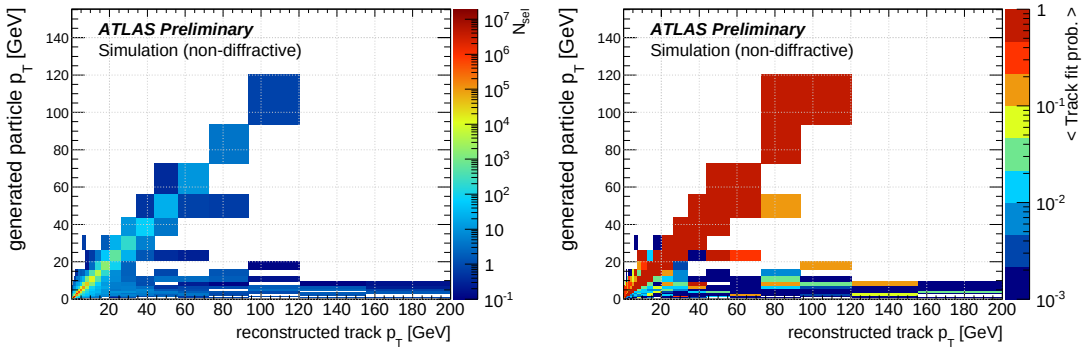

Figure 5.6: (a) MC distribution of the particle p_{T} vs the p_{T} of the reconstructed tracks. The color-scale (z-axis) indicates the number of entries, in a log-scale. Reconstructed tracks that cannot be matched to any generated particle are not displayed. (b) MC distribution of the mean track fit χ^2 probability (z-axis) vs particle p_{T} vs reconstructed track p_{T}.

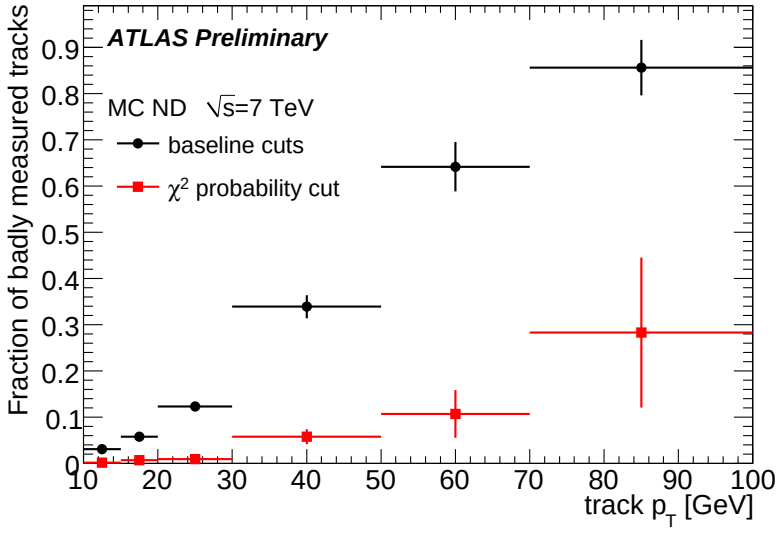

Figure 5.7: Fraction of tracks as a function of the reconstructed track p_{T}in simulation, where the reconstructed p_{T} differs by more than 50% from the particle p_{T} before (black) and after (red) the track fit χ^2 probability cut at 0.01. All other track selection cuts are applied.

5.1.8.1 Track Length Requirement

The hit efficiency of the silicon detectors (Pixel and SCT) is almost 100% since few modules were turned off during collisions. Therefore, the transverse momentum of the charged particle is the major parameter to use to determine how far the particle can reach out in to the tracking volume. [8]

However, the majority of charged particles from minimum bias events are hadrons. These hadrons can interact with the detector material which can significantly shorten the expected track length. The momentum resolution of the tracks gets worse due to this shorter track length and this shorter track length will be a dominant contributor to the migration effect of low p_{T} particles to be measured as high p_{T} tracks. The reconstructed tracks due to this migration effect with 50% difference in p_{T} are known as badly measured tracks or mis-aligned tracks, and the transverse momentum, p_{T}, of such badly reconstructed tracks differ by 50% from that of simulated tracks. Figure 5.8 (left) shows the badly measured tracks due to the migration effect.

This migration effect was suppressed by a strict requirement on the track length in terms of the SCT hit requirement depending on the reconstructed tracks as described below (this selection is already included in Section 5.1.7). [9]

- ≥ 2 SCT hits if the track is measured in the range $100\,\mathrm{MeV} < p_{\mathrm{T}} \leq 200\,\mathrm{MeV}$
- ≥ 4 SCT hits for $200\,\mathrm{MeV} < p_{\mathrm{T}} \leq 300\,\mathrm{MeV}$

[8] It also depends on other kinematic parameters of the particle: its production vertex, and the direction of the initial particle momentum, since the geometrical detector setup allows different numbers of crossed detection layers and thus leads to a different number of average hits. [45]

[9] "Studies have shown that an SCT hit requirement is very similar to a layer requirement. Since the SCT hit requirement is simpler to access in the analysis data format this has been favored over the layer requirement" [45]

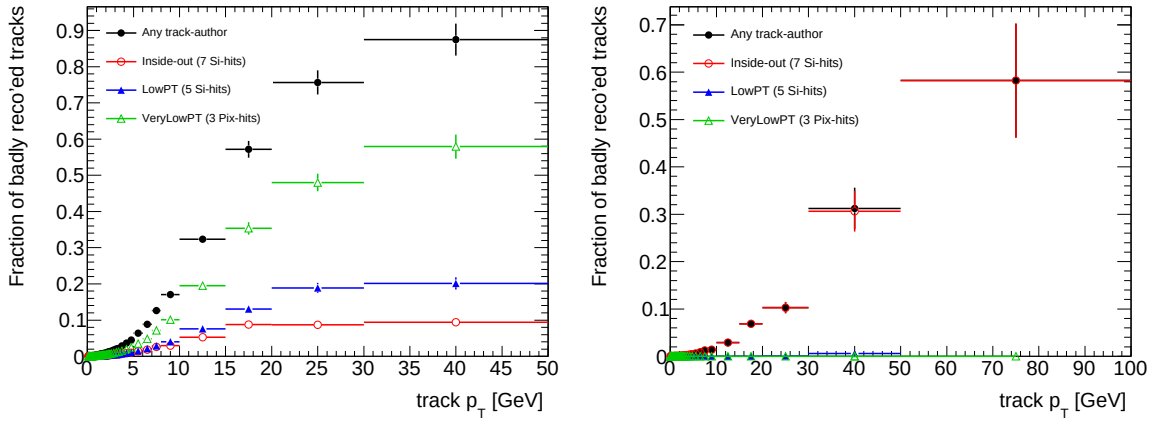

(a) (b)

Figure 5.8: Fraction of badly measured tracks as a function of reconstructed track p_{T}, without (left) and with (right) the p_{T} dependent SCT hit requirements. The fraction is split up into the single components from the different track reconstruction algorithms. Badly measured tracks are defined by a reconstructed p_{T} that is different from the generated p_{T} by at least 50%.

- ≥ 6 SCT hits for $p_{\mathrm{T}} > 300$ MeV

Figure 5.8 (right) shows the suppression of badly measured tracks after the SCT hit requirements. The suppression due the SCT hit requirement is very clear up to 20 GeV. The total of fraction badly measured tracks is reduced e.g. the total fraction of badly measured tracks is reduced from 90% to 30% in the p_{T} bins between 30 and 50 GeV. The remaining badly measured tracks are mainly dominated by the *Inside-Out* tracking algorithm. The remaining badly measured tracks with high reconstructed transverse momenta have been investigated in detail and are treated with an additional track quality requirement of χ^2 probability cut. Details of the requirement of χ^2 probability are discussed in Section 5.1.8.

The suppression of badly measured tracks reduces the average number of hits on tracks as a function of traverse momentum. Figure 5.9 shows the reconstructed

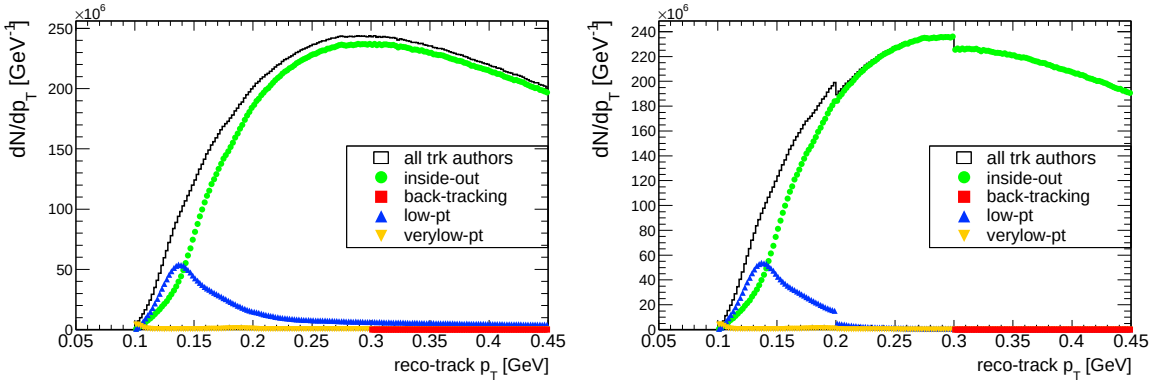

(a) (b)

Figure 5.9: Distribution of reconstructed track p_{T} in MC for the various track algorithms, with 2 (left) and 2/4/6 (right) SCT hit requirement at 100/200/300 MeV.

track p_{T} spectrum for the different track algorithms with and without the SCT hit requirement cuts. There is a reconstruction efficiency drop at certain transverse momentum values and it is clearly visible where the length requirement changes. There are other effects due to the SCT hit requirements in non-primary track suppression where these tracks are not associated with a primary vertex as shown in Figure 5.10. The track length suppression results in the non-primary particles at $p_{\mathrm{T}}>$ 400 MeV being completely dominated by the *Inside-Out* tracking algorithm. The detailed study of non-primary tracks is explained in section 6.2.9.

5.1.8.2 Impact Parameter and Pixel Hit Requirement

The impact parameter, the distance of closest approach to the beamline, with respect to the primary vertex is one of the strong discriminating variables between primary tracks and non-primary or secondary tracks.

The production of non-primary particles are induced by hadronic interaction of particles with the detector material or originated from the decay of neutral particles

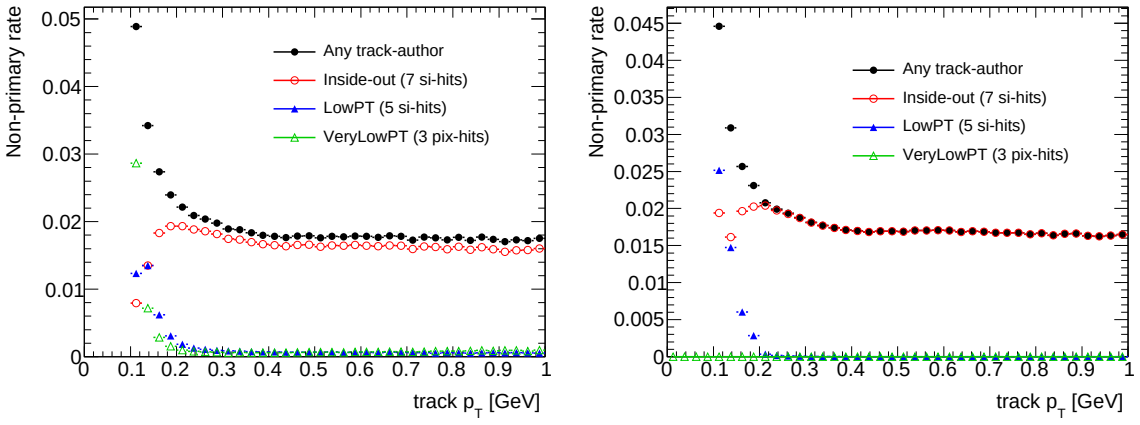

(a) (b)

Figure 5.10: Fraction of tracks that are not associated to primary particles as a function of p_{T} without (left) and with (right) the SCT hit requirement.

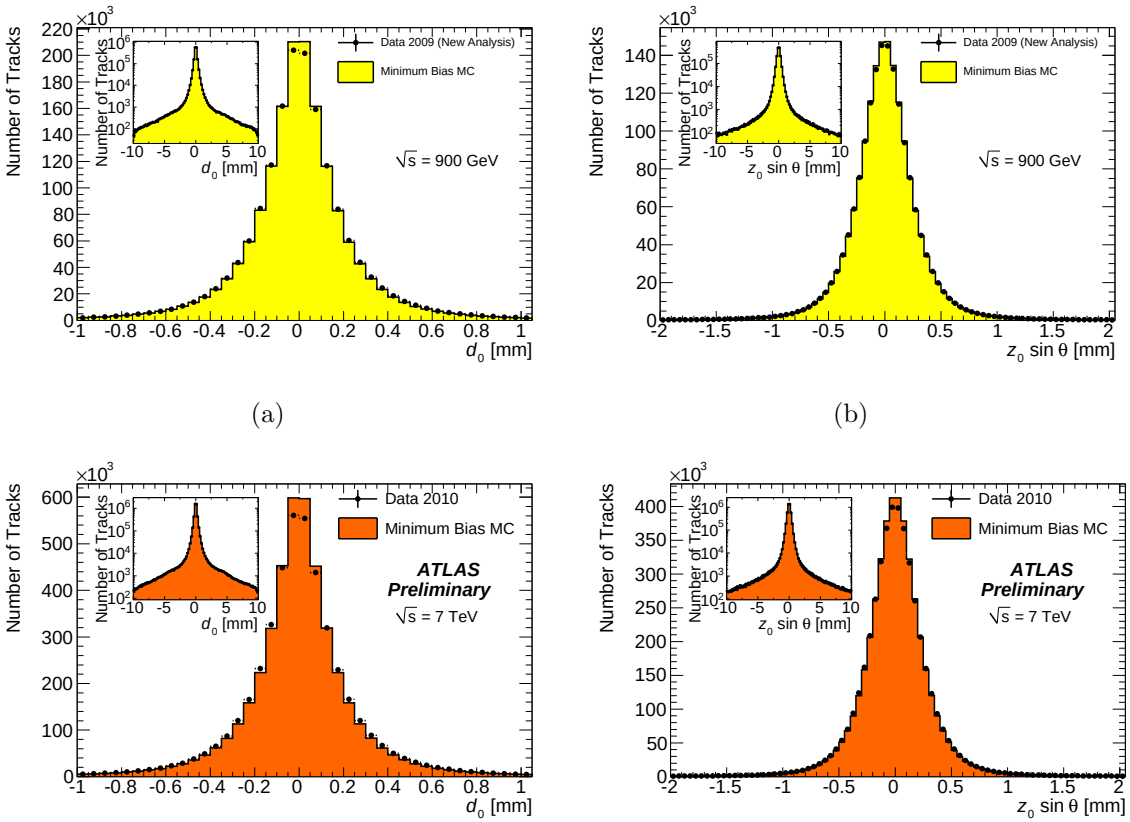

(a) (b)

(c) (d)

Figure 5.11: Transverse and longitudinal impact parameter distribution with respect to the primary vertex in data and simulation for tracks with p_{T}> 500 MeV. (a) and (b) are for $\sqrt{s} = 0.9$ TeV and (c) and (d) are for $\sqrt{s} = 7$ TeV.

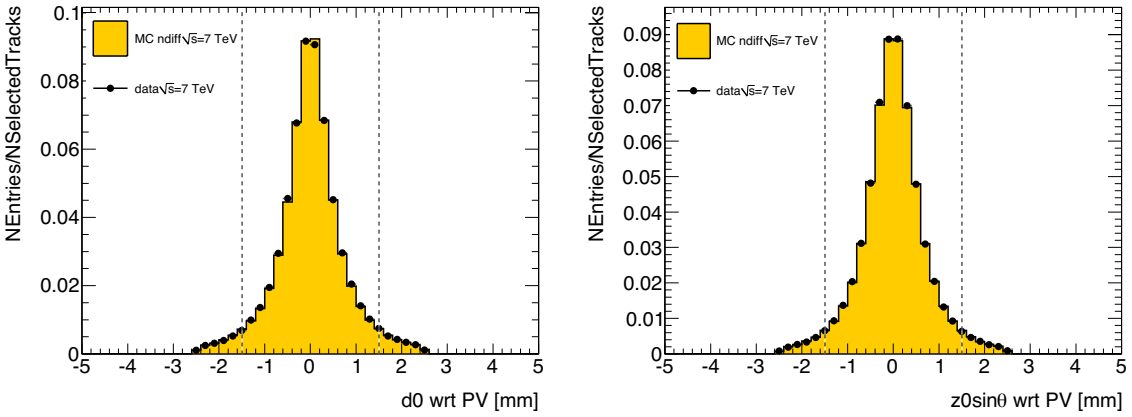

Figure 5.12: Transverse and longitudinal impact parameter distribution with respect to the primary vertex in data and simulation for tracks with p_{T} below 500 MeV. The vertical dashed lines indicate the chosen cut parameters.

such as decays of pions and kaons in flight typically with large radii. The transverse impact parameter d_0 of these non-primary particles is in general large, when extrapolating non-primary particles' tracks back to the primary vertex, they bend far away from the primary vertex.

In the case of the longitudinal component of impact parameter, z_0, there is similar discriminating power as d_0 but with less track bending. The resolution of the impact parameters is studied with $p_{\mathrm{T}} > 500$ MeV for the previous analysis [1, 2] as shown in Figure 5.11. For low momenta, the multiple scattering of the trajectory increases dramatically. Since the multiple scattering contribution tends to increase with the inverse momentum, this contribution dominates the impact parameters of the tracks at low momenta. The transverse and longitudinal impact parameter with respect to the primary vertex of tracks are shown in Figure 5.12 for tracks with p_{T} below 500 MeV.

A study that aims for high efficiency would require p_{T} dependent cuts on the

impact parameters. However, as the momentum spectrum of particles in minimum bias events are dominated by low p_{T} particles, this is of minor concern for this study. In contrast, the contamination of tracks that originate from particles induced by material interaction or so-called ghost tracks (sometimes referred to as fakes) that are random combinations of hits created by different particles cause more distortion to the measured particle spectrum.

Various cut sets on the impact parameter distributions with respect to the primary vertex have been studied. Finally, the requirements $|d_0| < 1.5\,\mathrm{mm}$ and $|z_0 \sin\theta| < 1.5\,\mathrm{mm}$ for the entire momentum range of interest have been chosen. This choice has been made by considering the cut efficiency, the contamination of non-primaries and the potential complexity of p_{T} dependent impact parameter cuts, that would introduce yet another discontinuity and resolution effect.

Another method to suppress the contamination from non-primaries is requiring the first pixel layer (also referred to as B-layer) hit. Requiring a B-layer hit significantly improved the estimation of the secondary fraction in the measured spectrum by means of a side-band template fit to the impact parameter distributions [4]. The agreement on the number of B-layer hits is good and the systematic error from a wrong modeling is estimated by the comparison of the cut efficiency. Thus, a B-layer hit is required, if the track had passed an active module[10]. In the case that the track had not passed an active B-layer module, or if the calculated intersection is either ambiguous or close to the inactive area, a single pixel hit is required.

[10]This can be tested in the track reconstruction using the extrapolation algorithm and is stored as a track quality parameter.

5.1.9 Tracking Reconstruction Efficiency

The track reconstruction efficiency is defined as the tracks passing through the detector volume that are reconstructed as good tracks divided by total number of generated tracks as in Equation 5.3.

$$\epsilon_{\rm trk}(p_{\rm T},\eta) \;=\; \frac{N_{\rm rec}^{\rm matched}(p_{\rm T},\eta)}{N_{\rm gen}(p_{\rm T},\eta)}, \tag{5.3}$$

where $p_{\rm T}$ and η are generated particle transverse momentum and pseudo rapidity, $N_{\rm rec}^{\rm matched}(p_{\rm T},\eta)$ is the number of reconstructed tracks matched to a generated charged particle and $N_{\rm gen}(p_{\rm T},\eta)$ is the number of generated charged particles in that bin [4].

This efficiency is calculated using simulated Monte Carlo events. Therefore, the systematic uncertainties can be calculated by comparing the data and MC simulation. The track efficiency depends on several factors such as the set of cuts to define the primary particles in the algorithm and the definition of non-primary particles in the generator.

5.1.10 Monte Carlo Truth Matching of the tracks

It is necessary to determine whether a generated particle is actually reconstructed to calculate the primary tracking efficiency. Mapping the reconstructed tracks to truth charged particles (generated particles) is known as truth matching. The definition of a good charged track can be defined by a track formed by combinations of hits from one charged particle that reproduce the momentum of that particle. These tracks can be matched to generated particles. The tracks that are formed by random combinations

of hits (from more than one particle) that cannot re-produce the momentum of the generated particles are known as fake tracks. Some tracks are formed by single particle hits but don't reproduce the momentum of the generated particle. These tracks are referred to badly reconstructed tracks. There are tracks which are formed by multiple particles but produce the momentum of a single particle. This is mostly due to quasi-elastic decays when the primary particle decays to secondary particles (non-primary) which have the same direction as that of the primary.

Two types of truth matching methods were used in this analysis; the hit based matching and the cone based matching.

5.1.10.1 The Hit Based Matching

This method associates reconstructed tracks and the particles based on comparing the number of hits on the track that correspond to the number of hits produced by the generated particle. A matching probability, the fraction of matched hits, is "defined as the ratio of number of hits which are common to a given track and the corresponding particles and the number of hits which form the track" [46]

The Matching probability, a function of the number of hits from different sub-detectors, is given by following equation with different weights.

$$P_{\text{match}} = \frac{10 \cdot N_{\text{Pix}}^{\text{common}} + 5 \cdot N_{\text{SCT}}^{\text{common}} + 1 \cdot N_{\text{TRT}}^{\text{common}}}{10 \cdot N_{\text{Pix}}^{\text{track}} + 5 \cdot N_{\text{SCT}}^{\text{track}} + 1 \cdot N_{\text{TRT}}^{\text{track}}} \tag{5.4}$$

where

- $N_{\text{det}}^{\text{common}}$ is the number of hits in the sub-detector which are part of both the

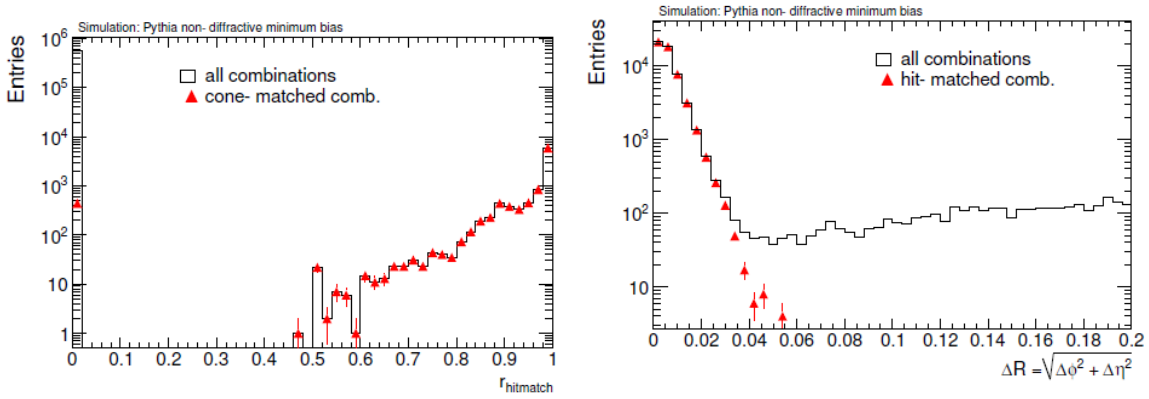

(a) (b)

Figure 5.13: Simulated distribution of hit-match ratio $r_{hitmatch}$, or matching probability, P_{mathc} (a) and angular distance ΔR (b) between selected reconstructed tracks and primary truth particles. The black histograms show the distributions for all possible matches between selected tracks and primary truth particles, while the red filled triangles show the hitmatch (angular distance) distribution for those matches that satisfy the $\Delta R < 0.05$ ($r_{hitmatch}$ >0.55) requirement.

truth and reconstructed tracks (Common hits)

- $N_{\text{det}}^{\text{track}}$ is the number of reconstructed hits per track
  - det = [Pix, SCT, TRT]

Since the average number of hits per track and contribution to the track parameter from each hit vary significantly between the three inner sub-detectors, different weights have been used for different sub-detector hits. Since there are, on average, many more TRT hits per track than that of silicon hits, the silicon hits have larger weights. The average number of SCT hits per track is two times higher than that of pixel hits. Therefore, the pixel hit weight is twice the SCT hit weight.

The hit based matching technique is robust since it explicitly connects the reconstructed tracks and the generated particles at the digitization level. However, this cannot match the tracks which are decay products of primary particles. There are no

topological studies to recover this effect at this time.

Since the matching probability, P_{match}, is a discrete variable it is very difficult to understand the very low momentum tracks with a lower number of hits. Therefore, the hit matching technique alone was not used for this analysis. Figure 5.13(a) shows the distribution of hit ratio for 900 MeV data.

5.1.10.2 The Cone (Delta R) Based Technique

The cone based technique associates a truth particle with the closest reconstructed track. The radius of the cone is know as Delta R, ΔR, and the ΔR is defined as:

$$\Delta R = \sqrt{\Delta\phi^2 + \Delta\eta^2} \tag{5.5}$$

where

- $\Delta\phi$ is the difference between the truth track and the reconstructed track in ϕ.
- $\Delta\eta$ is the difference between the truth track and the reconstructed track in η.

A match is considered successful when a reconstructed track is found inside a defined ΔR cut. If more than one reconstructed tracks are found around the generated particle the closest track will be kept. There are also problems with the cone based method. There are some cases where the cone based technique can incorrectly match a track with a nearby truth particle. When this happens there typically won't be any common hit between track and truth particle and the transverse momentum will differ by a large amount. This is a clear fake match and this fake match can be neglected by choosing a very tight ΔR cut. In the previous analysis [1] the ΔR cut

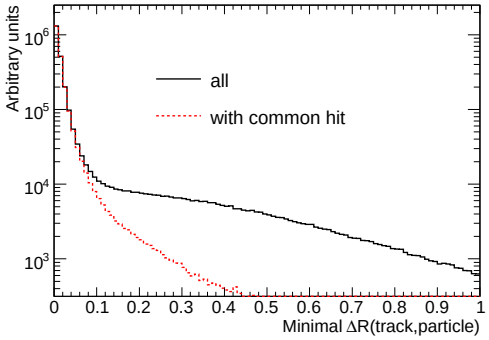

Figure 5.14: Minimal ΔR between a truth particle and a reconstructed track. In red, one common hit in the pixel detector is required.

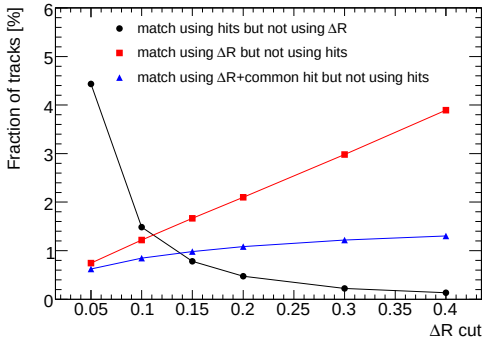

Figure 5.15: Fraction of tracks that have a truth match using one matching method and not another as a function of the ΔR cut used for the cone matching methods. The hit matching cut is fixed to P_{match} >0.55.

was 0.05 for $p_T > 500$ MeV. Therefore, the fake matching effect was neglected. In this analysis, for low-p_T tracks, $p_T > 100$ MeV and $p_T < 500$ MeV, the requirement of ΔR goes up to 0.15 (See Figure 5.14 [46]) since the track direction resolution dramatically degrades.

5.1.10.3 Combined Truth Matching Technique

As we have discussed in Section 5.1.10.2, the fake matches are a big problem for low-p_T tracks since we use a large cone size. Since the fake matches will not have common hits, the common hit requirement (matching probability) will reduce this fake effect. Figure 5.14 [46] shows that tail at large ΔR is removed after the common hit requirement. Figure 5.15 shows the fraction of the tracks with single matching technique and the combined matching technique. The fraction of the tracks, using only the cone based matching technique, increases with the ΔR cut due to fake matching. However, the additional common hit requirement cut controls the fake effect. A cut of 0.14 for

ΔR has been chosen for this analysis. Figure 5.15 clearly shows that the fractions of fake tracks with individual track matching techniques are small. But this fraction becomes completely negligible with the combined matching technique.

The combined matching technique associates a good description of the tracks and their corresponding charged particles. The hit matching technique removes the fake matches while the cone based method solves the problem of decays of primary particles. The combined matching technique is used for this analysis. Therefore, the inclusive efficiency of tracks of the primary particle is calculated by using Equation 5.3.

$$\epsilon_{\mathrm{trk}}(p_{\mathrm{T}},\eta) \;=\; \frac{N_{\mathrm{rec}}^{\mathrm{matched}}(p_{\mathrm{T}},\eta)}{N_{\mathrm{gen}}(p_{\mathrm{T}},\eta)}$$

and the non-primary rate (secondary rate) is given by:

$$f_{\mathrm{nonp}}(p_{\mathrm{T}},\eta) \;=\; \frac{N_{\mathrm{rec}}^{\mathrm{non-matched}}(p_{\mathrm{T}},\eta)}{N_{\mathrm{gen}}(p_{\mathrm{T}},\eta)} \tag{5.6}$$

where $N_{\mathrm{rec}}^{\mathrm{non-matched}}$ is the number of reconstructed tracks with no match to a primary truth particle.

In the case of non-primary particles, the non-primary particles are produced far away from the primary vertex and make the ΔR method complicated. Therefore, a simple hit matching of 0.55 is used to calculate the non-primary rate.

5.2 Summary

This chapter gives a clear explanation of minimum bias events. It also discusses the different types of Monte Carlo models with new tunings. The event selection for minimum bias measurements are discussed in detail.

Chapter 6

Charged Particle Multiplicities in pp Interactions at $\sqrt{s} = 0.9$ TeV and $\sqrt{s} = 7$ TeV Measured with the ATLAS Detector at the LHC

6.1 Introduction

Charged particle multiplicities have been measured in pp and $p\bar{p}$ collisions at different center-of-mass energies in previous experiments [38, 47–58]. Many of these measurements have been used to constrain phenomenological models of soft-hadronic interactions and to predict properties at higher center of mass energies.

In this chapter, the minimum bias measurements on primary charged particle

multiplicities are presented using the first $\sim$190 μb^{-1} of data recorded by the ATLAS experiment at 7 TeV and $\sim$7 μb^{-1} at 0.9 TeV.

In previous studies on minimum bias measurements at the same center-of-mass energies ($\sqrt{s}$ = 0.9 and 7 TeV), the measurements were taken by requiring a minimum reconstructed transverse momentum of $p_{\mathrm{T}} \geq 0.5GeV$[14,32]. Since most of the tracks have the transverse momentum of $p_{\mathrm{T}} \leq 0.5GeV$, it is very important to understand those low p_{T} tracks. In this analysis, the charged particle spectrum was measured requiring a minimum reconstructed transverse momentum of $p_{\mathrm{T}} \geq 0.1GeV$. In the previous measurements, high-p_{T} measurements, the tracks were reconstructed using the standard *Inside-Out* pattern recognition sequence of ATLAS; New Tracking (NEWT) [44].

The reconstruction algorithm setup has been updated to contain a staged chain of three *Inside-Out* tracking sequences to accommodate the lower momentum tracks. The enhanced tracking algorithm's threshold transverse momentum is lowered to p_{T} $\geq 0.1GeV$. The study implements a similar strategy as used at $\sqrt{s} = 0.9$ TeV for p_{T} $> 500MeV$ in analyzing the first collision data from the LHC.

The charged particle multiplicity measurements discussed here include

$$\frac{1}{N_{\mathrm{ev}}} \cdot \frac{\mathrm{d}N_{\mathrm{ch}}}{\mathrm{d}\eta}, \quad \frac{1}{N_{\mathrm{ev}}} \cdot \frac{1}{2\pi p_{\mathrm{T}}} \cdot \frac{\mathrm{d}^2 N_{\mathrm{ch}}}{\mathrm{d}\eta \mathrm{d}p_{\mathrm{T}}}, \quad \frac{1}{N_{\mathrm{ev}}} \cdot \frac{\mathrm{d}N_{\mathrm{ev}}}{\mathrm{d}n_{\mathrm{ch}}} \quad \text{and} \quad \langle p_{\mathrm{T}} \rangle \text{ vs. } n_{\mathrm{ch}},$$

where p_{T} is the transverse momentum of the charged particles with respect to the beam direction, and η is the pseudo-rapidity [1] , n_{ch} is the number of charged particles

[1] pseudo-rapidity is defined as $\eta = -\ln\tan(\theta/2)$. The polar angle θ is measured with respect to the z-axis. The

in an event, $N_{\rm ev}$ is the number of events with at least two charged particles in a selected phase space, $N_{\rm ch}$ is the total number of charged particles, and $\langle p_{\rm T} \rangle$ is the average $p_{\rm T}$ for a given number of charged particles [2]. In order to check the relative fractions of diffractive events (more diffractive contribution is expected at low number of charged particles and at the low track momentum), three different phase-space selections are considered by varying cuts on both $p_{\rm T}$ and the $N_{\rm ev}$ as explained in Section 5.1.5.1.

The charged particle multiplicity measurements are compared with Monte Carlo predictions. Even though the measurements are based on primary particles this analysis also includes non-primary particles, or secondary particles, which have to be corrected. A method of fitting Monte Carlo templates to data has been used to determined the fraction of secondary tracks in this analysis. The side band regions of the transverse (d0) and longitudinal (z0) impact parameters from data and MC are used for these fits. A detailed analysis of the fraction of non-primary particles is explained later in the chapter.

6.2 Analysis Procedure

This section discusses all the procedures, methods, and various contributions required to correct the charge multiplicity distributions.

The following factors are considered in correcting the multiplicity distributions.

- Trigger efficiency.

[2] The factor $2\pi p_{\rm T}$ in the $p_{\rm T}$ spectrum comes from the Lorentz invariant definition of the cross section in terms of d^3p. This can be expressed as $d\phi \cdot dy \cdot dp_{\rm T}$. Furthermore, we use the massless approximation: $dy \approx d\eta$.

- Vertex reconstruction efficiency.
- Tracking reconstruction efficiency.
- Non-primary tracks (secondaries and fakes).
- Unfolding of the p_{T} spectrum.

6.2.1 Trigger Efficiency

The trigger efficiency, ϵ_{trig}, for the single-arm MBTS trigger, is measured from the data sample using a control trigger. The events selected for the control trigger are from random filled bunch crossings (L1_RDO_FILLED), and are filtered at level 2 (L2). For the center-of-mass energy of $\sqrt{s} = 0.9$ TeV the level 2 (L2) filter requires at least seven SCT hits and seven pixel clusters, and the event filter (EF) requires at least one track with $p_{\mathrm{T}} > 200$ MeV. For the center-of-mass energy of $\sqrt{s} = 7$ TeV the L2 filter requires four pixel clusters and four SCT hits, and there were no EF requirements. Since the vertex efficiency is measured separately, the vertex requirements for the tracks were removed for trigger studies in order to minimize the correlation between trigger and vertex efficiencies. The trigger efficiency, ϵ_{trig}, is determined by dividing the number of events in the control sample which satisfied all L1_MBTS requirements with the total number of events in the control sample. Figure 6.1 [39] shows the trigger efficiency for both $\sqrt{s} = 0.9$ and 7 TeV.

6.2.2 Systematic Uncertainties for Trigger Efficiency

The trigger efficiency is measured without the vertex requirement so it is impossible to make the same impact-parameter cuts as in the final selection of tracks. Therefore, the trigger efficiency is measured using impact-parameter constraints with respect to the primary vertex (if available) or else the beam spot and compared to that obtained without this requirement. This variation provides a conservative estimation of the effect of beam induced background and non-primary tracks on the trigger efficiency at low values of $n_{\mathrm{sel}}^{\mathrm{BS}}$ [4]. The correlation of the MBTS trigger with the control trigger used to select the data sample for the trigger-efficiency determination is studied using simulations, and the effect on the trigger efficiency is found to be less than 0.1%. This is taken as a systematic uncertainty. The statistical uncertainty on the control sample is also taken as a systematic uncertainty. The total systematic uncertainty on the the trigger efficiency is of the order of 1% in the first $n_{\mathrm{sel}}^{\mathrm{BS}}$ bin, decreasing rapidly as $n_{\mathrm{sel}}^{\mathrm{BS}}$ increases.

6.2.3 Vertex Reconstruction Efficiency

The vertex reconstruction efficiency, ϵ_{vtx}, is calculated using data only, and is determined by taking the ratio of triggered events with a reconstructed vertex to the total number of triggered events. The method used to extract the vertex reconstruction efficiency is maintained with respect to the previous analysis [59]. The number of events that pass the event selection has been determined, where the primary tracks are defined with respect to the beam spot (BS). Then the fraction of the events with a

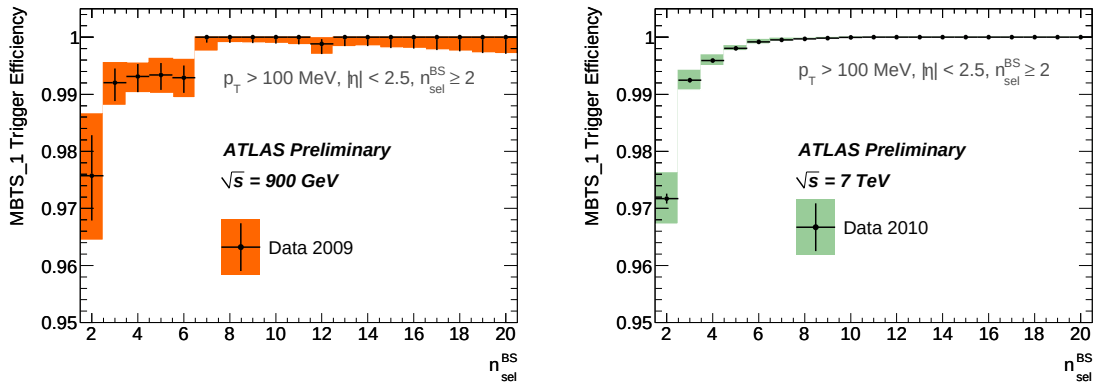

(a) (b)

Figure 6.1: Trigger efficiency as a function of $n_{\mathrm{sel}}^{\mathrm{BS}}$ at 0.9 (a) and 7 TeV (b). The colored error bands show the total uncertainty, the black vertical lines the statistical uncertainty of the events collected with the independent trigger.

reconstructed vertex is also measured. Background events are also excluded [4] before calculating the efficiency. The efficiency is measured as a function of $n_{\mathrm{sel}}^{\mathrm{BS}}$. In the first bin of $n_{\mathrm{sel}}^{\mathrm{BS}}$, the vertex efficiency is 90 - 92% depending on the center-of-mass energy and event selection. The ϵ_{vtx} goes up to 100% for higher $n_{\mathrm{sel}}^{\mathrm{BS}}$ bins.

The vertex reconstruction efficiency for events with two or more tracks, is shown in Figure 6.3 [42] for both $\sqrt{s} = 0.9$ and 7 TeV.

The dependence of the vertex efficiency on η, p_{T}, and the projection along the beam axis of the the separation between the perigees [3] of the tracks (Δz), for events with more than one track was studied. Only the dominant effect is corrected for all phase spaces. The rest of the corrections were found to be very small and without impact on the final result. A very strong effect is observed as a function of Δz for events with two tracks with the low momentum threshold. This bias can be corrected

[3] The perigee of a track is here the point of closest approach of the track and the coordinate origin (0,0,0).

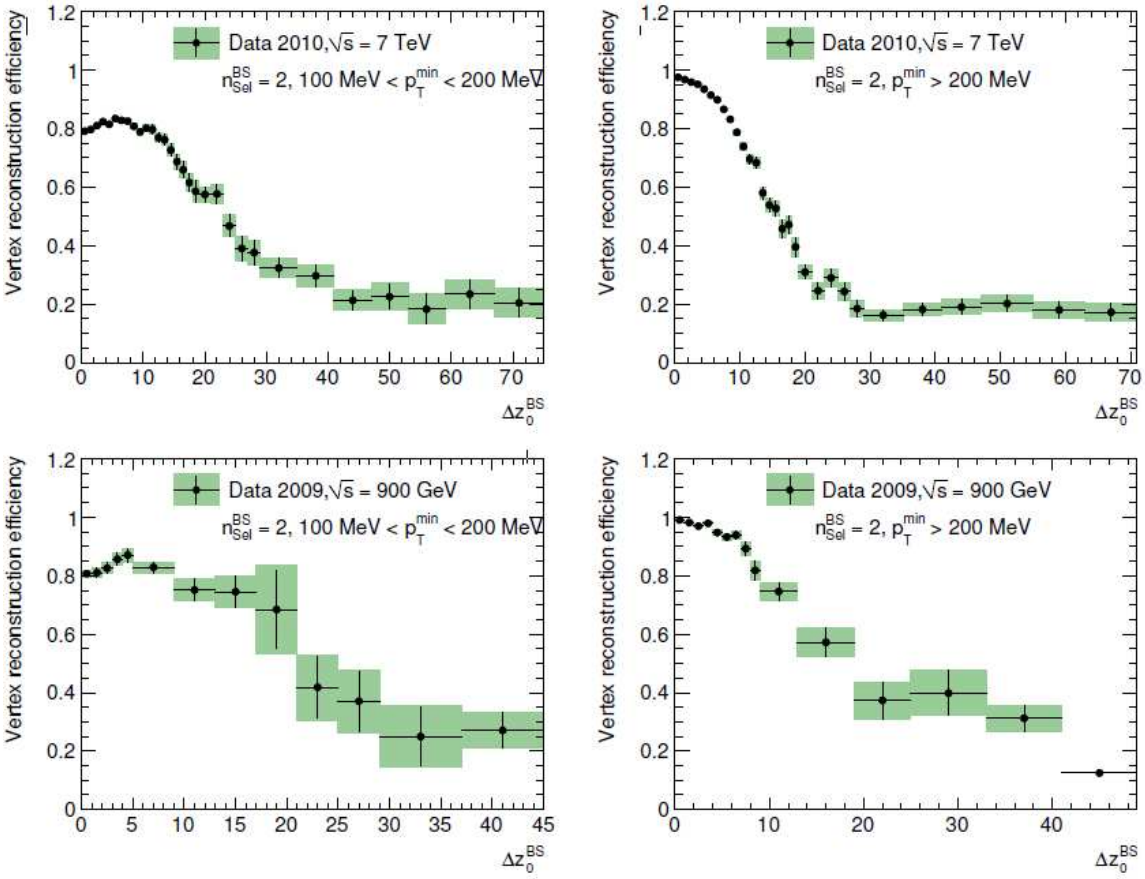

Figure 6.2: The primary vertex reconstruction bias as a function of Δz_0 for events with $n_{\rm sel}^{\rm BS}$= 2, in the ranges $p_T^{min} < 200$ MeV and $p_T^{min} > 200$ MeV for 7 TeV and 900 GeV samples. The bands represent the total systematic and statistical uncertainties.

using two different parameterizations of the momentum of lowest p_{T} tracks: one for the tracks below 200 MeV and another for the tracks above 200 MeV. Figure 6.2 shows the dependence on Δz in the lowest p_{T} region. The η dependence is negligible for this lower p_{T} track threshold selection. For the $p_{\mathrm{T}} \geq 500$ MeV selection, the η dependence is more than that of Δz.

6.2.4 Systematic Uncertainties for Vertex Reconstruction Efficiency

The systematic uncertainty on the Vertex Reconstruction Efficiency is taken to be equal to the beam background contribution.

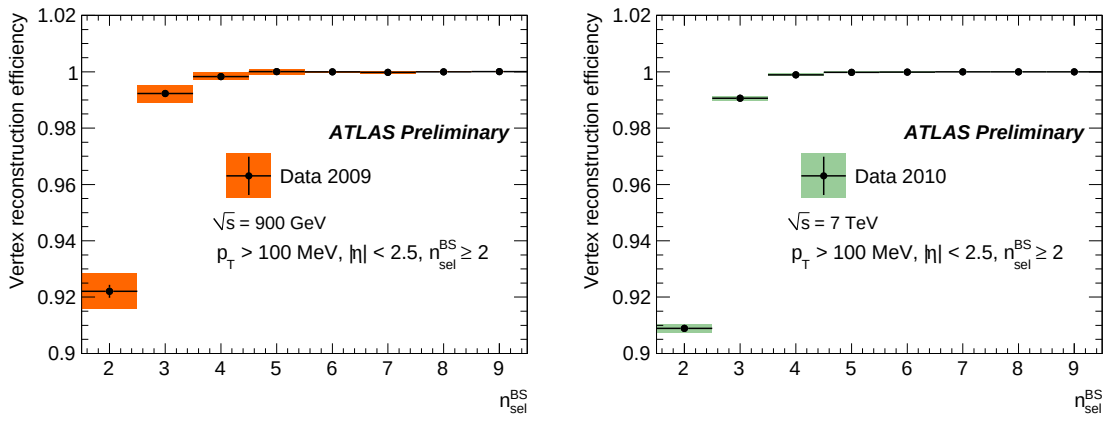

(a) (b)

Figure 6.3: Vertex reconstruction efficiency as a function of $n_{\mathrm{sel}}^{\mathrm{BS}}$ at 0.9 (a) and 7 TeV (b). The colored error bands show the total uncertainty, the black vertical lines the statistical uncertainty.

6.2.5 Track Reconstruction Efficiency

The reconstruction efficiency of the tracks was measured using MC samples and is binned in p_{T} and η. The reconstruction efficiency determination is explained in 5.1.9 . The agreement between data and MC of basic track quantities for tracks above 500 MeV and for $100 < p_{\mathrm{T}} < 500$ MeV is verified as shown in Figures 5.4 [2] and 5.5 [39].

The track reconstruction efficiency is defined as:

$$\epsilon_{\mathrm{trk}}(p_{\mathrm{T}}, \eta) \;=\; \frac{N_{\mathrm{rec}}^{\mathrm{matched}}(p_{\mathrm{T}}, \eta)}{N_{\mathrm{gen}}(p_{\mathrm{T}}, \eta)},$$

where p_{T} and η are generated particle transverse momentum and pseudo rapidity, $N_{\mathrm{rec}}^{\mathrm{matched}}(p_{\mathrm{T}}, \eta)$ is the number of reconstructed tracks matched to a generated charged particle, and $N_{\mathrm{gen}}(p_{\mathrm{T}}, \eta)$ is the number of generated charged particles in that bin [4].

Figure 6.4 [39] shows the final reconstruction efficiencies as functions of η and p_{T} at both $\sqrt{s} = 0.9$ and 7 TeV. An inefficiency is observed for $|\eta| > 1$ due to more material in that region. Since the analysis requires a minimum number of silicon hits, tracks that pass through the minimum number of layers, have a minimum p_{T}. Thus we observed an initial rise in reconstruction efficiency with p_{T}.

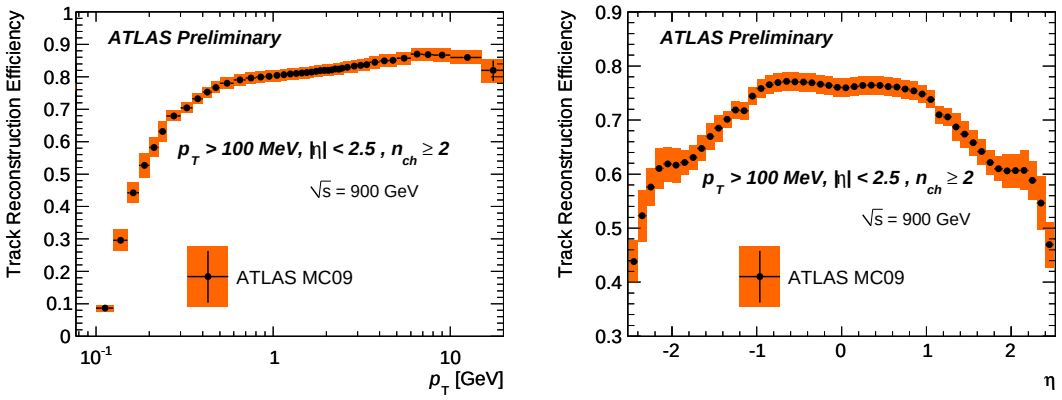

(a) (b)

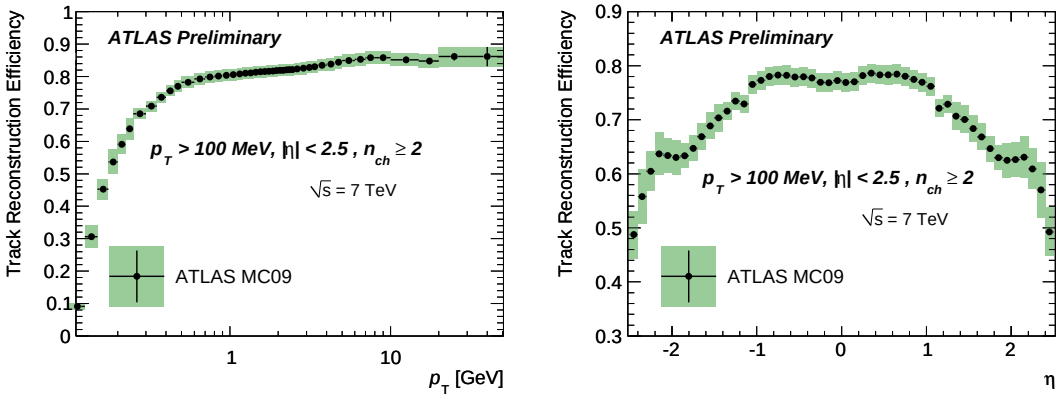

(c) (d)

Figure 6.4: Track reconstruction efficiency as a function of p_{T} (a,c) and η (b,d) for $\sqrt{s} = 0.9$ TeV (a,b) and 7 TeV (c,d). The total uncertainties on each point are shown as colored bands, the vertical error bars represent the statistical uncertainty of the Monte Carlo generator.

Systematic Uncertainty	Size	Region
Material	$\pm 2 - 15\%$	decreases with p_{T}, increases with $\lvert\eta\rvert$
χ^2 prob. cut	$\pm 10\%$	flat, only for $p_{\mathrm{T}} > 10$ GeV
Resolution	$\pm 5\%$ negligible -7%	$100 < p_{\mathrm{T}} < 150$ MeV $0.15 < p_{\mathrm{T}} < 10$ GeV $p_{\mathrm{T}} > 10$ GeV
Efficiency correction factor	$\pm 4\%$	only for $\sqrt{s} = 2.36$ TeV ID Track
Alignment and other high p_{T}	-3% to -30%	only for $p_{\mathrm{T}} > 10$ GeV averaged over η, increases with increasing p_{T}

Table 6.1: The systematic uncertainties on the track reconstruction efficiency for $\sqrt{s} = 0.9$ TeVand $\sqrt{s} = 7$ TeV . Unless otherwise stated, the systematic uncertainty is similar for all energies and phase-spaces. All uncertainties are quoted relative to the track reconstruction efficiency.

6.2.6 Systematic Uncertainties for Track Reconstruction Efficiency

There are several factors considered as systematic uncertainties on the track reconstruction efficiency such as the absorbing material uncertainty, the uncertainty due to the χ^2 probability cut, alignment uncertainty and other high-p_{T} effects, track selection uncertainty, and resolution uncertainty. The major contribution comes from material uncertainty effects. A summary of the total estimated systematic uncertainty is shown in Table 6.1.

6.2.6.1 Material Uncertainty Effect on Track Reconstruction Efficiency

Two different data driven methods were used to estimate the difference between the real detector and the material description in the simulation;

- reconstruction of the invariant mass of K_s^0 which decays to two charged pions.

- comparing the track lengths in data and the simulation.

The K_s^0 invariant mass method studies the variation of mass as a function of decay radius of the meson. It has great sensitivity for small radii. The second method probes the material description in the simulation in terms of nuclear interaction length (λ), starting after the Pixel detector [4]. In the K_s^0 invariant mass method, the invariant mass is measured as a function of η, ϕ, and decay radius.

The data is compared with distributions obtained by three types of simulations: the nominal simulation and simulations in which the total material weight in the Inner Detector had been increased by 5% or 10%.

Figure 6.8 [39] shows the invariant mass of K_s^0 as a function of η . It clearly shows that the material description in the nominal simulation sample gives the observed K_s^0 invariant mass in the barrel region where $|\eta| \lesssim 1.3$.

In the track length method, the tracks are reconstructed using the pixel detector only. These Pixel-only tracks are matched with good tracks with the full selection cuts. The fraction of matched tracks with only pixel detector is defined as the SCT extension rate. The SCT extension rate is compared between both data and two types of MC simulation samples; the nominal sample and the 10% extra-material sample. In addition to the 10% ID material sample another sample where only the external pixel services are scaled by 20% is also compared in some particular η regions. This study verified that the nominal MC simulation sample has good agreement with data in the barrel region while a small deviation was observed for the lowest p_{T} slice (100-200 MeV) (see Figure 6.5 [39]).

The data has very good agreement with the nominal sample and not with the 10% enhanced material sample for $|\eta| < 2.0$. There is a deviation in the end-cap region ($|\eta| > 2.0$) which is not covered by the 10% enhanced extra material sample for all p_{T} bins. This complicated region contains the service structures (cooling pipes, cables, etc.) of the pixel detector. The pixel service structures cause the MC material description to be inaccurate. Both the 20% enhanced pixel service material and 10% enhanced ID material samples have similar and strong effects in this forward region.

Two slightly different approaches have been use to determine the final material uncertainty using the track length method. The first one is to combine the uncertainties of 10% extra material sample with that of nominal sample using the SCT extension rate. The second one is to combine the uncertainties of 10% extra material sample with 20% enhanced pixel service material sample using the SCT extension rate. Both methods give relatively similar uncertainties for most p_{T} and η bins. In the barrel region,the total uncertainty from material effects varies from 8% at low p_{T} down to 2% above 500 MeV. The uncertainty increases with $|\eta|$. In the region of $2.3 < |\eta| < 2.5$ the largest uncertainties are observed with 15% in the first p_{T} bin decreasing to 7% above 500 MeV.

6.2.6.2 Uncertainty due to the χ^2 Probability Cut on Track Reconstruction Efficiency

In Section 5.1.7, the track-fit (χ^2) probability, as shown in Figure 5.6(b), has been used as a powerful tool to discriminate against badly measured tracks. In reality, the distribution of this variable is not well modeled in MC. The fraction of these mis-

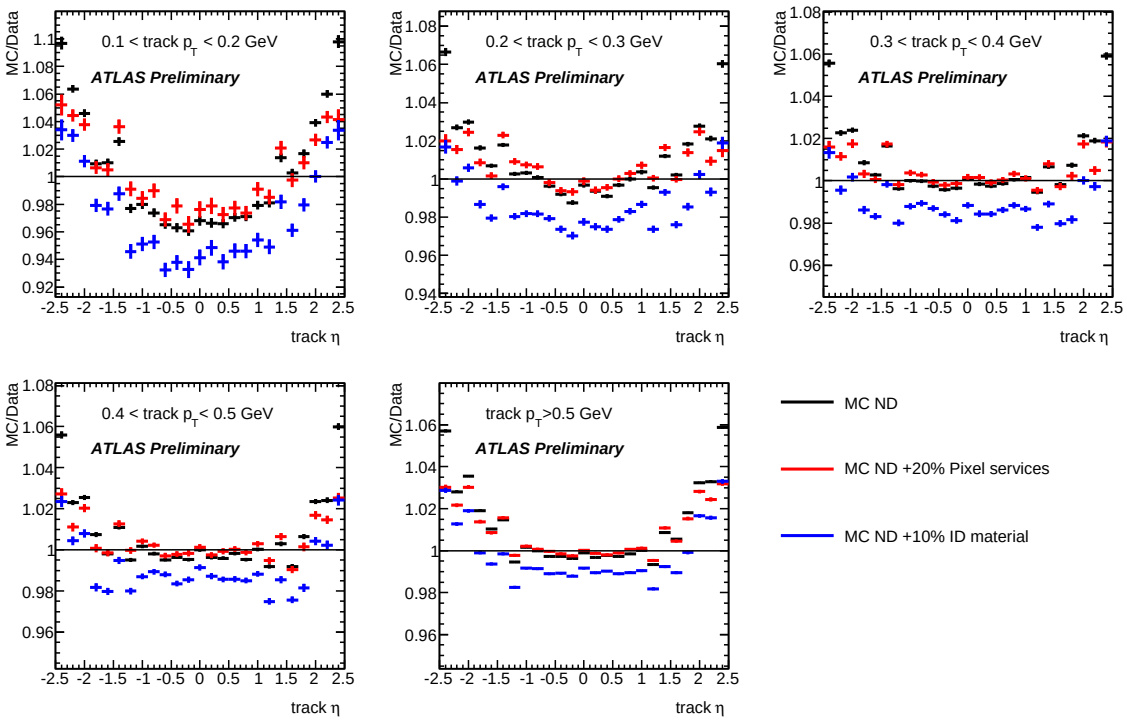

Figure 6.5: Ratio of the MC over data of the SCT extension rate in slices of p_{T} and as a function of η, for the nominal MC (black) as well as the sample with 10% extra material in the ID (blue) and the sample with 20% more material in the external Pixel services (red). The horizontal black line at unity is to guide the eye.

measured tracks, which are observed predominantly at the edges of the η acceptance where the distance between consecutive measurement points of the outer layer of the pixel and the first layer of the SCT can reach to $\sim$ 1 m, is observed to be more significant in data than the Monte Carlo generator even after this cut is applied. Figure 6.6 shows, for one particular $|\eta|$ region, the χ^2 probability distribution in data compared to MC. There is a difference in χ^2 probability distributions between data and MC. This difference is caused by differences either in the number of degrees-of-freedom or in the χ^2 distributions. But the studies found that the number of degrees of freedom has a relatively good agreement at the end-cap while there is a very clear shift in the barrel. In particular, the χ^2 is smaller in MC than in data for the barrel.

In order to have a better agreement with the data and MC, a error scaling factor is obtained to increase the χ^2 values of the tracks in the MC. Figure 6.6 shows a good improvement in the χ^2 distributions after the scaling factor is applied (red line). The fraction of tracks in data and in MC as a function of the reconstructed track p_{T} are shown in Figure 6.7 after the χ^2 probability cut of 0.01. Since this cut is applied only for $p_{\mathrm{T}} > 10\ GeV$, the fraction is always 1 for $p_{\mathrm{T}} < 10\ GeV$. The maximum difference between data and MC is found to be 10%, which is taken as a conservative estimate of the systematic uncertainty due to this cut. The uncertainty is taken to be flat in p_{T}. All systematic uncertainties on the mis-measured high-p_{T} tracks are taken as single-sided errors [4].

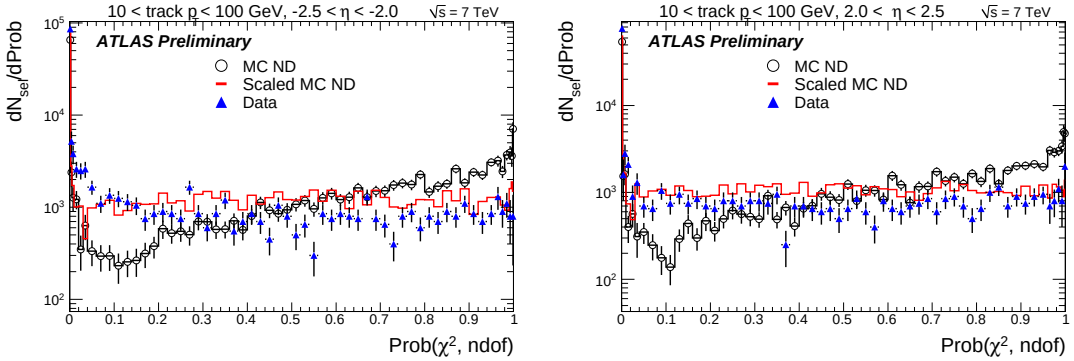

Figure 6.6: Comparison of track-fit probability for $-2.5 < \eta < -2.0$ (left) and $2.0 < \eta < 2.5$ (right) . All plots are for a reconstructed track p_{T} above 10 GeV. The blue filled triangles show the data, while the black histogram indicates the MC (normalized to the number of data entries). The red histogram shows the MC with a scale factor of 1.3 applied to the χ^2.

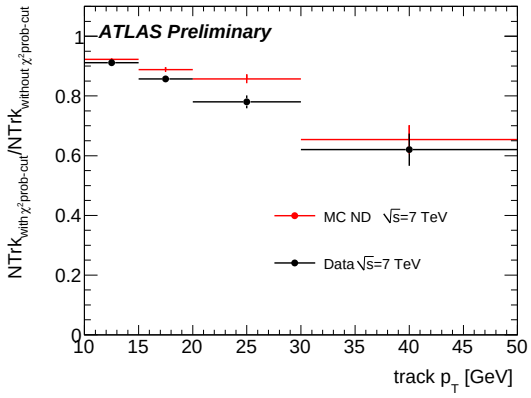

Figure 6.7: Fraction of tracks in data (black) and in MC (red) that pass the χ^2 probability cut of 0.01 as a function of the reconstructed track p_{T}. The cut is only applied for tracks with $p_{\mathrm{T}} > 10$ GeV.

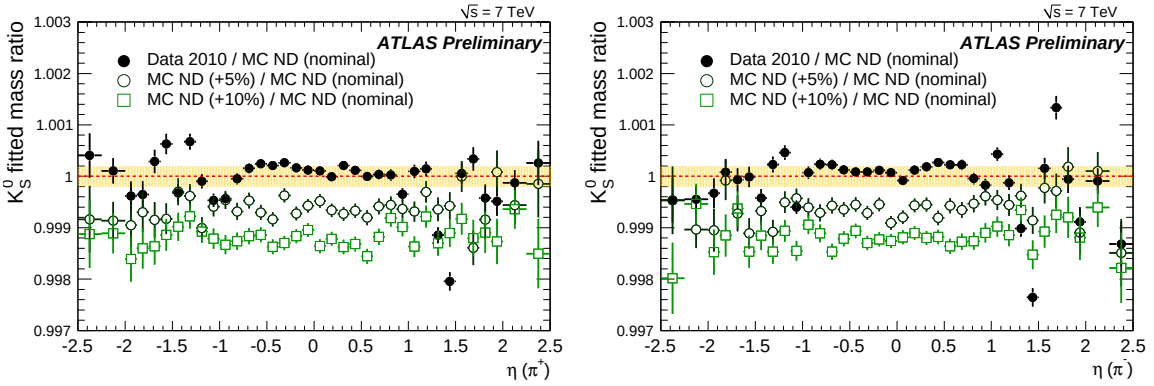

(a) (b)

Figure 6.8: Fitted K^0_s mass ratios as a function of η for data and various MC simulated material descriptions over to the nominal MC sample. The η values are obtained from the positive (a) and negative (b) track. The K^0_s candidates considered for these plots are required to have a reconstructed decay radius smaller than 25 mm, i.e. before the beam pipe. Furthermore, the two pion tracks of all K^0_s candidates are required to have at least four silicon hits. The vertical error bars show the statistical uncertainty only (data and MC), while the horizontal orange bands indicate the uncertainty due to the magnetic field strength.

6.2.6.3 Track Resolution Uncertainty

The p_T cuts are applied at various stages of the pattern recognition inside the track reconstruction algorithm. These different p_T cuts cause an inefficiency due to the momentum resolution. The different momentum resolution or a significant bias in the momentum estimation in data and MC can change the migration of the tracks in the first bin ($100 < p_T < 150$ MeV). This can cause a loss or gain in the observed number of tracks. In order to estimate the effect of momentum resolution in tracking efficiency, the track resolution was increased by a very conservative value of 10 MeV at the seed finding stage in MC. This adjustment made the p_T resolution effectively 15 MeV instead of 10 MeV at the seed finding stage. The effect of this shift on the track reconstruction efficiency in the first p_T bin was found to be about 5%. This

difference is assigned as a systematic uncertainty.

6.2.6.4 Track Selection Uncertainty

The track selection uncertainty is determined by the detailed comparison of the properties of the data and MC simulation by varying the track selection criteria. A difference between data and MC is observed in the high η region and is found to be $\sim 1\%$. As a conservative estimate a constant 1% uncertainty is assigned for the whole region.

6.2.7 Unfolding p_{T} distribution of the generated tracks

The p_{T} unfolding method, is explained in B.3, corrects the bin migration in p_{T} of a poorly reconstructed tracks. The unfolding method is used after applying all other corrections. The effect on the p_{T} spectrum in data due to this unfolding procedure is at most 10% at $\sqrt{s} = 0.9$ TeV and 3% at $\sqrt{s} = 7$ TeV.

6.2.8 Closure Test

The closure test exercise is used to demonstrate the performance of the corrections and Bayesian unfolding. This exercise was used in the previous analyses [1, 2]. In this test, the particles from the nominal Monte Carlo sample were reconstructed and corrected back to the particle level using the same methods as applied to data. The corrected charged particle distributions are then compared to the initial known distributions from PYTHIA. There was 1.5% of difference found between the generated and the corrected distributions in the second bin (n_{ch}= 3) of the n_{ch} distribution. All

other bins remain the same when we compared generated particles with corrected distributions. The agreement of the charged-particle multiplicity spectrum as a function of pseudorapidity and the average p_{T} vs n_{ch} is at the level of 1% in all bins.

6.2.9 Non-Primary Particles Estimation

Two types of particles are considered to be non-primary particles: fakes and secondaries.

6.2.9.1 Method

A method was used in previous analyses [1,2,42] to obtain the fraction of non-primary tracks in data. A fit to the tails of the d_0 distribution is applied in this analysis to all non-primary tracks. In the previous analysis [1, 2, 42], to estimate the fraction of non-primaries in the data the primary ($f_p(d_0)$) and the non-primary($f_{np}(d_0)$) templates were derived from Monte Carlo using the impact parameter, d_0, distribution. These templates are used to fit the distribution in the data leaving the normalization constant B (scaling factor) for the non-primaries free. The following equation has been used in previous analysis where the threshold p_{T} is 500 MeV: $f(d_0) = A \times (f_p(d_0) + B/A \times (f_{np}(d_0))$ where A is the fraction of all particles, and B is the fraction of non-primary particles. As default the fraction of all particles A in the Monte Carlo is normalized to the data for a non-primary scaling factor of 1. Since the previous analysis [1, 2, 42] is based $p_{\mathrm{T}} \geq 500$ MeV, the contribution from photon conversions to electron and positron is small. But in this analysis, the threshold p_{T} started from 100 MeV. The contribution from photon conversions is no longer negligi-

ble as shown in Figures 6.9 and 6.10. In this analysis, we fit separately for primaries, non-primaries from conversions and non-conversions. Figures 6.9 and 6.10 show that primaries are populated inside the Gaussian peak of d_0. The electrons/positrons from conversions have primarily large values of d_0 while other non-primaries (labeled non-electrons) are more likely to be inside the Gaussian peak.

A fit is performed in the side-bands region of the d_0 distribution, i.e. outside the range in $|d_0|$ used for selecting tracks. The fraction of primary, electron non-primary and non-electron non-primary tracks are all allowed to float with the total number of events constrained to that of the data [4].

The main reason to introduce the layer-0 (B-layer) hit requirement in track selection, as explained in Section 5.1.7, is to remove the large fraction of the tails of this distribution. This allows the fit of all three parameters to be performed on the data. Since the primary and non-primary $|d_0|$ region changes from very low p_{T} to 500 MeV, the low p_{T} region is divided into eight bins of 50 MeV for $100 < p_{\mathrm{T}} < 500$ MeV in the fit. There was an additional single fit for $p_{\mathrm{T}} > 500$ MeV. For this bin, there is no separate fit for electrons and non-electrons since the electron contribution is extremely low in both the central and the tail regions.

The effect of the electron contribution is cross checked with z_0 (longitudinal impact parameter) as shown in Figure 6.11 where there is no distinction between electrons and other non-primaries. The non-primary rate difference between the d_0 and z_0 fit is taken as a systematic uncertainty. The scaling factors of non-electrons in the d_0 fit differ with respect to electrons by 11% in the first bin, by 10% in the last bin and less than 3% in all other bins.

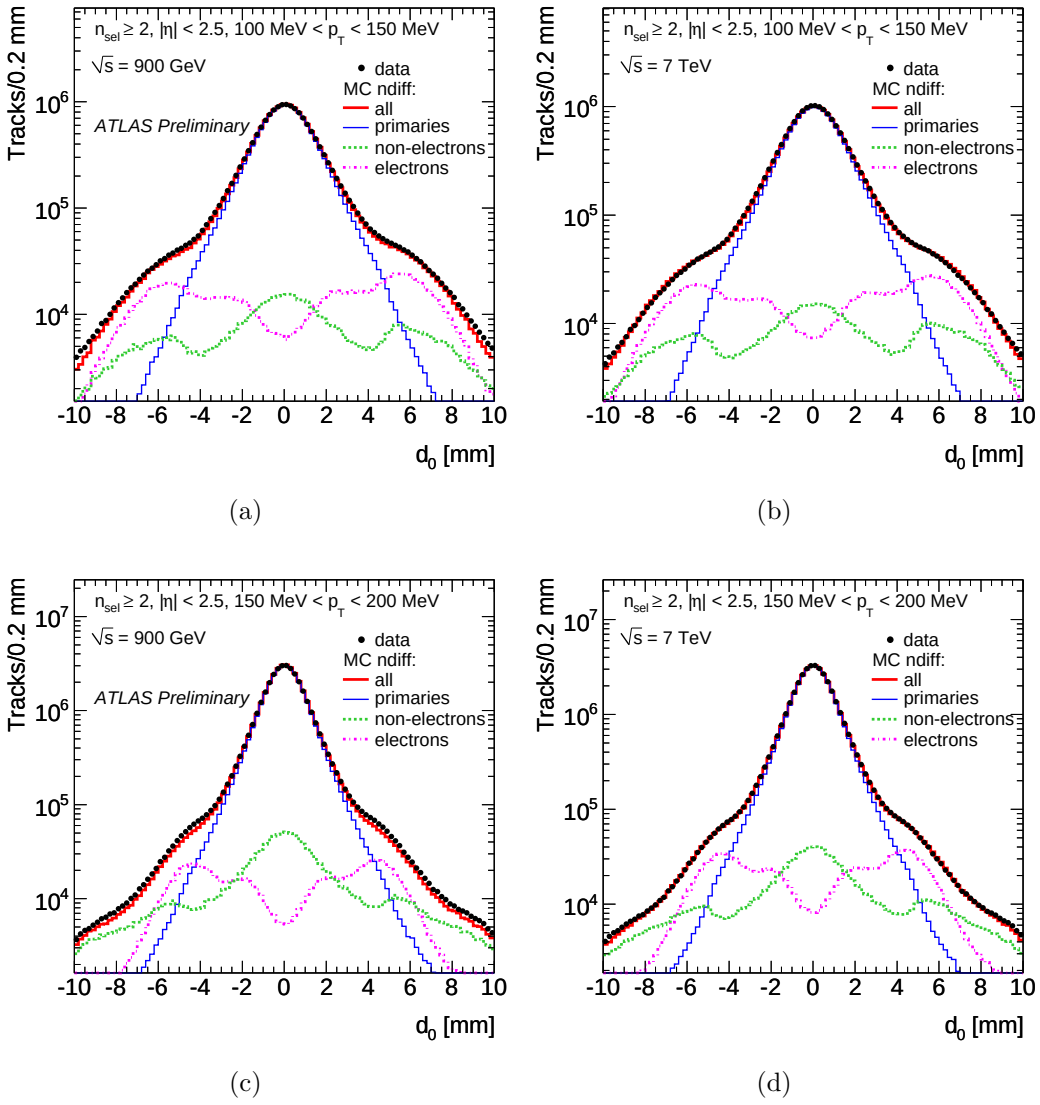

Figure 6.9: d_0 distribution for primary (blue) and non-primary particles after scaling them to the best fit value for $p_{\mathrm{T}} = 100 - 150$ MeV (a) and $p_{\mathrm{T}} = 150 - 200$ MeV (b) at $\sqrt{s} = 7$ TeV (c) and $p_{\mathrm{T}} = 100 - 150$ MeV (b) and $p_{\mathrm{T}} = 150 - 200$ MeV (d) at $\sqrt{s} = 0.9$ TeV. The non-primary particles are split into electrons (pink) coming mostly from photon conversions and non-electrons (green) which are the dominant contribution after the analysis cuts are applied.

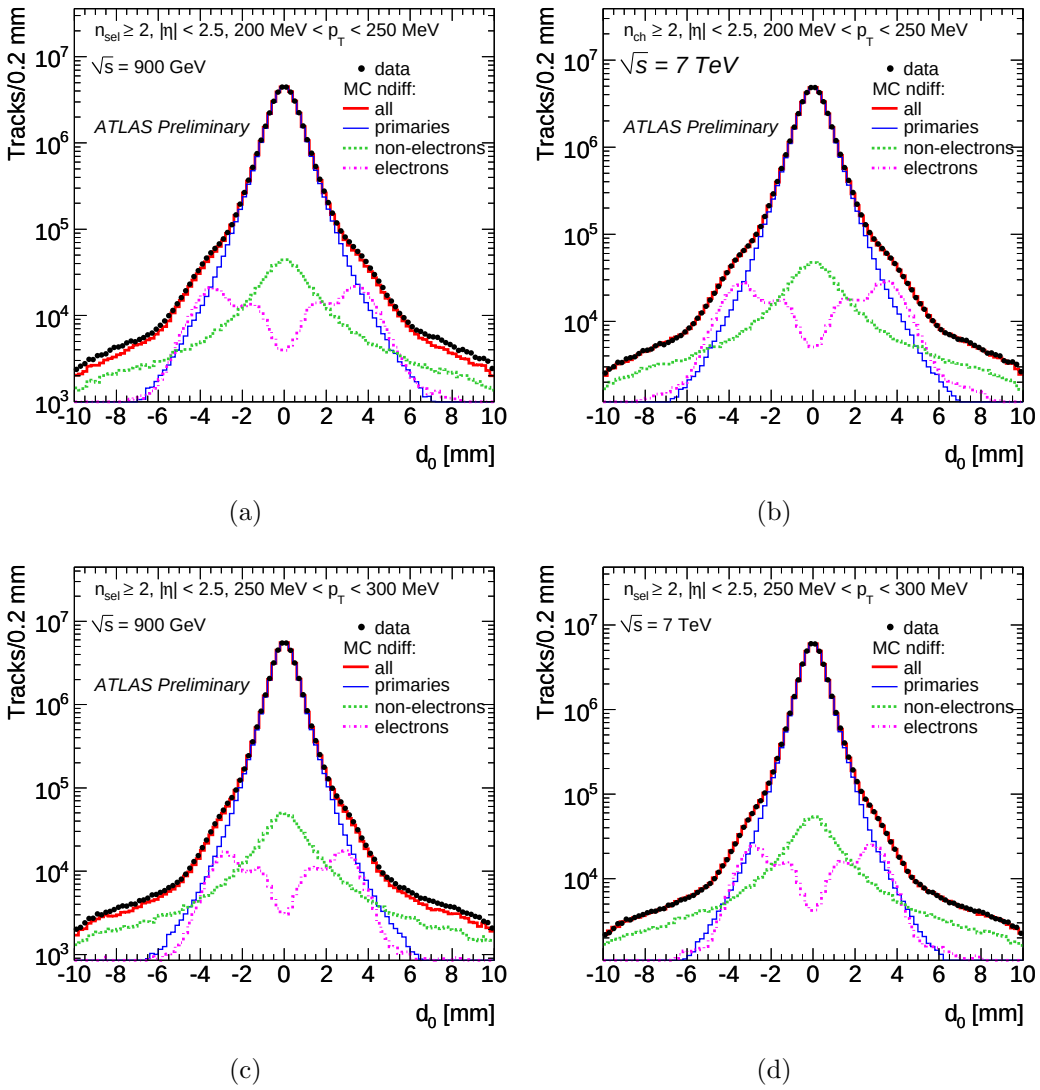

Figure 6.10: d_0 distribution for primary (blue) and non-primary particles after scaling them to the best fit value for $p_{\mathrm{T}} = 200 - 250$ MeV (a) and $p_{\mathrm{T}} = 250 - 300$ MeV (b) at $\sqrt{s} = 7$ TeV (c) and $p_{\mathrm{T}} = 200 - 250$ MeV (b) and $p_{\mathrm{T}} = 250 - 300$ MeV (d) at $\sqrt{s} = 0.9$ TeV. The non-primary particles are split into electrons (pink) coming mostly from photon conversions and non-electrons (green) which are the dominant contribution after the analysis cuts are applied.

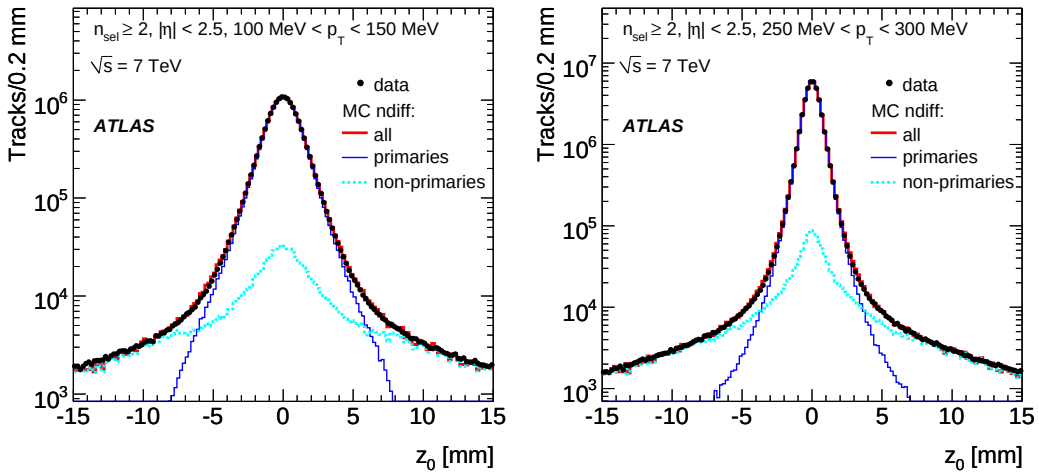

(a) (b)

Figure 6.11: z_0 distribution for primary (blue) and non-primary particles (Megenda) after scaling them to the best fit value for $p_{\mathrm{T}} = 100 - 150$ MeV (a) and $p_{\mathrm{T}} = 250 - 300$ MeV (b) at $\sqrt{s} = 7$ TeV.

Table 6.2: Non-primary rate using d_0 fit

P_T Range (MeV)	SF (electron)	SF (others)	Rate	Fraction (electron)	Fraction (others)	Fraction (total)
100 -150	0.79	0.90	0.0288	0.0146	0.0192	0.0338
150 -200	0.74	0.98	0.0218	0.0082	0.0161	0.0243
200 -250	0.70	0.97	0.0181	0.0059	0.0144	0.0203
250 -300	0.70	1.03	0.0178	0.0054	0.0136	0.0190
300 -350	0.68	1.06	0.0171	0.0048	0.0131	0.0179
350 -400	0.67	1.09	0.0170	0.0044	0.0129	0.0173
400 -450	0.61	1.17	0.0175	0.0043	0.0127	0.0170
450 -500	0.60	1.18	0.0175	0.0043	0.0126	0.0169
> 500	1.26		0.0205			0.0163

Table 6.3: Non-primary rate using z_0 fit

P_T Range (MeV)	SF secondaries	Rate
100 -150	1.01	0.0340
150 -200	1.0	0.0242
200 -250	1.01	0.0205
250 -300	1.05	0.0201
300 -350	1.08	0.0193
350 -400	1.13	0.0196
400 -450	1.14	0.0194
450 -500	1.21	0.0205
> 500	1.36	0.0221

6.2.9.2 Systemic Uncertainties

The non-primary fraction difference between MC and data is taken as a systematic uncertainty. There is a 25% difference of non-primaries in data compared to MC for $p_{\mathrm{T}} > 500$ MeV. This conservative estimate is taken to be constant as a function of p_{T} and results in only a small effect, up to 0.9%, on the final corrected distributions.

The resulting difference between the d_0 fit and z_0 fit is used to estimate the effect of the choice of variables in the fit. The difference is measured to be 12% in the first bin, 8% in the last bin and less than 4% in all other bins; this difference is taken as a source of systematic uncertainty.

The fraction of non-primary tracks for $|d_0| < 1.5$ mm is found to be stable with respect to a change in the fit range of 1 mm in all p_{T} bins except the first one ($100 < p_{\mathrm{T}} < 150$ MeV), where a 10% difference is observed; this difference is taken as a systematic uncertainty. The fraction of non-primary tracks is found to be independent of n_{sel}, but shows a small dependence on η, which is taken as a small systematic

uncertainty of 0.1%.

The total uncertainty on the fraction of non-primary tracks is the sum of all the above uncertainties. The total absolute uncertainty at $\sqrt{s} = 0.9$ TeV and $\sqrt{s} = 7$ TeV is 0.01 for the first p_{T} bin, decreasing to 0.005 above 500 MeV.

Tables 6.2 and 6.3 show the scaling factor, non-primary rate, and the non-primary fraction for both d_0 and z_0 respectively.

6.2.10 Correction Procedure

The distribution of charged particle multiplicities as explained in Section 6.1 are shown in Figures 6.12 and 6.13 [60]. These distributions are plotted after applying all selection cuts but before the corrections. The corrections are applied on these distributions using the correction procedure.

Each component of the distributions is weighted by predicted cross section by PYTHIA, and the sum of each distribution were normalized to the number of tracks in data. These figures also show the ratio between data and MC simulation. Since the multiplicity (n_{tr}) and the bin size of these distributions were determined from the statistical uncertainty on each bin in the uncorrected distributions, the bin widths are smaller at low n_{tr} and p_{T} but the widths increase at high n_{tr} and p_{T}.

The bin widths are varied for different center-of-mass energies due to the statistics of data. However, the multiplicity as a function of the pseudorapidity has a constant bin width throughout the region.

The goal of the minimum bias analysis to obtain the charged particle multiplicity distributions as a function of the number of reconstructed tracks. In order to get

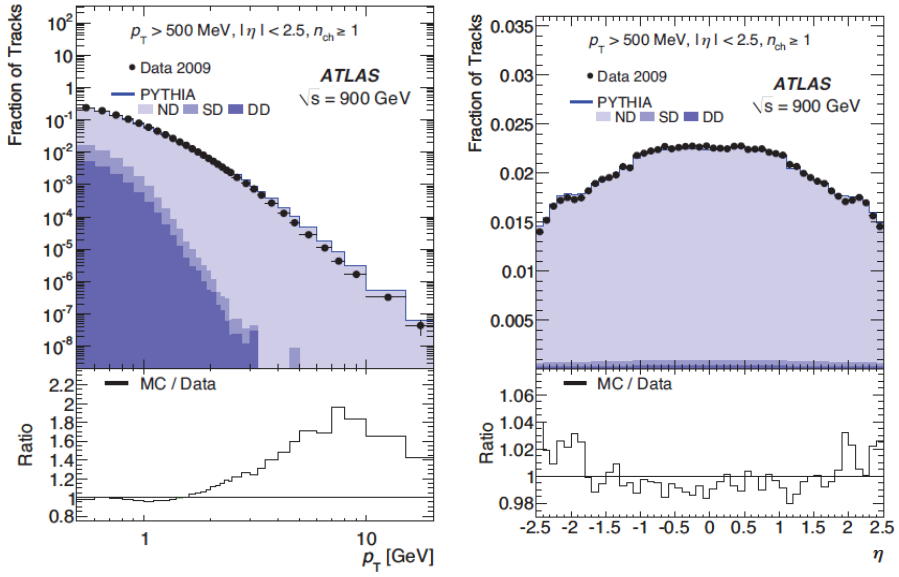

(a) (b)

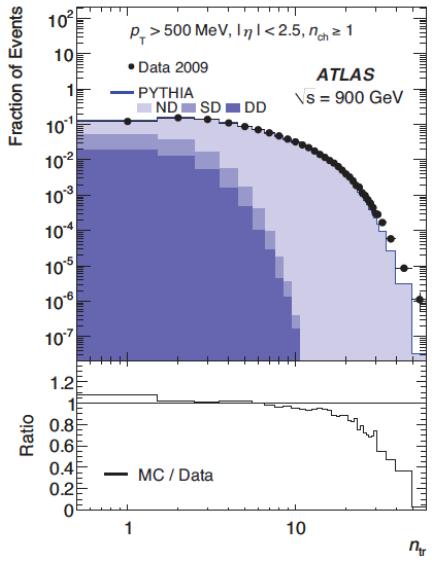

(c)

Figure 6.12: The fraction of the distribution of reconstructed tracks from both data and PYTHIA with MC09 tune at center-of-mass energy of 900 MeV as a function of pseudorapidity (a), transverse momentum (b) and charged particle multiplicity (n_{tr}).

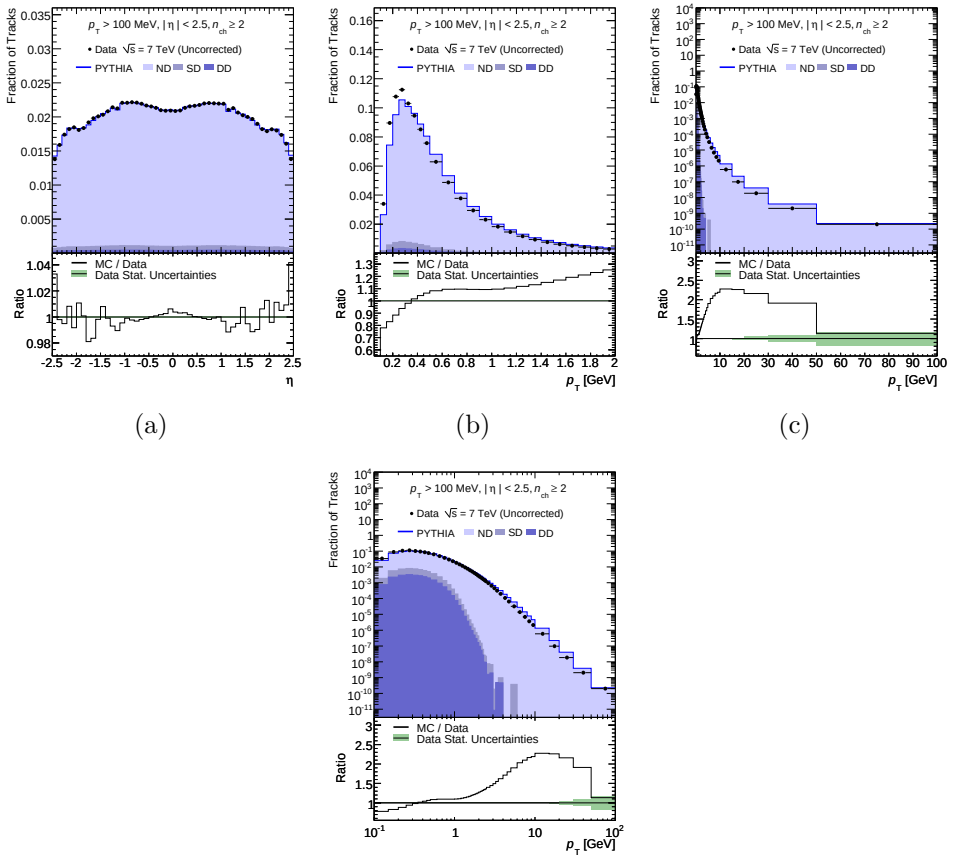

(a) (b) (c)

(d)

Figure 6.13: Uncorrected distributions of reconstructed track multiplicities for $\sqrt{s} =$ 7 TeV events with $n_{\rm sel} \geq 2$ within the kinematic range $p_{\rm T} > 100$ MeV and $|\eta| < 2.5$. The panels show the selected-track multiplicity as a function of pseudorapidity (a) and of the transverse momentum in linear (b), linear-log (c) and log-log (d) scales. The dots represent the data and the shaded areas are the sum of the PYTHIA-MC09 inelastic components produced from reconstructing tracks from the Geant4 simulation. The vertical bars represent the statistical uncertainties.

these distributions, corrections must be applied to events and the tracks in the form of weighs. The events are corrected by applying a weight to the each event for the event selection efficiency, and the tracks are corrected by applying the weight to each track for the reconstructed tracking efficiency. The effect of the trigger and the vertex requirement on event selection could have caused the event to be lost. This can be corrected by applying an event weight:

$$w_{\mathrm{ev}}(n_{\mathrm{sel}}^{\mathrm{BS}}) = \frac{1}{\epsilon_{\mathrm{trig}}(n_{\mathrm{sel}}^{\mathrm{BS}})} \cdot \frac{1}{\epsilon_{\mathrm{vtx}}(n_{\mathrm{sel}}^{\mathrm{BS}}, x)} \tag{6.1}$$

where

- $\epsilon_{\mathrm{trig}}(n_{\mathrm{sel}}^{\mathrm{BS}})$ and $\epsilon_{\mathrm{vtx}}(n_{\mathrm{sel}}^{\mathrm{BS}}, x)$ are the trigger and the vertex efficiencies respectively.
- x is either the Δz between tracks or the η of the tracks, as described in Section 6.2.3.

The corrections to p_{T} and η of the selected tracks are obtained by applying a weight to each track:

$$w_{\mathrm{trk}}(p_{\mathrm{T}}, \eta) = \frac{1}{\epsilon_{\mathrm{trk}}(p_{\mathrm{T}}, \eta)} \cdot (1 - f_{\mathrm{nonp}}(p_{\mathrm{T}})) \cdot (1 - f_{\mathrm{okr}}(p_{\mathrm{T}}, \eta)) \tag{6.2}$$

where

- $\epsilon_{\mathrm{trk}}(p_{\mathrm{T}}, \eta)$ is the tracking efficiency as described in Section 5.1.9.
- f_{nonp} is the fraction of non-primary tracks determined as described in section 6.2.9.

- f_{okr} is the fraction of selected tracks produced by primary particles outside the kinematic range.

The f_{okr} is produced from resolution effects and has been estimated using the Monte Carlo model. There were no corrections applied to η. The closure test was carried out for all distributions in all phase-space regions considered.

6.2.10.1 n_{ch} Unfolding

The number of selected tracks, n_{sel}, is corrected for trigger and vertex efficiencies. Then, the Bayesian unfolding technique [61] is used to correct the observed track multiplicities, n_{sel}, to the number of charged particles in the event: An Unfolding two dimensional matrix, $M_{\mathrm{ch,sel}}$, is defined that the probability for a given multiplicity of selected track n_{sel} is due to a number of charged particles n_{ch}. The Matrix is populated using Monte Carlo, MC09 tune, and applied to obtain the n_{ch} distribution from the data. The resulting n_{ch} distribution was then used to repopulate the matrix and the correction was applied on the number of selected tracks n_{sel}. This procedure was repeated without a regularization until it converged [4].

After the unfolding procedure was finished on n_{sel}, the resulting charged particle multiplicity distribution is corrected for the migrated events which are coming from out of the kinematic range (eg: $n_{\mathrm{ch}} \geq 2$). The unfolding matrix cannot be used for

[4] Convergence is defined as the first iteration in which the χ^2 difference between the result of the unfolding and the input distribution for that iteration is less than the number of bins used in the unfolding.

these events. An additional correction factor:

$$1/(1-(1-\epsilon_{\rm trk})^{n_{\rm ch}}-n_{\rm ch}\cdot\epsilon_{\rm trk}\cdot(1-\epsilon_{\rm trk})^{(n_{\rm ch}-1)}) \tag{6.3}$$

is used to correct these events for all phase-space selections. Here $\epsilon_{\rm trk}$ is the mean effective track reconstruction efficiency for a particular $n_{\rm ch}$ bin.

6.2.10.2 Systematic Uncertainties for $n_{\rm ch}$ Unfolding

Two main sources of systematic uncertainties are considered here:

- those due to track reconstruction efficiency uncertainties,
- and different $p_{\rm T}$ spectra in data and simulation.

The first uncertainty was estimated by starting from the $n_{\rm sel}$ spectrum in the data; the tracks are randomly removed for each value of $n_{\rm sel}$ according to the mean $p_{\rm T}$ and η and the reconstruction efficiency uncertainty for $p_{\rm T}$ and η values. Once the new input distribution is obtained by removing the tracks, the unfolding method was applied to this distribution and the difference with respect to nominal $n_{\rm ch}$ distribution is considered as a systematic uncertainty. This source gives the uncertainty of $\sim 3\%$ to $\sim 25\%$ at $\sqrt{s} = 7$ TeV in the most inclusive phase-space, $n_{\rm ch} \geq 2$, $p_{\rm T} > 100$ MeV, $|\eta| < 2.5$.

In the second case, as the unfolding is carried out in a single dimension on $n_{\rm ch}$, there is some dependency on $p_{\rm T}$ spectrum of simulation. This dependency is due to the strong dependence of the track reconstruction efficiency on $p_{\rm T}$. The difference between the average track reconstruction efficiency in data and MC is treated in the

same way as the uncertainty on track reconstruction efficiency and the same procedure was followed as described in the previous paragraph. This gives an asymmetric uncertainty. The uncertainty varies between -2% and $+55\%$ at $\sqrt{s} = 7$ TeV for the most inclusive phase-space selection.

6.2.10.3 Corrections to N_{ev}

The total number of events, N_{ev}, is calculated by integrating the corrected n_{ch}distributions. This is used to normalize the final distribution.

6.2.10.4 Systematic Uncertainties for N_{ev}

The systematic uncertainty of the N_{ev} distribution is estimated using the same method as that used for the n_{ch}distribution. Events entering or leaving the phase-space introduce a systematic uncertainty on N_{ev}. The total uncertainty on N_{ev} at $\sqrt{s} = 7$ TeV for the most inclusive phase-space is 0.3%, mostly due to the track reconstruction efficiency.

6.2.10.5 Corrections to p_{T}

The tracks are first corrected for the trigger and vertex inefficiencies at the event level. For the track level, they were corrected for the track reconstruction inefficiencies, contamination due to non-primary tracks and out of range kinematic factors. Then an unfolding method (see the Appendix B.3 for the p_{T} unfolding), similar to that used on n_{ch}, is applied to correct the p_{T} of the selected track to obtain the primary particle momentum.

6.2.10.6 Systematic Uncertainties for p_{T}

In the high-p_{T} region, the systematic uncertainties associated with mis-aligned tracks are estimated by scaling the number of mis-measured tracks in MC to match those found in data. The new input p_{T} distribution obtained using the above scaling is put through the unfolding procedure. The difference between final p_{T} distribution and nominal MC p_{T} distribution is taken as a systematic uncertainty. The systematic associated with the p_{T} resolution is obtained by smearing good tracks as explained in Section 6.2.6.3. The effect on the final unfolded distribution is taken as a systematic [4]. Since both high-p_{T} systematic uncertainties are single-sided, they were added linearly. The systematic uncertainty, in the high-p_{T} region, is measured to be -10% at p_{T} of 10 GeV to -30% in the last bin in p_{T} ($30 < p_{\mathrm{T}} < 50$ GeV) at $\sqrt{s} = 7$ TeV for the $n_{\mathrm{ch}} \geq 2$, $p_{\mathrm{T}} > 100$ MeV phase-space.

"In order to assess the stability of the results under varying starting hypotheses for the MC spectrum used to fill the matrix, a flat initial prior is used as an input. While convergence is only typically reached after seven iterations, instead of three for the nominal prior, the final difference in the unfolded spectra is small; this difference with respect to the MC p_{T} spectrum used as prior is taken as a systematic uncertainty. At $\sqrt{s} = 7$ TeV this uncertainty is less than 2% for all but a couple of bins around bin size changes where the effect is 3-5%. At $\sqrt{s} = 0.9$ TeV, due to more limited statistics in the MC, the largest change seen is 7% with a few others around 3-4%" [4].

6.2.11 Correction to the Mean p_{T} versus n_{ch}

In the case of the $\langle p_{\mathrm{T}} \rangle$ vs. n_{ch} distribution, the correction is applied on two separate components: $\sum_i p_{\mathrm{T}}(i)$ vs. n_{ch} and $\sum_i 1$ vs. n_{ch}, where $\sum_i p_{\mathrm{T}}(i)$ is the total p_{T} of all tracks in a particular bin of n_{ch} and $\sum_i 1$ is the total number of tracks in that bin. Then the ratio of $\sum_i p_{\mathrm{T}}(i)$ and $\sum_i 1$ is taken, after all corrections are applied, to obtain the $\langle p_{\mathrm{T}} \rangle$. The corrections of $\sum_i p_{\mathrm{T}}(i)$ and $\sum_i 1$ distributions are also done by two steps.

First, both $\sum_i p_{\mathrm{T}}(i)$ and $\sum_i 1$ distributions as a function number of selected tracks, n_{sel}, are corrected at event level and track level by applying weights. Then the n_{ch} unfolding procedure, is explained in section 6.2.10.1, is applied to each of the distributions. Finally, the ratio of these two distribution is taken.

6.2.11.1 Extrapolation to $p_{\mathrm{T}} = 0$

The correction to extrapolate the average multiplicity in the spectrum with lowest measured p_{T} to the inclusive p_{T} multiplicity is not applied in calculating the main results. However, a model-dependent correction is applied in order to compare the ATLAS results with other experiments. Three different correction methods are used to obtain the corrections:

- fitting the p_{T} spectrum to a given functional template.
- assumption of a flat distribution of $\frac{1}{p_{\mathrm{T}}} \cdot \frac{\mathrm{d}N_{\mathrm{ch}}}{\mathrm{d}p_{\mathrm{T}}}$ in the low p_{T} region.
- obtaining the correction factor from the AMBT1 PYTHIA6 MC.

The corrected p_{T} spectrum of the track is fitted with the Tsallis [62] distribution which has two components.

$$f(p_{\mathrm{T}}) = \frac{1}{2\pi\eta'} \sum_{i=\pi,p} \frac{dN_{\mathrm{ch}}}{dy}\bigg|_{y=0,i} \cdot \frac{(n_i-1)(n_i-2)}{(n_i T_i + m_{0,i}(n_i-1))(n_i T_i + m_{0,i})} \cdot \left[\frac{n_i T_i + m_T(p_{\mathrm{T}})_i}{n_i T_i + m_{0,i}}\right]^{-n_i} \cdot \tanh^{-1}\left(\frac{p_{\mathrm{T}}\sinh\eta'}{\sqrt{m_{0,i}^2 + p_{\mathrm{T}}^2\cosh^2\eta'}}\right)\bigg|_{\eta'=2.5},$$

"where $m_T(p_{\mathrm{T}})$ is the transverse mass $m_T = \sqrt{p_{\mathrm{T}}^2 + m_0^2}$ and m_0 is the particle rest mass $m_0 = \{m_\pi, m_p\}$ and $dN_{\mathrm{ch}}/dy|_{y=0,i}$, T_i and n_i are the six parameters of the fit. $dN_{\mathrm{ch}}/dy|_{y=0}$ represents the integrated yield of the particle production at mid-rapidity, but is left here as a free parameter of the fit. Mesons (pions and kaons) are merged into a single Tsallis function since there is insufficient information in the measured distribution to fit three independent shapes. The $\tanh^{-1}$ term is derived to account for the fact that the measurement is done as a function of pseudorapidity, as the individual E/p measurement for each track is unavailable and thus we consider averaged terms integrated over the whole η range." [4]

The fit to this function, from $p_{\mathrm{T}} > 100$ MeV to $p_{\mathrm{T}} > 0$ MeV, gives the correction factors of 1.068 at $\sqrt{s} = 0.9$ TeV and 1.065 at $\sqrt{s} = 7$ TeV. The second method gives a correction factor of 1.055 at $\sqrt{s} = 0.9$ TeV and 1.051 at $\sqrt{s} = 7$ TeV. The third method gives a correction factor of 1.055 at $\sqrt{s} = 0.9$ TeV and 1.051 at $\sqrt{s} = 7$ TeV.

The correction factor obtained from the functional fit is used in this analysis.

6.2.11.2 Systematic Uncertainties for the Average Multiplicity at $p_{\mathrm{T}} = 0$

Several systematic uncertainties sources on the scale factor are considered to estimate the uncertainty. The final scale factors, with total uncertainty, are then $1.063 \pm 0.014_{\mathrm{tot}}$ at $\sqrt{s} = 7$ TeV and $1.065 \pm 0.011_{\mathrm{tot}}$ at $\sqrt{s} = 0.9$ TeV.

6.3 Total Systematic Uncertainties

The systematic uncertainty of each variable has been individually discussed in previous sections. The total uncertainty is obtained by the sum in quadrature from the different sources, unless explicitly mentioned in the text. The major contribution comes from the track reconstruction efficiency.

6.4 Summary

A detailed explanation of minimum bias analysis procedure is discussed in this chapter. This procedure includes trigger efficiency, tracking efficiency, event efficiency, and non-primary estimation. Each of these components are discussed in detail.

Systematic uncertainty on the number of events, N_{ev}		
	$\sqrt{s} = 0.9$ TeV	$\sqrt{s} = 7$ TeV
Trigger efficiency	0.2%	0.2%
Vertex reconstruction efficiency	$< 0.1\%$	$< 0.1\%$
Track reconstruction efficiency	1.0%	0.7%
Different Monte Carlo tunes	0.4%	0.4%
Total uncertainty on N_{ev}	1.1%	0.8%
Systematic uncertainty on $(1/N_{\mathrm{ev}})\cdot(dN_{\mathrm{ch}}/d\eta)$ at $\eta = 0$		
Track reconstruction efficiency	3.1%	3.1%
Trigger and vertex efficiency	$< 0.1\%$	$< 0.1\%$
Non-primary track fraction	0.4%	0.4%
Total uncertainty on N_{ev}	-1.1%	-0.8%
Total uncertainty on $(1/N_{\mathrm{ev}}) \cdot (dN_{\mathrm{ch}}/d\eta)$ at $\eta = 0$	2.1%	2.3%

Table 6.4: Summary of systematic uncertainties on the number of events, N_{ev}, and on the charged-particle density $(1/N_{\mathrm{ev}})\cdot(\mathrm{d}N_{\mathrm{ch}}/\mathrm{d}\eta)$ at $\eta = 0$ for $n_{\mathrm{ch}} \geq 2$, $p_{\mathrm{T}} > 100$ MeV, $|\eta| < 2.5$ for $\sqrt{s} = 0.9$ TeV and $\sqrt{s} = 7$ TeV. All sources of uncertainty are assumed to be uncorrelated.

Chapter 7

Results and Conclusions

7.1 Results

The charged particle multiplicity distributions of primary particles for three difference phase-spaces of:

- at least one charged particle in the kinematic range $|\eta| < 2.5$ and $p_{\mathrm{T}} > 500$ MeV,
- at least two charged particles in the kinematic range $|\eta| < 2.5$ and $p_{\mathrm{T}} > 100$ MeV, and
- at least six charged particles in the kinematic range $|\eta| < 2.5$ and $p_{\mathrm{T}} > 500$ MeV

are shown in Figures from 7.1 to 7.9. At each center-of-mass energy, the results are compared to predictions of Monte Carlo models tuned to a wide range of measurements as discussed in Section 5.1.4. The data are presented as inclusive-inelastic distributions, where no corrections were made to remove the single diffractive com-

ponent, within a particular phase-space with minimal model-dependent corrections to facilitate the comparison with models.

7.1.1 Charged Particle Multiplicities as a Function of Pseudorapidity

The charged particle multiplicities as a function of pseudorapidity for center-of-mass energies of $\sqrt{s} = 0.9$ and 7 TeV are shown in Figures 7.1 and 7.2 [4]. Figure 7.1 shows the distribution for the first phase-space selection, $n_{\rm ch} \geq 1, p_{\rm T} > 500$ MeV, $|\eta| < 2.5$, for both center-of-mass energies of $\sqrt{s} = 0.9$ TeV and $\sqrt{s} = 7$ TeV. The mean pseudorapidity density distribution is relatively stable in the central region, $|\eta| < 1.0$, while it decreases for higher pseudorapidity. There are variations between the different MC models such as the DW PYTHIA 6 tuning strategy which has a flatter behavior and a pronounced dip at zero pseudorapidity particularly for $\sqrt{s} = 0.9$ TeV. Overall, the shape and normalization are fairly well described by the AMBT1 PYTHIA6 tune for both $\sqrt{s} = 0.9$ TeV and $\sqrt{s} = 7$ TeV.

Figures 7.2(a) and 7.2(b) show the pseudorapidity density function for second and most inclusive phase-space selection, $n_{\rm ch} \geq 2, p_{\rm T} > 100$ MeV, $|\eta| < 2.5$. In this case, the shape and normalization variations among the MC models are somewhat less compared to the first space-space as described above. The distributions are somewhat flatter due to the lower $p_{\rm T}$ threshold consistent with the effects of the diffractive component versus η. However, there is a difference among the MC models at $\sqrt{s} = 0.9$ TeV where the PHOJET model has very good agreement with data. All

models describe the shape of the data distribution relatively well. However, at 7 TeV, the normalization between models varies more widely even though the shapes match relatively well.

Finally, Figures 7.2(c) and 7.2(d) represent the density distributions for the third phase-space, $n_{\mathrm{ch}} \geq 6$, $p_{\mathrm{T}} > 500$ MeV, $|\eta| < 2.5$, which has a smaller diffractive contribution. All models have relatively good agreement with data at 900 GeV. However, at 7 TeV, DW PYTHIA6 and PHOJET show some difference versus data for both shape and normalization.

7.1.2 Charged Particle Multiplicities as a Function of the Transverse Momentum

The charged particle multiplicities as a function of transverse momentum for both $\sqrt{s} = 0.9$ TeV and $\sqrt{s} = 7$ TeV are shown in Figures 7.3 and 7.4. Figure 7.3 shows the charged particle multiplicity distribution for the first phase-space of $n_{\mathrm{ch}} \geq 1$, $p_{\mathrm{T}} > 500$ MeV, $|\eta| < 2.5$. No model agrees with data over the whole region specially for $p_T > 1$ GeV. In this region, $p_T > 1$ GeV, the PYTHIA6 DW model shows relatively better agreement to the data than the other models (i.e. the model with Q^2 ordered parton showering).

The distributions for the second phase-space of $n_{\mathrm{ch}} \geq 2$, $p_{\mathrm{T}} > 100$ MeV, $|\eta| < 2.5$ are shown in Figures 7.4(a) and 7.2(b) for $\sqrt{s} = 0.9$ TeV and $\sqrt{s} = 7$ TeV respectively. At 900 GeV, among the all models the PHOJET model describes the

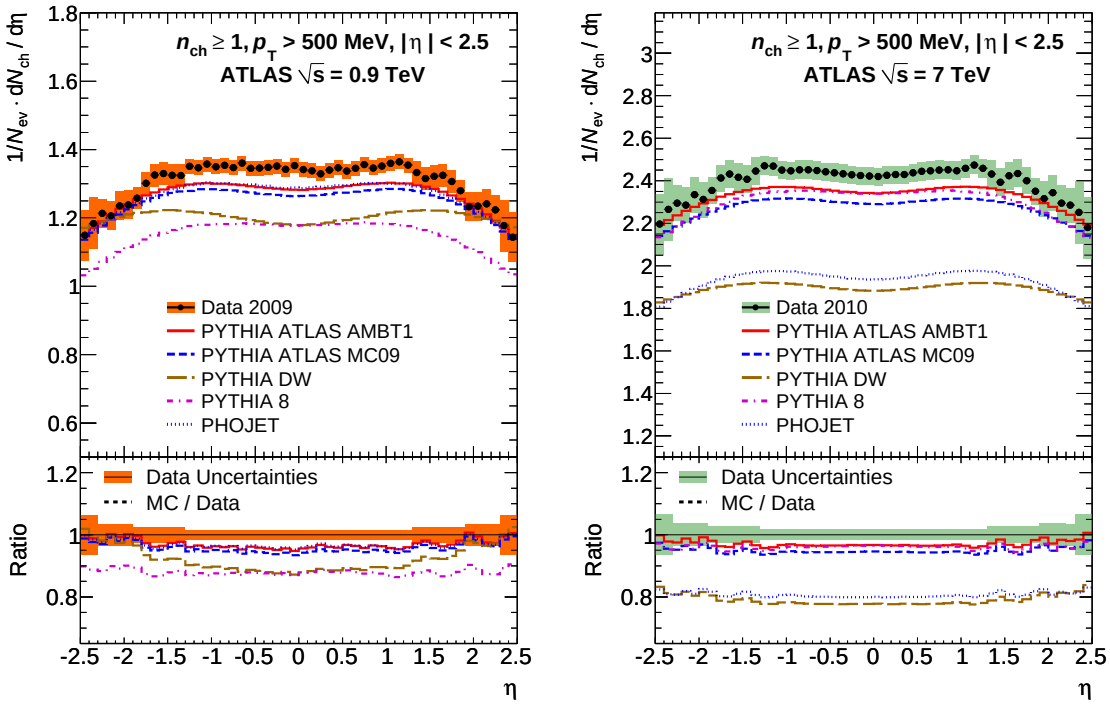

(a) (b)

Figure 7.1: Charged particle multiplicities as a function of pseudorapidity for events with $n_{\mathrm{ch}} \geq 1$, $p_{\mathrm{T}} > 500$ MeV and $|\eta| < 2.5$ at $\sqrt{s} = 0.9$ TeV (a) and $\sqrt{s} = 7$ TeV (b). The dots represent the data and the curves represent the predictions from different MC models. The vertical bars represent the statistical uncertainties, while the shaded areas show statistical and systematic uncertainties added in quadrature. The bottom inserts show the ratio of the MC over the data. The values of the ratio histograms refer to the bin centroids.

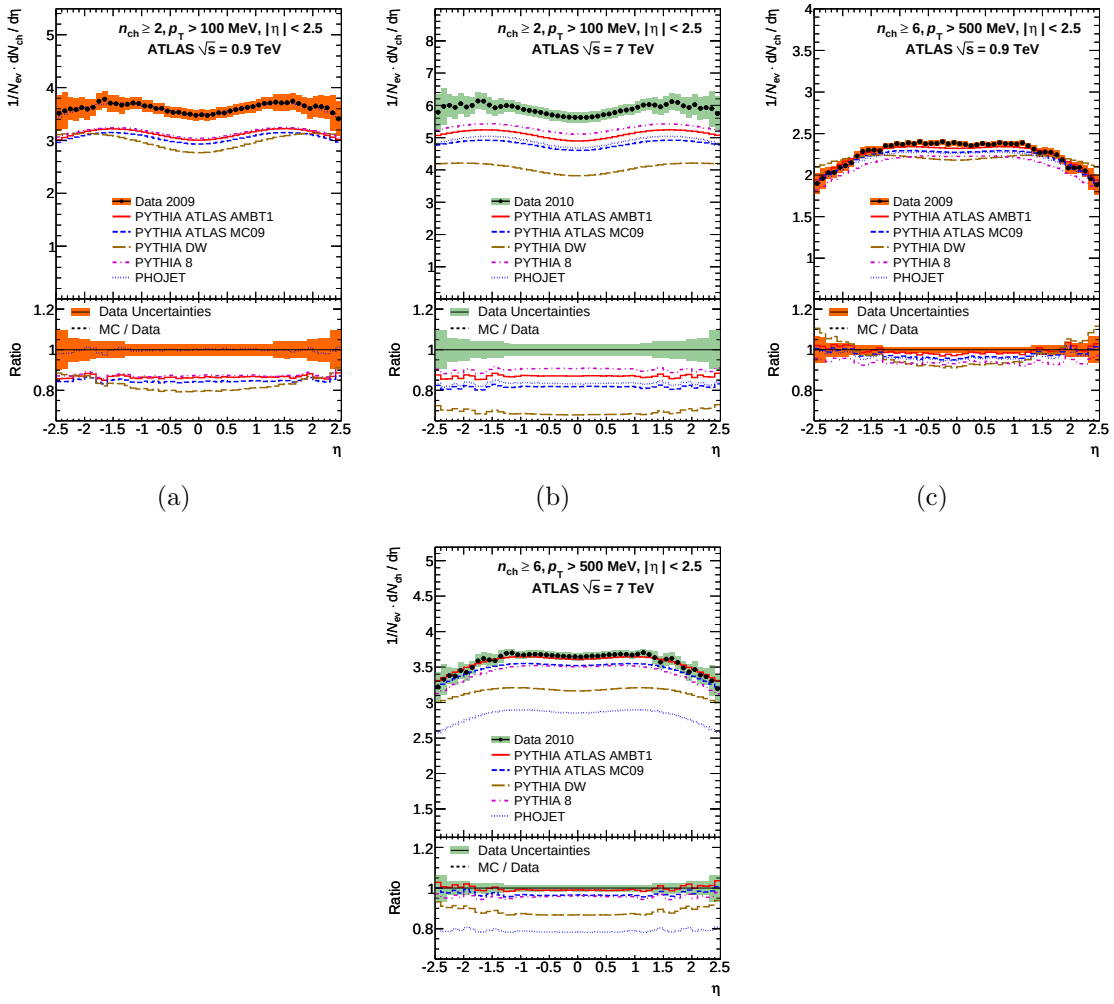

Figure 7.2: Charged particle multiplicities as a function of pseudorapidity for events with $n_{\mathrm{ch}} \geq 2$ $p_{\mathrm{T}} > 100$ MeV (a,b) and $n_{\mathrm{ch}} \geq 6$ (c,d), $p_{\mathrm{T}} > 500$ MeV and $|\eta| < 2.5$ at $\sqrt{s} = 0.9$ TeV (a,c) and $\sqrt{s} = 7$ TeV (b,d). The dots represent the data and the curves represent the predictions from different MC models. The vertical bars represent the statistical uncertainties, while the shaded areas show statistical and systematic uncertainties added in quadrature. The bottom inserts show the ratio of the MC over the data.

data better over the whole range of p_{T} spectrum but still shows some slight disagreement with the data. All other models at this energy underestimate the number of low p_{T} particles while they widely vary in predictions at high p_{T}. At 7 TeV, the low p_{T} effect is more pronounced while PYTHIA8 and PHOJET have good agreement with data at high p_{T}. The AMBT1, MC09 and DW tunes of PYTHIA6 overestimate the number particles in the high p_{T} region.

Figures 7.4(c) and 7.2(d) [4] show the distributions for the last and the most exclusive phase-space of $n_{\mathrm{ch}} \geq 6$, $p_{\mathrm{T}} > 500$ MeV, $|\eta| < 2.5$. For these distributions, the new AMBT1 tune shows improvement compared to the older MC09 tune. However, this tune does not agree with data for the entire p_{T} range.

7.1.3 Charged Particle Multiplicity Distribution

The charged particle multiplicity distributions as a function of number of charged particles for the first phase-space, $n_{\mathrm{ch}} \geq 1$, $p_{\mathrm{T}} > 500$ MeV and $|\eta| < 2.5$, are shown in Figure 7.5 for both center-of-mass energies [4]. Some of the models predict higher numbers of the events for a low number of charged particles. "It should be noted that due to the normalization, $1/N_{\mathrm{ev}}$, a deviation observed in one region needs to be compensated for by one in the other direction somewhere else" [4]. The AMBT1 tuning of PYTHIA6 has a relatively better agreement with data than other models. Figures 7.6(a) and 7.6(b) show the charged particle distributions for the most inclusive phase-space. The shape and the normalization widely vary for all MC models throughout the region for both $\sqrt{s} = 0.9$ TeV and $\sqrt{s} = 7$ TeV. There is no a single model which can explain this distribution for this phase-space.

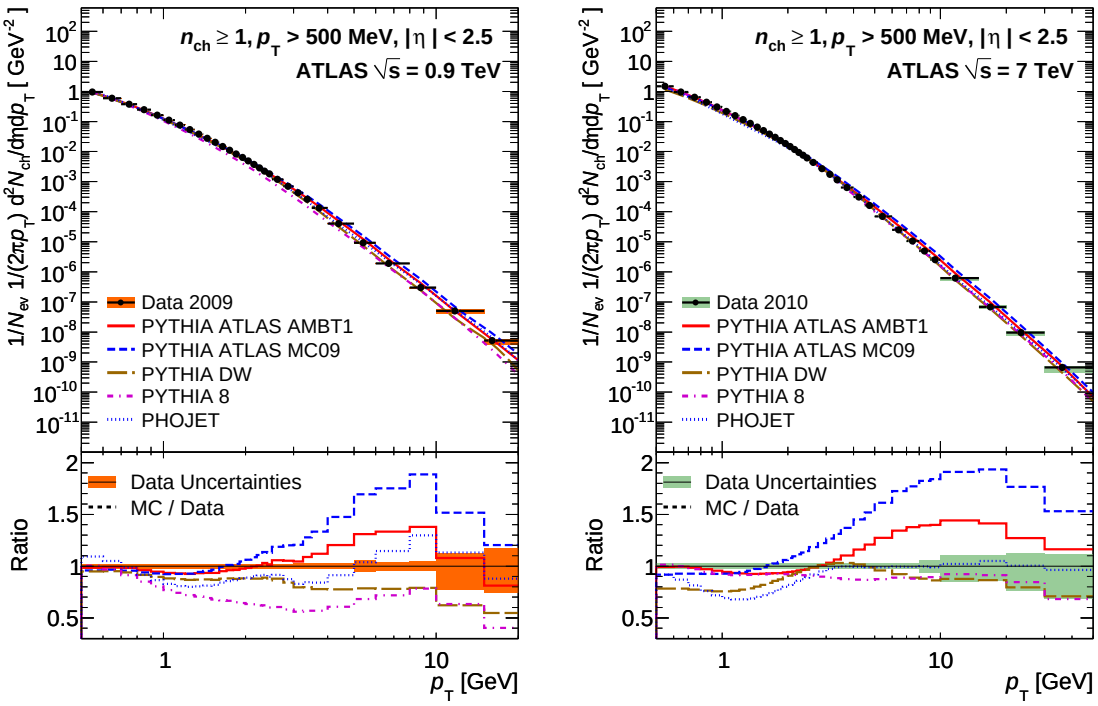

(a) (b)

Figure 7.3: Multiplicities as a function of the transverse momentum for events with $n_{\mathrm{ch}} \geq 1$, $p_{\mathrm{T}} > 500$ MeV and $|\eta| < 2.5$ at $\sqrt{s} = 0.9$ TeV(a) and $\sqrt{s} = 7$ TeV(b). The dots represent the data and the curves represent the predictions from different MC models. The vertical bars represent the statistical uncertainties, while the shaded areas show statistical and systematic uncertainties added in quadrature. The bottom inserts show the ratio of the MC over the data. The values of the ratio histograms refer to the bin centroids.

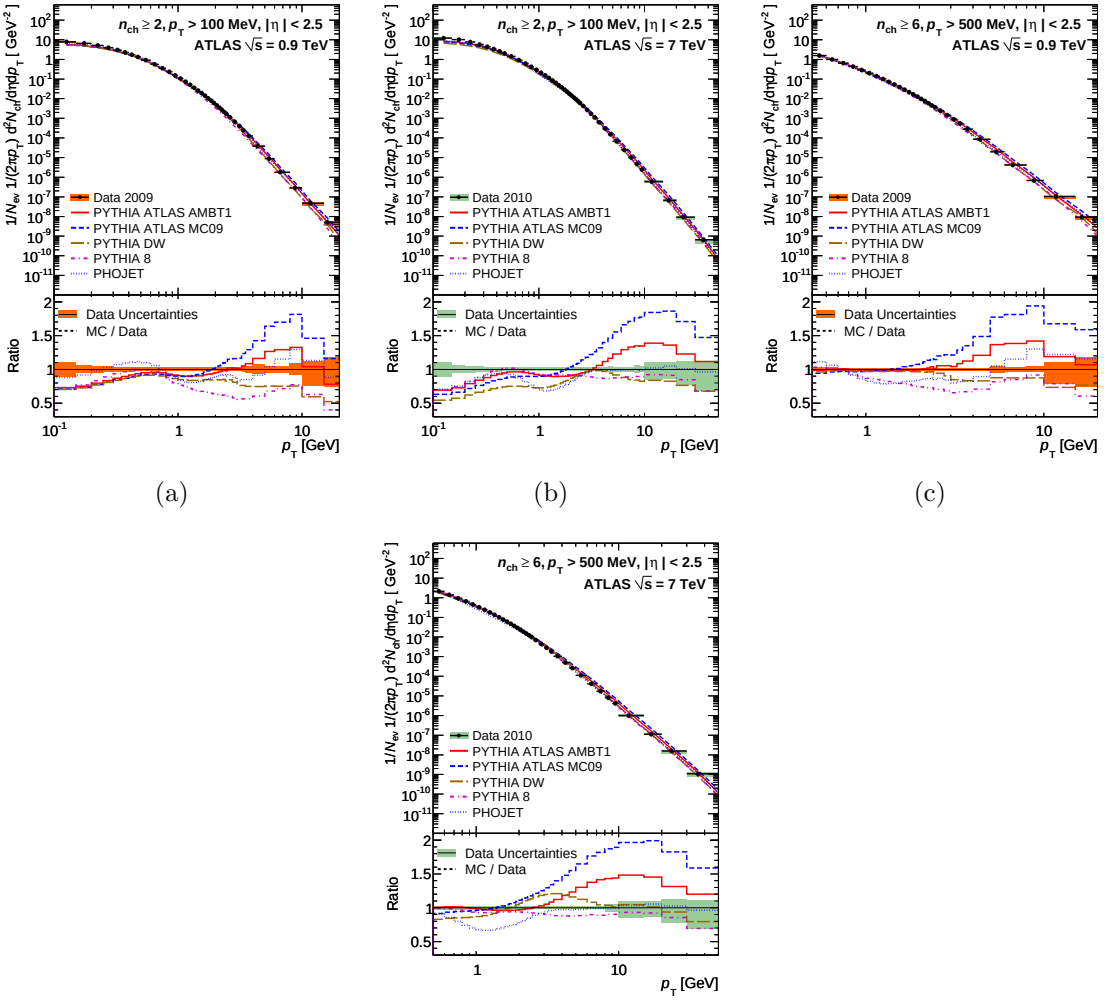

Figure 7.4: Multiplicities as a function of the transverse momentum for events with $n_{\mathrm{ch}} \geq 2$ $p_{\mathrm{T}} > 100$ MeV (a,b) and $n_{\mathrm{ch}} \geq 6$ (c,d), $p_{\mathrm{T}} > 500$ MeV and $|\eta| < 2.5$ at $\sqrt{s} = 0.9$ TeV (a,c) and $\sqrt{s} = 7$ TeV (b,d). The dots represent the data and the curves represent the predictions from different MC models. The vertical bars represent the statistical uncertainties, while the shaded areas show statistical and systematic uncertainties added in quadrature. The bottom inserts show the ratio of the MC over the data.

Figures 7.6(c) and 7.6(d) show the distribution for the most exclusive phase-space of $n_{\mathrm{ch}} \geq 3$, $p_{\mathrm{T}} > 500$ MeV and $|\eta| < 2.5$. The distributions are similar to those in Figure 7.5. But the normalization of the distributions differ between the two phase space selections due to the different number of charged particles requirement.

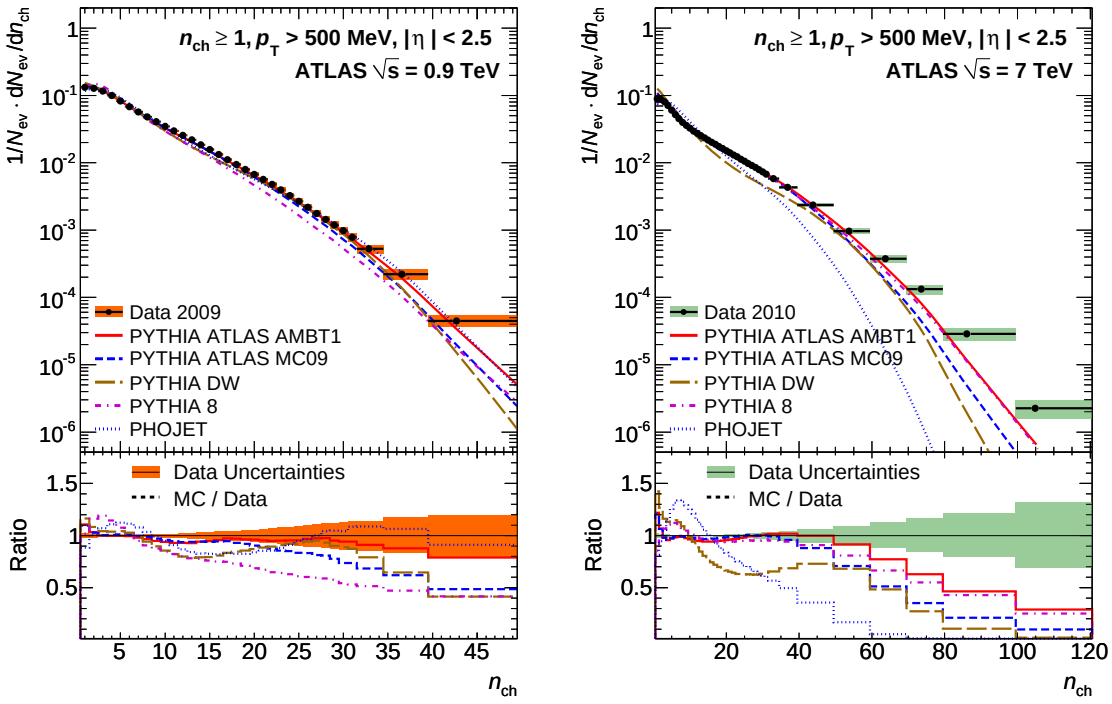

(a) (b)

Figure 7.5: Charged particle multiplicity distributions for events with $n_{\mathrm{ch}} \geq 1$, $p_{\mathrm{T}} > 500$ MeV and $|\eta| < 2.5$ at $\sqrt{s} = 0.9$ TeV (a) and $\sqrt{s} = 7$ TeV (b). The dots represent the data and the curves represent the predictions from different MC models. The vertical bars represent the statistical uncertainties, while the shaded areas show statistical and systematic uncertainties added in quadrature. The bottom inserts show the ratio of the MC over the data. The values of the ratio histograms refer to the bin centroids.

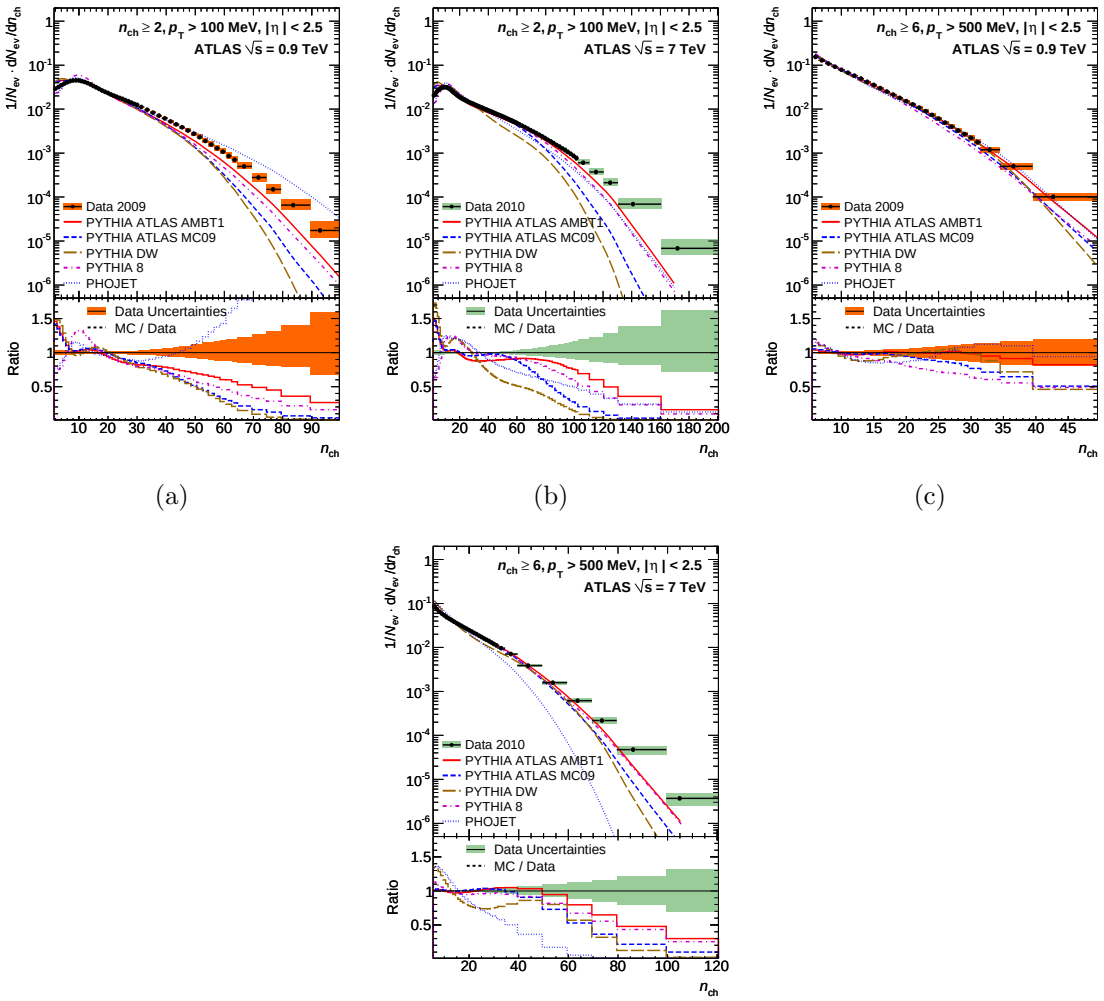

(a) (b) (c)

(d)

Figure 7.6: Multiplicity distributions for events with $n_{\mathrm{ch}} \geq 2$ $p_{\mathrm{T}} > 100$ MeV (a,b) and $n_{\mathrm{ch}} \geq 6$ (c,d), $p_{\mathrm{T}} > 500$ MeV and $|\eta| < 2.5$ at $\sqrt{s} = 0.9$ TeV (a,c) and $\sqrt{s} = 7$ TeV (b,d). The dots represent the data and the curves represents the predictions from different MC models. The vertical bars represent the statistical uncertainties, while the shaded areas show statistical and systematic uncertainties added in quadrature. The bottom inserts show the ratio of the MC over the data.

7.1.4 Average Transverse Momentum as a Function of the Number of Charged Particles

The distributions of average transverse momentum as a function of charged particle multiplicities, $< p_{\mathrm{T}} >$ vs. n_{ch}, for events with $n_{\mathrm{ch}} \geq 1$, $p_{\mathrm{T}} > 500$ MeV and $|\eta| < 2.5$ phase-space are shown in Figure 7.7. At 900 GeV, all the models describe the data relatively well for the slope at low number of charged particles. At the 7 TeV, none of the models agree with both slope and average p_{T}.

Figures 7.8(a) and 7.8(b) represent the average p_{T} distributions as a function of n_{ch}. PYTHIA8 agrees with data over the full range of n_{ch} for low center of mass energy. Furthermore, the AMBT1 has reasonably good agreement with the shape of the data distribution at high n_{ch}. All other MC models disagree with data throughout the region, specially at $\sqrt{s} = 7$ TeV.

7.1.5 $dn_{\mathrm{ch}}/d\eta$ at $\eta = 0$

The mean number of charged particles in the central pseudorapidity region can be calculated by averaging over $|\eta| < 0.2$. Table 7.1 and the Figure 7.9 [4] show the values of the mean number of charged particles in the central region for all three center-of-mass energies. Even though limited studies have been made using $\sqrt{s} =$ 2.36 TeV data I have included the values for that energy here. The result showed at $\sqrt{s} = 2.36$ TeV is the value obtained using the pixel track method.

For the most inclusive phase-space, none of the MC models have good agreement with data. The observed values in the most inclusive measurement are significantly

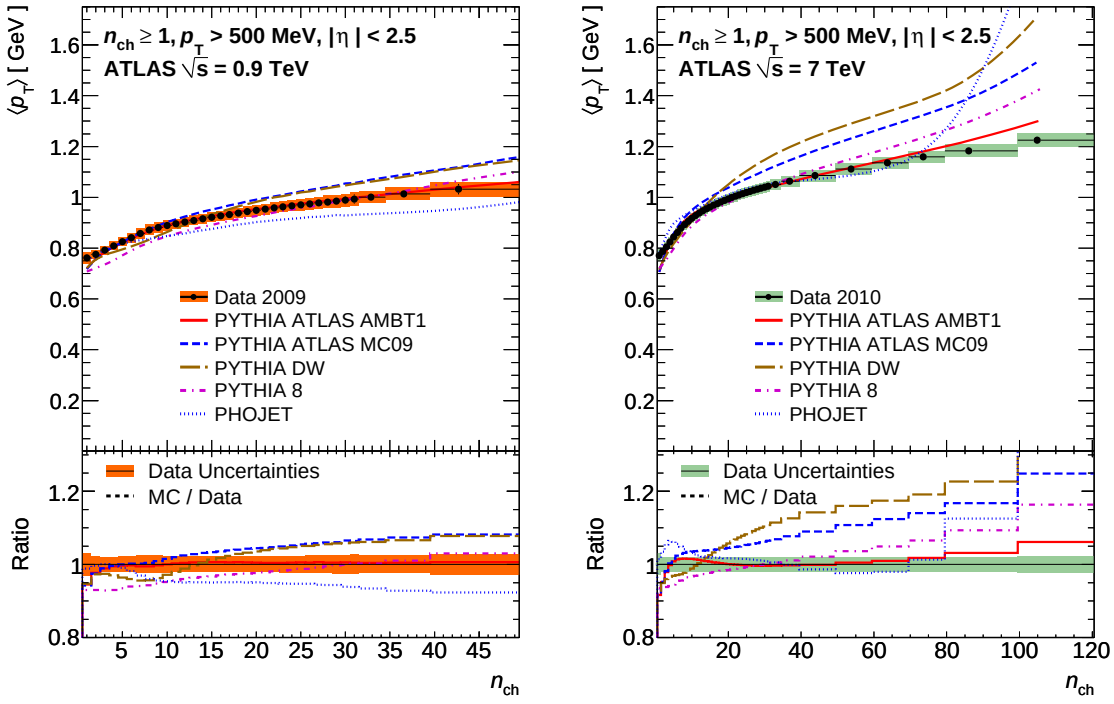

(a) (b)

Figure 7.7: Average transverse momentum as a function of the number of charged particles in the event for events with $n_{\mathrm{ch}} \geq 1$, $p_{\mathrm{T}} > 500$ MeV and $|\eta| < 2.5$ at $\sqrt{s} = 0.9$ TeV(a), and $\sqrt{s} = 7$ TeV(b). The dots represent the data and the curves the predictions from different MC models. The vertical bars represent the statistical uncertainties, while the shaded areas show statistical and systematic uncertainties added in quadrature. The bottom inserts show the ratio of the MC over the data. The values of the ratio histograms refer to the bin centroids.

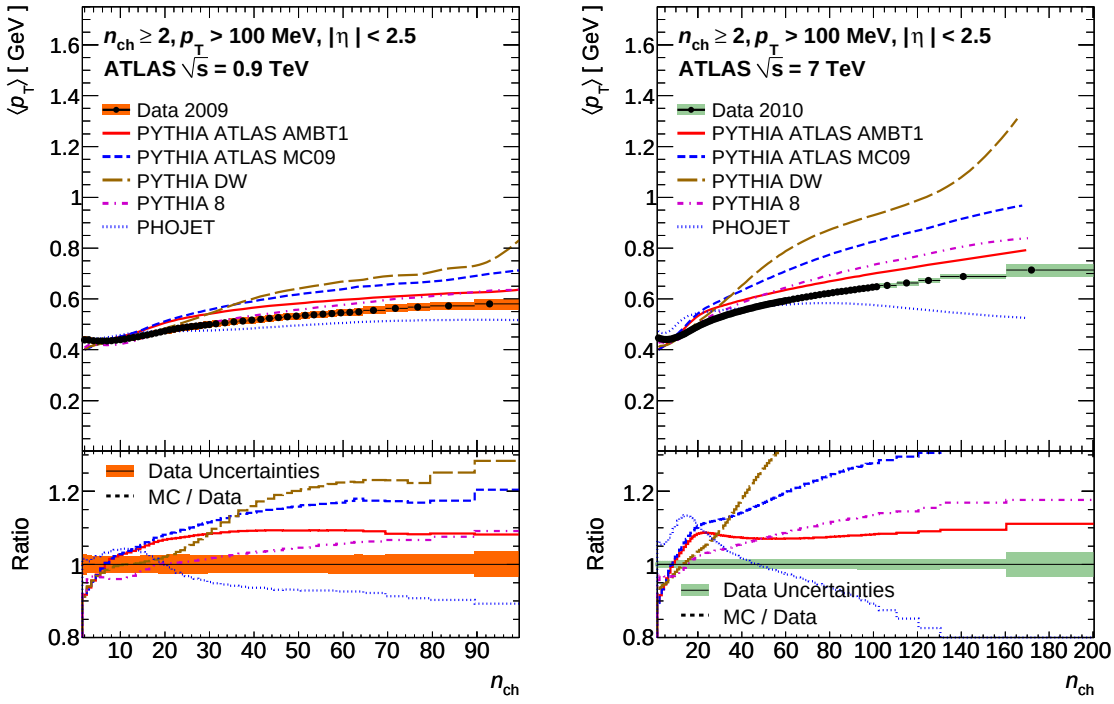

(a) (b)

Figure 7.8: Average transverse momentum as a function of the number of charged particles in the event for events with $n_{\mathrm{ch}} \geq 2$ $p_{\mathrm{T}} > 100$ MeV and $|\eta| < 2.5$ at $\sqrt{s} = 0.9$ TeV (a) and $\sqrt{s} = 7$ TeV (b). The dots represent the data and the curves the predictions from different MC models. The vertical bars represent the statistical uncertainties, while the shaded areas show statistical and systematic uncertainties added in quadrature. The bottom inserts show the ratio of the MC over the data. The values of the ratio histograms refer to the bin centroids.

higher than predicted values.

Phase-Space	Energy (TeV)	$dn_{ch}/d\eta$ at $\eta = 0$ Measured	PYTHIA6 AMBT1
$n_{ch} \geq 2$, $p_T > 100$ MeV	0.9	3.483 ± 0.009 (stat) ± 0.098 (syst)	3.01
	7	5.630 ± 0.003 (stat) ± 0.162 (syst)	4.93
$n_{ch} \geq 1$, $p_T > 500$ MeV	0.9	1.343 ± 0.004 (stat) ± 0.020 (syst)	1.28
	2.36	1.74 ± 0.019 (stat) ± 0.058 (syst)	1.70
	7	2.423 ± 0.001 (stat) ± 0.042 (syst)	2.36
$n_{ch} \geq 6$, $p_T > 500$ MeV	0.9	2.380 ± 0.009 (stat) ± 0.028 (syst)	2.33
	7	3.647 ± 0.006 (stat) ± 0.055 (syst)	3.63

Table 7.1: $dn_{ch}/d\eta$ at $\eta = 0$ for the three different phase-spaces considered in this paper for the energies where results are available. For MC, sufficient statistics are generated such that the statistical uncertainty is smaller than the last digit quoted.

7.1.6 Extrapolation to $p_T = 0$

The average number of charged particles with $p_T > 100$ MeV and the full range of $|\eta| < 2.5$ are calculated as the average of the multiplicity distribution. Figures 7.2(a) and 7.2(b) show the charged multiplicity functions that have to be used to compute the average number of charged particles.

The measured number of charged particles are found to be 3.614 ± 0.006 (stat) ± 0.163 (syst) at $\sqrt{s} = 0.9$ TeV and 5.881 ± 0.002 (stat) ± 0.268 (syst) at $\sqrt{s} = 7$ TeV. These values have been multiplied by the model-dependent scale factors obtained from section 6.2.11.1 and the corrected average number of inclusive charged particles for events with two or more particles are then found to be 3.831 ± 0.006 (stat) ± 0.177 (syst) at $\sqrt{s} = 0.9$ TeV and 6.160 ± 0.002 (stat) ± 0.287 (syst) at $\sqrt{s} = 7$ TeV.

These results are give the average total inelastic multiplicity for events with two

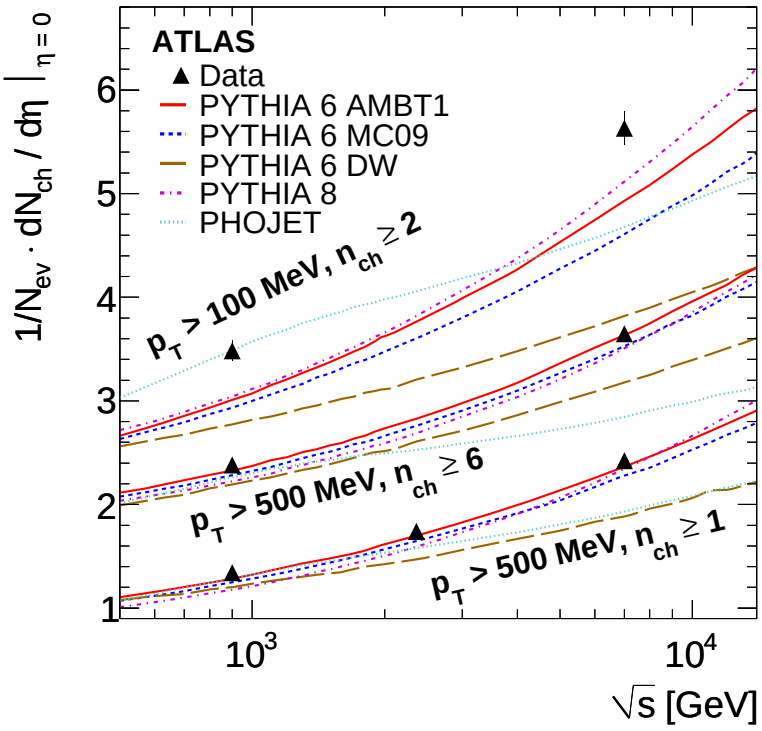

Figure 7.9: The average charged particle multiplicity per unit of rapidity for $\eta = 0$ as a function of the center-of-mass energy. The results with $n_{\mathrm{ch}} \geq 2$ within the kinematic range $p_{\mathrm{T}} > 100$ MeV and $|\eta| < 2.5$ are shown along-side the results with $n_{\mathrm{ch}} \geq 1$ within the kinematic range $p_{\mathrm{T}} > 500$ MeV and $|\eta| < 2.5$ at 0.9, 2.36 and 7 TeV. The data are compared to various particle level MC predictions.

or more particles within $|\eta| < 2.5$. Comparison plots with ALICE results [63, 64] with at least one charged particle are shown in Figure 7.10. The ALICE experiment has computed the values by averaging over $|\eta| < 1.0$ and $|\eta| < 0.5$, respectively.

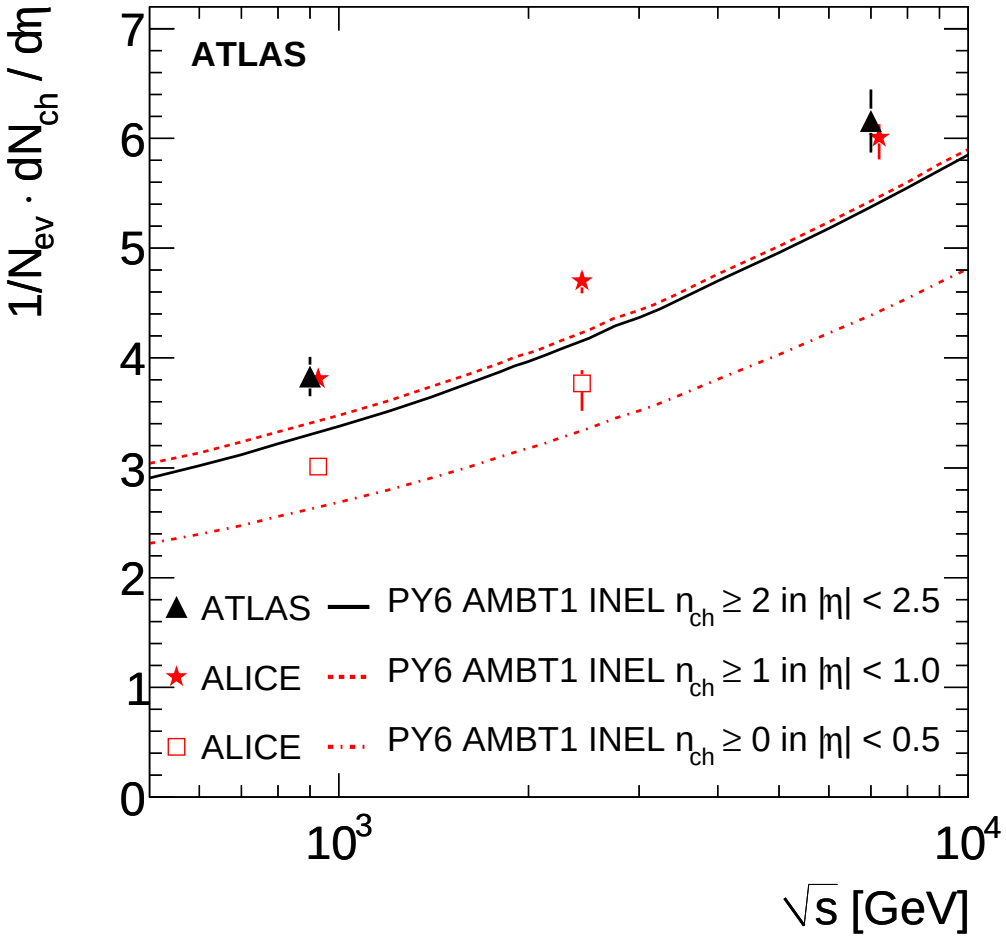

Figure 7.10: The average charged particle multiplicity per unit of rapidity as a function of the center-of-mass energy. The ATLAS results are for $n_{\text{ch}} \geq 2$ in the region $|\eta| < 2.5$. For comparison ALICE results for $n_{\text{ch}} \geq 1$ in the region $|\eta| < 1.0$ and $n_{\text{ch}} \geq 0$ in the region $|\eta| < 0.5$ are shown. It should be noted that the ALICE points have been slightly shifted horizontally for clarity.

7.2 New ATLAS tunes to 2010 data

Since the PYTHIA 6 MC generator is used as a main event generator for the ATLAS experiment, it is important to tune this generator using current measurements. Even though the PHOJET generator has a relatively good performance for minimum bias measurements it has not been tuned using the most recent LHC data.

Minimum bias and underlying events measurements are made using 2010 data and MC10 simulation. The MC10 simulation was produced by applying the PYTHIA 6 tune of AMBT1. After the minimum bias studies using the AMBT1 tune, two new sets of PYTHIA 6 tunes, AMBT2/AUET2, collectively known as A*T2 tunes [65] and AMBT2B/AUET2B, collectively known as A*T2B tune [66], were produced. The AMBT2 and AMBT2B tunes are dedicated to simulation of minimum bias events while the AUET2 and AUET2B tunes are tuned only for underlying events. The A*T2B tunes are currently used for the MC11 simulation campaign.

Both sets of tunes use the MRST LO** parton distribution functions (PDF) [67]. The LO**, as explained in Appendix B.4, is a modified leading order PDF similar to MRST LO* (see Appendix B.4) that was the one used in previous ATLAS MC09 and MC10 simulations. The LO** PDF uses p_{T}^2 as a scale for the evolution of α_s (as in Equation 2.4) while LO* uses Q^2, which is more conventional, as a scale for α_s evolution.

A*T2 tunes including the parton shower algorithm were performed using data from e^+e^- collisions as well as Tevatron, and ATLAS data. One of the main goals of these tunes is to understand the transverse jet shape discrepancy between CDF and

ATLAS. The ATLAS measurement of jet shape in events containing at least one jet above 20 GeV was too narrow compared to the AMBT1 tune. The Perugia 0 [36] tune also had the same issue when it was compared with Tevetron data. However, the Perugia 2010 tune [68] was developed to improve the description of the jet shape. The Perugia 2010 tune simulated the jet shapes in ATLAS data relatively well. Therefore, tuning of the initial state shower (ISR) and primordial k_T parameters is based on the strategy used for the Perugia 2010 tune.

The strong coupling constant in ISR is defined as $\alpha_s(kQ/\Lambda^2_{ISR})$ where the k is multiplication factor, and Λ_{ISR} is the QCD scale factor. Λ_{ISR} and k are specified by the PARP(61) and PARP(64) parameters respectively in PYTHIA. These tunes set the $\Lambda_{ISR} = 0.265$, which is the nominal value of Λ_{QCD} in MRST LO** PDF, very close to that of normal LO PDF. The previous tunes used $\Lambda_{ISR} = 0.192$, i.e the nominal value Λ_{QCD} in CTEQ5L LO PDF. This is one of the important changes that has been introduced in these tunes. The Λ_{QCD} value use to calculate the α_s in the final state radiation (FSR) showers starting from ISR partons is defined by Λ^{IFSR}_{QCD}. This is a important element from the point of jet shape and this is specified as PARP(72) in PYTHIA. The AMBT1 tune sets PARP(72) to the valued found by tuning to e^+e^-. "The new tunes set the PARP(72) value from hadronization since ATLAS tuning groups consider the jet shape description sufficiently important for ATLAS physics to tune this parameter explicitly to data from ATLAS and the Tevatron [65]." As a result, the ATLAS jet shape agreement is improved from 15% using the AMBT1 tune to 5% as shown in Figure 7.11(a). However, the jet shape in CDF, as shown in Figure 7.11(b), still has a 20% disagreement with data in some regions.

Adjusting the parameters affecting Multiple Parton Interactions (MPI) is the final stage of the ATLAS tuning process. One of the main parameters of MPI is the p_{T} cutoff parameter, which is used in PYTHIA to avoid soft divergence during the transformation from high-p_{T} to low-p_{T}partons. The reference p_{T} cutoff value of $\sqrt{s}$ = 1800 GeV, and its exponent that used in energy evolution to other beam energies are specified by PARP(82) and PARP(90) respectively. These both are tuned. Two other MPI parameters PARP(77) and PARP(78), which control the color reconnection probabilities for high-p_{T} are also tuned.

All the previous ATLAS tunes for ISR and MPI set $\Lambda_{QCD} = 0.192$, i.e the nominal value in CTEQ5L LO PDF, rather than the true value of the PDFs used. Therefore, ISR/MPI Λ_{QCD} value set to the true value of 0.265 of MRST LO** PDF. In addtion to theΛ_{QCD} values, several variations of fit weights were introduced before setting the final tune. It was found to be impossible to describe all the desired variables simultaneously in single tune. In particular, the MC-data descriptions of order 20% in the level of number of charged particles and $\sum p_{\mathrm{T}}$ are observed when the ATLAS minimum bias and underlying events are tuned together. Therefore, two distinct tunes of AMBT2 for minimum bias events and AUET2 for underlying events are produced. The major difference between these two tunes lie in the color recognition parameters PARP(77) and PARP(78). Furthemore, in the final stage of tuning, the production of observables required several extensions of initial ranges. Specially, minimum bias observables required PARP(82) and PARP(78) to be set to values beyond the upper and lower limits of initial ranges. Therefore, many more runs, 533, were generated and used for final tuning.

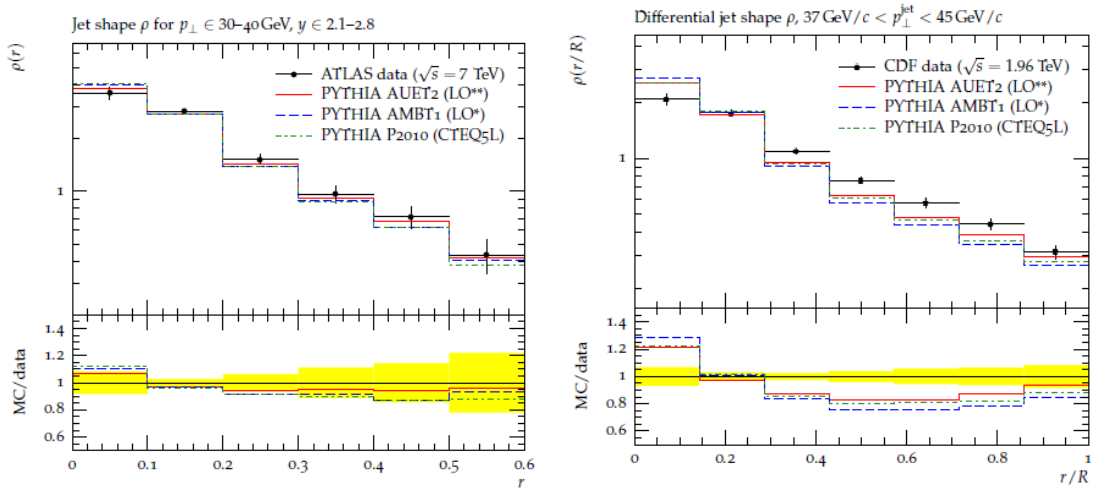

(a) (b)

Figure 7.11: Comparison plots of the new PYTHIA 6 AMBT2 tune to ATLAS minimum bias data at 7 TeV and 1.96 TeV of CDF.

The dedicated tuning for underlying events gives a good improvement over the AMBT1 tune. The charged particle multiplicities, in the low end of the spectrum, has good improvement using the AMBT2 tune compared to AMBT1, but high multiplicities are not described well in AMBT2. The AMBT2 tune doesn't provide an improvement of charged particle multiplicities in the very low-p_{T} region. Similarly, the descriptions of the p_{T} spectrum is more deviant in AMBT2 than the other tunes. By varying the MPI parameters and increasing the fit weight on the p_{T} does not help to improve the quality of the fit. The theory group suspected that the treatment of Λ_{QCD} in this tune causes these disagreements. Figures 7.11 and 7.12 [65] show some comparison plots for average transverse momentum, jet shape, charged particle multiplicities as a function of pseudorapidity.

AMBT2B/AUET2B are the updates of the A*T2 tunes. As discussed before,

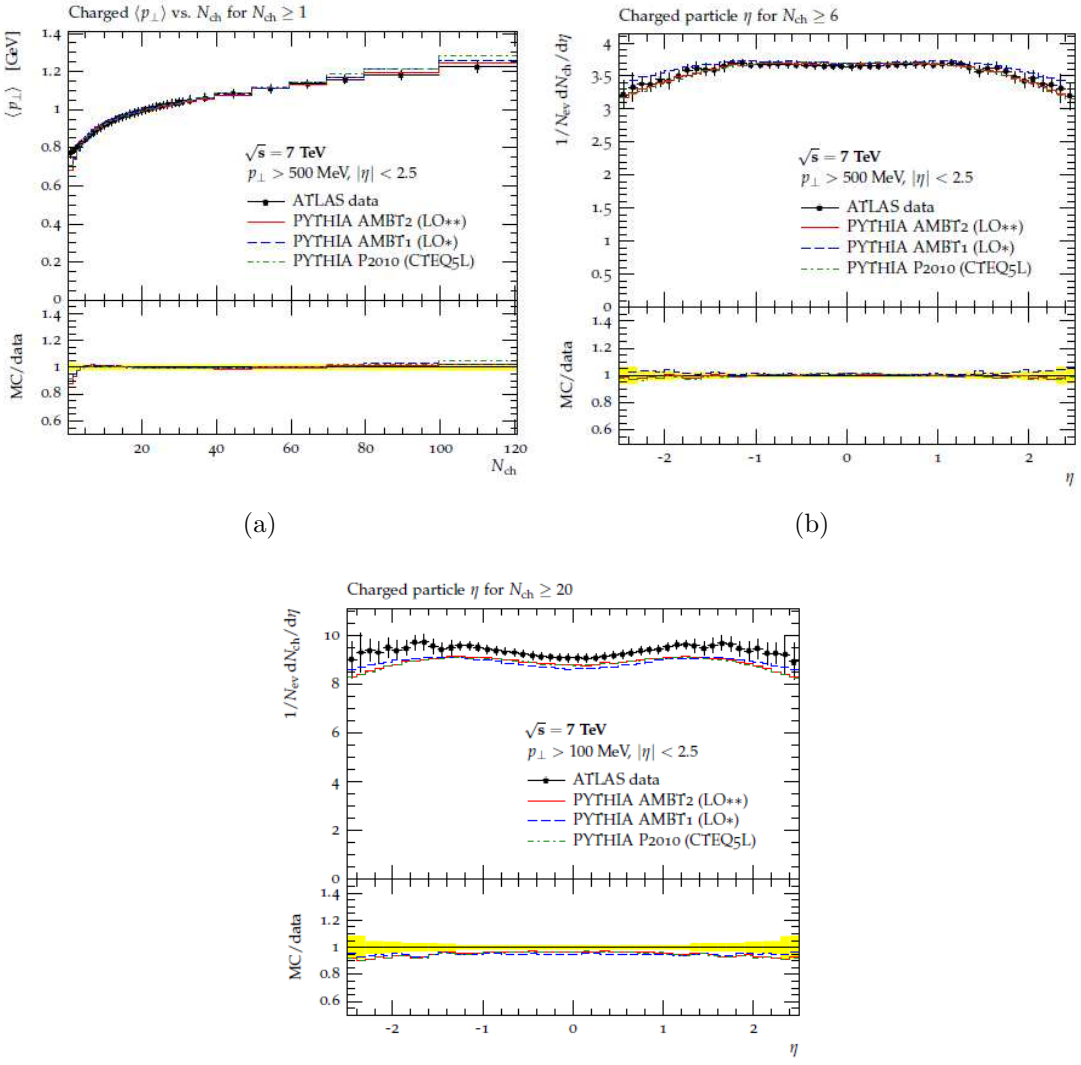

(a) (b)

(c)

Figure 7.12: Comparison plots of the new PYTHIA 6 AMBT2 tune to ATLAS minimum bias data at 7 TeV.

A*T2 tuning came to an end with some agreements and some disagreements with the data. A*T2B were constructed for a variety of PDFs, and they constitute alternatives to the A*T2 tunes for MC11 simulation. The new A*T2B re-tuning program was started right after the A*T2 tunes with the intention to provide an alternative single solution to PYTHIA 6 MC11 simulation. In these tunes, the parton shower setting was returned back to AMBT1-like configuration where the Λ_{QCD} value set explicitly to the default value for the CTEQ5L PDF of 0.192. This value differs from the true value of Λ_{QCD} for LO* (0.365) and LO** (0.265). Therefore, the coupling constant α_s in these tunes differs significantly between the different parts of showers. This change is the main difference between A*T2 and A*T2B. 5 flavor evolution of α_s is used in these tunes, and it is different from 4 flavor evolution in AMBT1. This is the primary difference between AMBT1 and A*T2B. Since 5 flavor evolution is always used in FSR this setting is a consistent flavor treatment for Λ_{QCD} in the different parts of shower code in PYTHIA. Most of the other tunings values in A*T2B are consistent with A*T2 tunes.

The A*T2B tunes are sensitive to different PDFs used as shown in Figures 7.13, 7.14, 7.15 and 7.16 [66]. AMBT2B tune using CTEQ6L1 produced a particularly a good agreement for minimum bias events as shown in Figures 7.14, 7.15 and 7.16, and it is recommended to be used for purely minimum bias simulation. The LO** PDF still remains the baseline PDF for ATLAS MC11 simulation. Similarly, the AUTE2B using LO** produces a reasonable description of underlying events, and AUTE2B with LO** PDF is recommended for underlying events in MC11 simulation. Further studies are currently going on to improve the current tuning for future simulations.

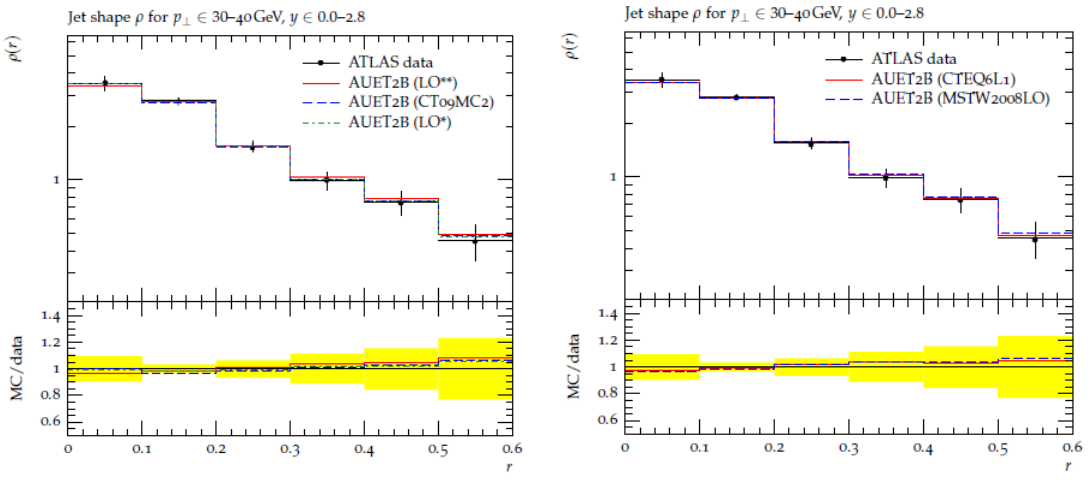

(a) (b)

Figure 7.13: Comparison plots of jet shape of the new PYTHIA 6 A*TB2 tune to ATLAS minimum bias data at 7 TeV.

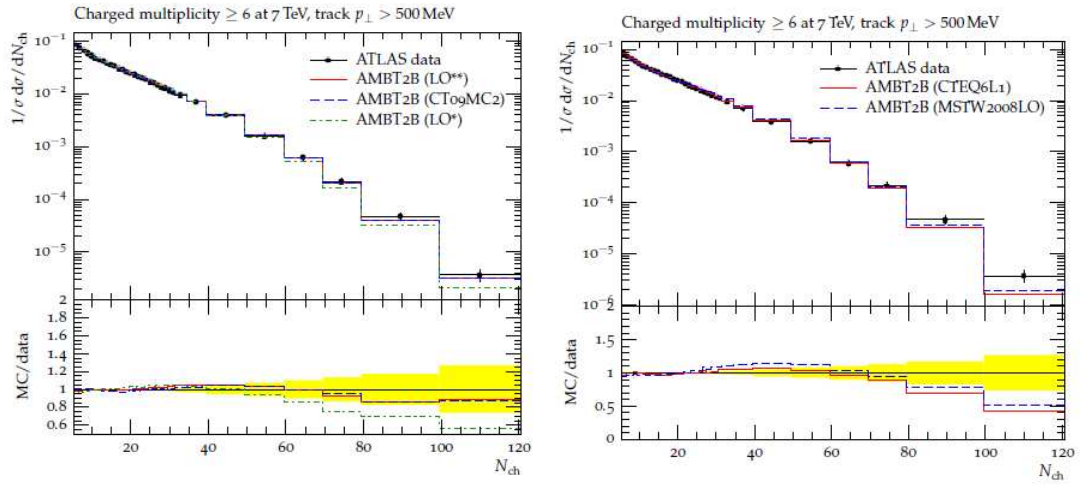

(a) (b)

Figure 7.14: Comparison plots of number of charged particles of the new PYTHIA 6 A*TB2 tune to ATLAS minimum bias data at 7 TeV.

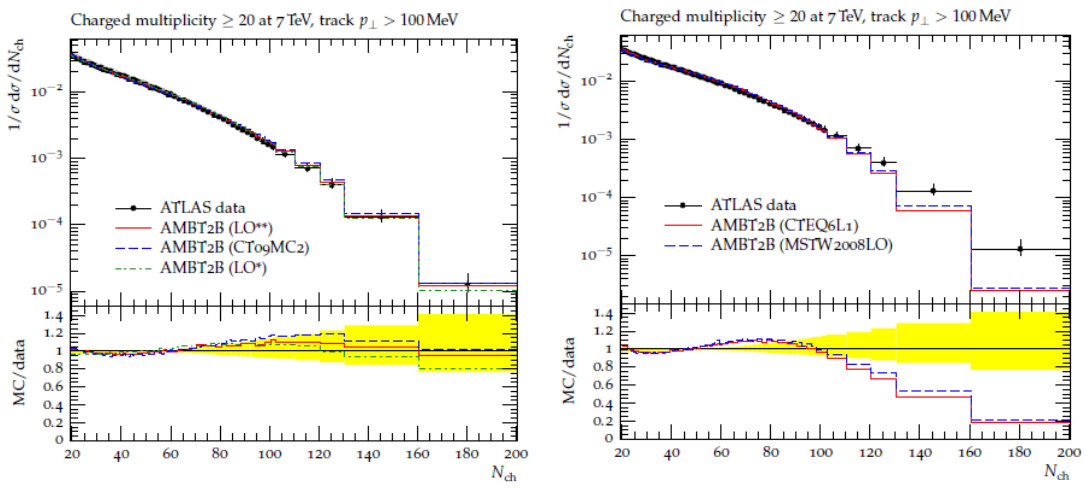

(a) (b)

Figure 7.15: Comparison plots of number of charged particles of the new PYTHIA 6 A*TB2 tune to ATLAS minimum bias data at 7 TeV.

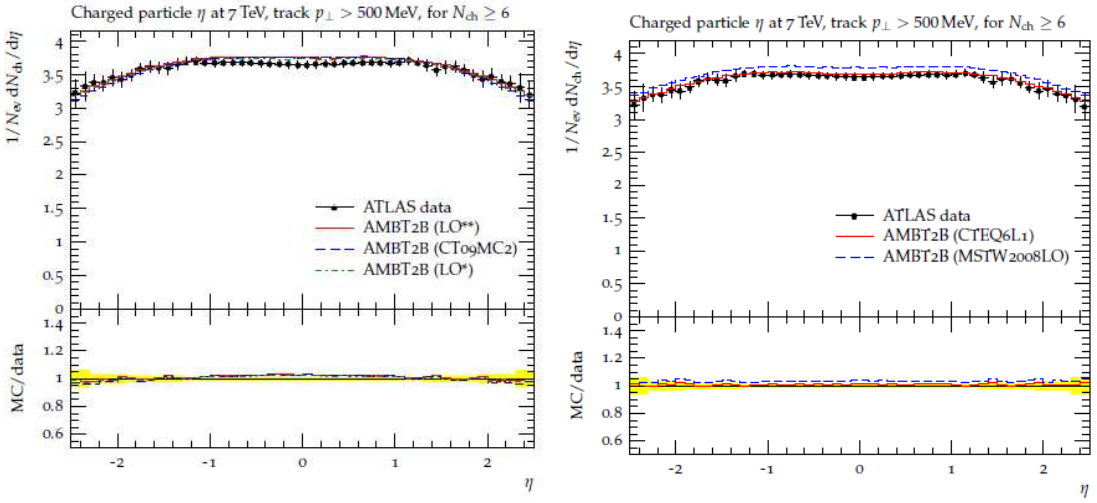

(a) (b)

Figure 7.16: Comparison plots of number of charged particles as function of pseudo-rapidity of the new PYTHIA 6 A*TB2 tune to ATLAS minimum bias data at 7 TeV.

7.3 Conclusions

Charged particle multiplicity distributions measured by the ATLAS detector at the LHC using the the first collisions recorded by the LHC during 2009 and 2010 are presented. The charged particle multiplicities were measured at three different center-of-mass energies: $\sqrt{s} = 0.9$ TeV, $\sqrt{s} = 2.36$ TeV and $\sqrt{s} = 7$ TeV. A limited analysis was made using the $\sqrt{s} = 2.36$ TeV data due to lack of statistics (there was only one run recorded in this energy.) Therefore, this thesis does not include much information about the analysis at this energy. Over ten million proton-proton inelastic interactions at $\sqrt{s} = 7$ TeV, just under six hundred thousand at $\sqrt{s} = 2.36$ TeV and over three hundred thousand at $\sqrt{s} = 0.9$ TeV were used to study the properties of events using three different phase-space selections.

In order to obtain the inclusive distributions of the charged particles the data were corrected with minimal MC model dependence. Tracks were reconstructed using all three ATLAS Inner detector components: Pixel (silicon pixel detector), SCT (Silicon Strip Detector) and TRT (Transition Radiation Tracker). Four different charged particle multiplicity distributions were measured: the charged particle multiplicity as a function of pseudorapidity, the charged particle multiplicity as a function of the transverse momentum, the charged particle multiplicity and the average transverse momentum as a function of the charged particle multiplicity.

There were several factors considered to compute corrections to the distributions including event selection efficiency, trigger efficiency, vertex reconstruction efficiency,

track reconstruction efficiency, non-primary estimation, etc. Each one of the above components were thoroughly studied to make the corrections accurate. The event selection efficiency was measured using the data. The tracking efficiency was calculated by Monte Carlo simulation. A detailed study was made to estimate the contribution of non-primary particles.

The selection of three different kinematic phase-spaces and the precision of this analysis showed a very clear difference between Monte Carlo model predictions and the measured distributions using data. The charged particle multiplicities in all three kinematic phase-spaces considered are higher than the prediction by Monte Carlo models. In general, the distributions using more exclusive phase-spaces, with a smaller contribution from diffractive events, have better agreement between data and the Monte Carlo models. Introducing these three different phase-spaces will allow the different components of Monte Carlo models to make further improvements.

The central charged particle multiplicity per event and unit of pseudorapidity, The charged particle multiplicity per event and unit of pseudorapidity at $\eta = 0$, for tracks with $p_{\mathrm{T}} > 100$ MeV (very inclusive region) is measured to be:
3.483 ± 0.009 (stat) $\pm$ 0.106 (syst) at $\sqrt{s} = 0.9$ TeV and
5.630 ± 0.003 (stat)$\pm$ 0.169 (syst) at $\sqrt{s} = 7$ TeV.

Two sets of new tunings were carried out after the minimum bias measurements. There are several improvements in charged particle multiplicities in the high transverse momentum region, but there are still some disagreements in the low-p_{T} region. Further studies are going on both PYTHIA 6 and PYTHIA 8 tunings.

Bibliography

[1] ATLAS Collaboration, G. A. et al., *Charged-particle multiplicities in pp interactions at $\sqrt{s}$ = 900 GeV measured with the ATLAS detector at the LHC*, Phys. Lett. **B688** (2010) 21–42.

[2] ATLAS Collaboration, G. A. et al., *Charged-particle multiplicities in pp interactions at $\sqrt{s}$ = 7 TeV measured with the ATLAS detector at the LHC*, . ATLAS-CONF-2010-024.

[3] ATLAS Collaboration, G. A. et al., *Consmic-Ray Detection Efficiencies for the ATlas Pixel Detector*, . ATLAS-PHYS-PUB-2009-000.

[4] ATLAS Collaboration, G. A. et al., *Charged particle multiplicities in pp interactions measured with the ATLAS detector at the LHC*, New J.Phys **13:053033** (2011) .

[5] C. A. et al., *Review of Particle Physics*, Phys. Lett. **B667** (2008) .

[6] C. Rubbia, *Experimental observation of the intermediate vector bosons W^+, W^-, and Z0*, Rev. Mod. Phys. **57** (1985) 699–722.

[7] C. W. Higgs, *Broken Symmetry and the Mass of Gauge Vector Mesons*, Phys. Lett. **12** (1964) 132–133.

[8] C. R. H. G. S. Guralnik and T. W. B. Kibble, *lobal Conservation Laws and Massless Particles*, Phys. Rev. Lett. **13** (1964) 585–587.

[9] F. Englert and R. Brout, *Broken Symmetry and the Mass of Gauge Vector Mesons*, Phys. Lett. **13** (1964) 321–322.

[10] V. D. Barger and R. J. N. Phillips, *Collider Physics. Frontiers in Physics. Addison-Wesley*, .

[11] S. Bethke, *The 2009 World Average of α_s(MZ)*, Eur. Phys. J **C64** (2009) 689–703.

[12] J. R. Forshaw and D. A. Ross, *Quantum Chromodynamics and the Pomeron*, Cambridge (1997) .

[13] L. Evans and P. Bryant, *THE CERN LARGE HADRON COLLIDER: ACCELERATOR AND EXPERIMENTS*, JINST **3:S08001** (2008) .

[14] G. A. et al., *The ATLAS Experiment at the CERN Large Hadron Collider*, JNIST **3:S08003** (2008) .

[15] CMS Collaboration, R. A. et al., *The CMS experiment at the CERN LHC*, JINST **3:S08004** (2008) .

[16] ATICE Collaboration, K. A. et al., *The ALICE experiment at the CERN LHC*, JINST **3:S08002** (2008) .

[17] LHCb Collaboration, A. A. A. et al., *The LHCb Detector at the LHC*, JINST **3:S08005** (2008) .

[18] ATLAS Collaboration, *ATLAS Inner Detector: Technical Design Repor*, .

[19] ATLAS Collaboration, *ATLAS Inner Detector: Technical Design Repor*, .

[20] ATLAS Collaboration, *ATLAS Level-1 Trigger Group. Level-1 Trigger Technical Design Report*, Technical Report (CERN/LHCC/98-14) .

[21] ATLAS Collaboration, G. A. et al., *ATLAS Pixel Detector Electronics and Sensors*, JINST **3:P07007** (2008) .

[22] ATLAS Collaboration, S. Strandberg, *Results from the commissioning of the ATLAS Pixel detector*, JINST **4:P03020** (2009) .

[23] ATLAS Collaboration, J. D. et al., *Commissioning of the ATLAS Pixel Optical Readout Link*, . ATLAS-INDET-INT-2010-012.

[24] ATLAS Collaboration, P. B. et al., *Threshold Tuning of the ATLAS Pixel Detector*, . ATL-COM-INDET-2010-044.

[25] ATLAS Collaboration, N. G. et al., *The Tuning and Calibration of the Charge Measurement of the Pixel Detector*, . ATL-COM-INDET-2010-017.

[26] ATLAS Collaboration, M. C. et al., *Monte Carlo Models for Minimum Bias Analysis at 900GeV*, . ATLAS NOTE.

[27] T. Sjostrand, S. Mrenna, and P. Skands, *PYTHIA 6.4 physics and manual*, JHEP **05** (2006) 026, `hep-ph/0603175`.

[28] R. Engel, *Phojet*, Z.Phys **C60** (1995) .

[29] A. Capella, *Dual Parton Model*, Surveys in High Energy Physics **16(3-4)** (2001) 175–186.

[30] A. Capella, U. Sukhatme, C.-I. Tan, and J. Tran Thanh Van, *Dual parton model*, Phys. Rep. **236** (1994) 225–329.

[31] A. Capella and J. T. T. Van, *Hadron-Nucleus Interactions and the Leading Particle Effect in a Dual-Parton Model*, Zeitschrift fr Physik C Particles and Fields **10** (1981) 249–262.

[32] V. M. Chudakov and V. V. Lugovoi, *Dual Parton Model of Inelastic pp Interactions and Cascade Breaking of String*, Z. Phys **C59(4-5)** (1993) 511–523.

[33] ATLAS Collaboration, Z. Marshall, *The ATLAS simulation software*, . ATL-SOFT-PROC-2008-001.

[34] GEANT4 Collaboration Collaboration, S. A. et al., *GEANT4: A simulation toolkit*, Nucl. Instr. Meth. **A506** (2003) 250–303.

[35] T. A. et al., *Tevatron-for-LHC Report of the QCD Working Group*, .

[36] P. Z. Skands, *The Perugia Tunes*, `arXiv:0905.3418`. arXiv:0905.3418.

[37] ATLAS Collaboration, G. A. et al., *ATLAS Monte Carlo Tunes for MC09*, . ATL-PHYS-PUB-2010-002.

[38] T. A. et al., *Measurement of Particle Production and Inclusive Differential Cross Sections in $p\bar{p}$ Collisions at $\sqrt{s}$ = 1.96 TeV*, Phys. Rev **D79** (2009) .

[39] ATLAS Collaboration, G. A. et al., *Charged particle multiplicities in pp interactions for track p_T > 100 MeV at $\sqrt{s}$ = 0.9 and 7 TeV measured with the ATLAS detector at the LHC*, . ATLAS-CONF-2010-046.

[40] G. Piacquadio, K. Prokofiev, and A. Wildauer, *Primary vertex reconstruction in the ATLAS experiment at LHC*, J. Phys. Conf. Ser. **119** (2008) 032033.

[41] ATLAS Collaboration, T. C. et al., *The new ATLAS track reconstruction (NEWT)*, J. Phys. Conf. Ser. **119** (2008) 032014.

[42] ATLAS Collaboration, G. A. et al., *Charged particle multiplicities in pp interactions at $\sqrt{s}$ = 0.9 and 7 TeV in a diffractive limited phase space measured with the ATLAS detector at the LHC and a new PYTHIA6 tune*, . ATLAS-CONF-2010-031.

[43] T. C. et al., *Concepts, Design and Implementation of the ATLAS New Tracking (NEWT)*, ATL-SOFT-PUB-2007-007, 2007.

[44] ATLAS Collaboration, T. C. et al., *Single track performance of the inner detector new track reconstruction (NEWT)*, . ATL-INDET-PUB-2008-002.

[45] ATLAS Collaboration, J. A. et al., *Track Reconstruction Efficiency in 900 GeV Data*, . ATL-COM-INDET-2010-010.

[46] ATLAS Collaboration, G. A. et al., *Track Reconstruction Efficiency in $\sqrt{s}$ = 7 TeV Data for Tracks with p_T > 100 MeV*, . ATL-PHYS-INT-2011-001.

[47] CMS Collaboration, V. Khachatryan et al., *Transverse momentum and pseudorapidity distributions of charged hadrons in pp collisions at $\sqrt{s}$ = 0.9 and 2.36 TeV*, JHEP **02** (2010) 041, arXiv:1002.0621 [hep-ex].

[48] ALICE Collaboration, K. A. et al., *First proton–proton collisions at the LHC as observed with the ALICE detector: measurement of the charged particle pseudorapidity density at $\sqrt{s}$ = 900 GeV*, Eur. Phys. J. **C65** (2010) 111–125, arXiv:0911.5430 [hep-ex].

[49] E735 Collaboration, T. A. et al., *Multiplicity dependence of transverse momentum spectra of centrally produced hadrons in $\bar{p}p$ collisions at 0.3 TeV, 0.54 TeV, 0.9 TeV, and 1.8 TeV center of mass energy*, Phys. Lett. **B336** (1994) 599–604.

[50] UA1 Collaboration, C. A. et al., *A Study of the General Characteristics of $p\bar{p}$ Collisions at $\sqrt{s}$ = 0.2 TeV to 0.9 TeV*, Nucl. Phys. **B335** (1990) 261.

[51] CDF Collaboration, F. A. et al., *Pseudorapidity distributions of charged particles produced in $\bar{p}p$ interactions at $\sqrt{s}$ = 630 GeV and 1800 GeV*, Phys. Rev. **D41** (1990) 2330.

[52] UA5 Collaboration, R. A. et al., *Charged particle multiplicity distributions at 200 and 900 GeV c.m. energy*, Z. Phys. **C43** (1989) 357.

[53] UA5 Collaboration, R. A. et al., *Charged particle correlations in $p\bar{p}$ collisions at c.m. energies of 200, 546, and 900 GeV*, Z. Phys. **C37** (1988) 191–213.

[54] CDF Collaboration, F. A. et al., *Transverse momentum distributions of charged particles produced in $\bar{p}p$ interactions at $\sqrt{s}$ = 630 GeV and 1800 GeV*, Phys. Rev. Lett. **61** (1988) 1819.

[55] UA5 Collaboration, G. J. A. al., *UA5: A general study of proton-antiproton physics at $\sqrt{s}$ = 546 GeV*, Phys. Rept. **154** (1987) 247–383.

[56] UA5 Collaboration, R. E. A. et al., *Diffraction dissociation at the CERN pulsed $p\bar{p}$ collider at c.m. energies of 900 and 200 GeV*, Z. Phys. **C33** (1986) 175.

[57] ABCDHW Collaboration, A. B. et al., *Charged Multiplicity Distribution in pp Interactions at ISR Energies*, Phys. Rev. **D30** (1984) 528.

[58] UA1 Collaboration, G. A. et al., *Transverse Momentum Spectra for Charged Particles at the CERN Proton anti-Proton Collider*, Phys. Lett. **B118** (1982) 167.

[59] ATLAS Collaboration, S. A.-S. et al., *Vertex reconstruction for analysis of charged particle multiplicities in pp interactions at $\sqrt{s}$ = 900 GeV* , . ATL-COM-INDET-2010-009.

[60] ATLAS Collaboration, G. I. B. et al., *Correction of Track to Charged Particle Distributions in pp Interactions at $\sqrt{s}$ 900 GeV*, . ATL-COM-PHYS-2010-038.

[61] G. D'Agostini, *A Multidimensional unfolding method based on Bayes' theorem*, Nucl. Instr. Meth. **A362** (1995) 487–498.

[62] C. Tsallis, *Possible Generalization of Boltzmann-Gibbs Statistics*, J. Stat. Phys. **52** (1988) 479–487.

[63] ALICE Collaboration, K. A. et al., *First proton-proton collisions at the LHC as observed with the ALICE detector: measurement of the charged particle pseudorapidity density at* $\sqrt{s} = 900\ GeV$, Eur. Phys. J. **C65** (2010) 111–125, `arXiv:0911.5430 [hep-ex]`.

[64] ALICE Collaboration, K. A. et al., *Charged-particle multiplicity measured in proton-proton collisions at* $\sqrt{s} = 7\ TeV$ *with ALICE at LHC*, 2010.

[65] ATLAS Collaboration, G. A. et al., *New ATLAS event generator tunes to 2010 data*, . ATL-PHYS-PUB-2011-008.

[66] ATLAS Collaboration, G. A. et al., *ATLAS tunes of PYTHIA6 and Pythia 8 for MC11*, . ATL-PHYS-PUB-2011-009.

[67] A. Sherstnev and R. Thorne, *Parton Distributions for LO Generators*, Eur.Phys.J **C55** (2008) 553–575.

[68] P. Z. Skands, *Tuning Monte Carlo Generators: The Perugia Tunes*, Phys. Rev. **D82** (2010) .

Appendix A

A.1 ATLAS Coordinate System

The ATLAS coordinate system describes the ATLAS detector and the particles emerging from the p-p collisions. This is a right handed cordinate system in which the nominal interaction point is define as the origin. The z-axis lies along the beam direction, and x-y plane is transverse plane to the beam direction (z-axis). The positive x-axis is pointing towards to the center of the LHC ring and positive y-axis is pointing upward direction. The positve z-axis towards the A side of the detector. The azimuthal angle ϕ is mesured around beam axis, clockwise, and the polar angle θ is meaured from the z-axis. The pseudorapidity is defined by: $\eta = -ln\ tan(\frac{\theta}{2})$ The transverse momentum p_{T}, the transverse energy E_T, and the missing transverse energy E_T^{miss} are defined in x-y plane. The distance ΔR in the $\eta - \phi$ angle space is given by: $\Delta R = \sqrt{\Delta\eta^2 + \Delta\phi^2}$.

Appendix B

B.1 χ^2 probability

The χ^2 is given by:

$$\chi^2 = \sum_i^n \frac{r_i^2}{\sigma_i^2}$$

where r_is are hit residuals: the difference between measurement position (hit) and the position predicted by track at every measurement surface, and σ_is are their errors. The probability density function for the χ^2 distribution with n degrees of freedom is given by:

$$p(\chi^2, n) = \frac{\int_{\chi^2}^{\infty}(t)^{\frac{n}{2}-1}e^{-n/2}dt}{2^{n/2}\Gamma(n/2)}$$

where the gamma function is given by:

$$\Gamma(x) = \int_0^{\infty} t^{x-1}e^{-t}dt$$

In ROOT, there is a special class for χ^2 probability p(χ^2, n).

B.2 Pile-Up Removal

The influence of multiple interactions inside a single event could bias the measurement of charged particle multiplicities. These types of events are removed where events with a second vertex with four or more tracks. The observed number of tracks at the second vertex (red), and the expected number of tracks at the second vertex if there was a real second interaction in the vertex (black) are shown in Figure B.1. The distribution of the expected number of tracks is obtained by considering events with only one vertex and adding on top another interaction according to that same distribution. These two vertices are then ordered according to their $\sum p_{\mathrm{T}}^2$. This shows that second vertices with two or three tracks are mostly from secondary interactions and fake vertices [2].

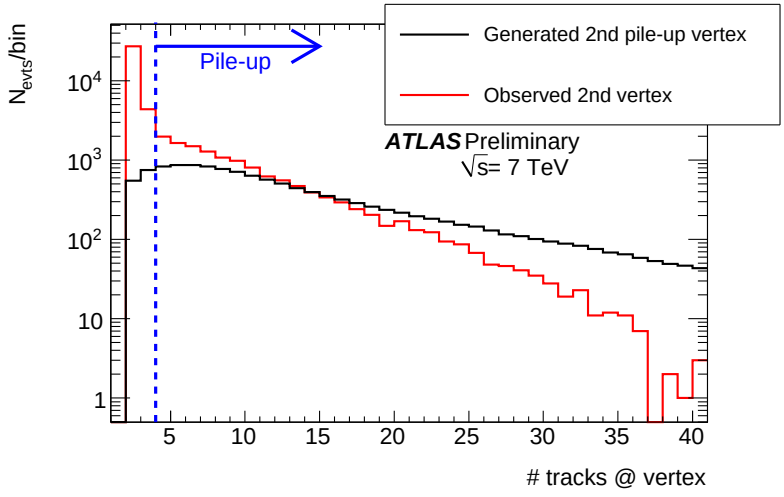

Figure B.1: The number of tracks associated to the second vertex (red) compared to the prediction for real second vertices (black). The blue line represents the cut applied

B.3 p_{T} Unfolding Procedure

The unfolding procedure used in the analysis is based on Bayes' Theorem. The complete theoretical and practical details of this procedure are explained in [61].

This method requires the measured data parameters as input, as well as some 'best guess' of the true distribution. However, the dependency on this initial probability distribution can be overcome by an iterative procedure. For this analysis, the p_{T} spectrum of a minimum bias MC, composed of a mixture of non-diffractive, single-diffractive, and double-diffractive events from PYTHIA 6 MC09, has been used as the "training" input distribution. The uncertainty associated to this choice of initial probabilities is evaluated as a systematic uncertainty [2].

The unfolding program also requires a migration matrix, relating the measured p_{T} of the reconstructed tracks to the true p_{T}. This matrix is then populated using the same PYTHIA minimum bias MC sample as used in the rest of the analysis. In addition to minimum bias MC sample, a combination of single-particle pion, Kaon and proton samples in the range 10 MeV $< p_{\mathrm{T}} <$ 100 GeV is also added in order to populate all kinematical regions and to ensure that the MC statistics exceeds as much as possible the statistics in data.

In order to calculate the migration matrix, a 2-D histogram of $p_{\mathrm{T}}^{\mathrm{gen}}$ vs. $p_{\mathrm{T}}^{\mathrm{corr\ reco}}$ is first filled for all well-matched reconstructed tracks after passing all the track selection cuts and corrections [2]. Then, each column of $p_{\mathrm{T}}^{\mathrm{corr\ reco}}$ is normalized by its sum in order to keep the number of reconstructed tracks constant before and after the unfolding procedure. Figure B.2 [2] shows the normalized migration matrix used for

the p_{T} unfolding procedure.

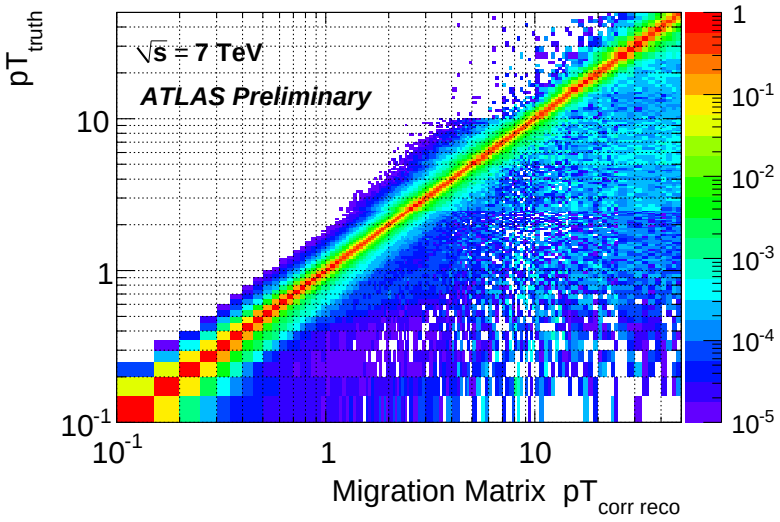

Figure B.2: Migration matrix used for the iterative p_{T} unfolding procedure in the measured range 0.1–100 GeV. The figure shows the generated charged particle p_{T} on the y-axis and the corrected, reconstructed track p_{T} on the x-axis for all well-matched reconstructed tracks in selected events passing the track selection cuts and weighted by the track- and event-level corrections. The matrix is populated using a combination of MC09 PYTHIA6 Monte Carlo and fully-simulated single-particle pion, Kaon and proton samples. Kaons and protons are scaled to 10% of their original size.

Figure B.3 shows the change in the measured p_{T} spectrum in data due to this unfolding procedure at both energies. The maximum size of the correction is of the order of 10%.

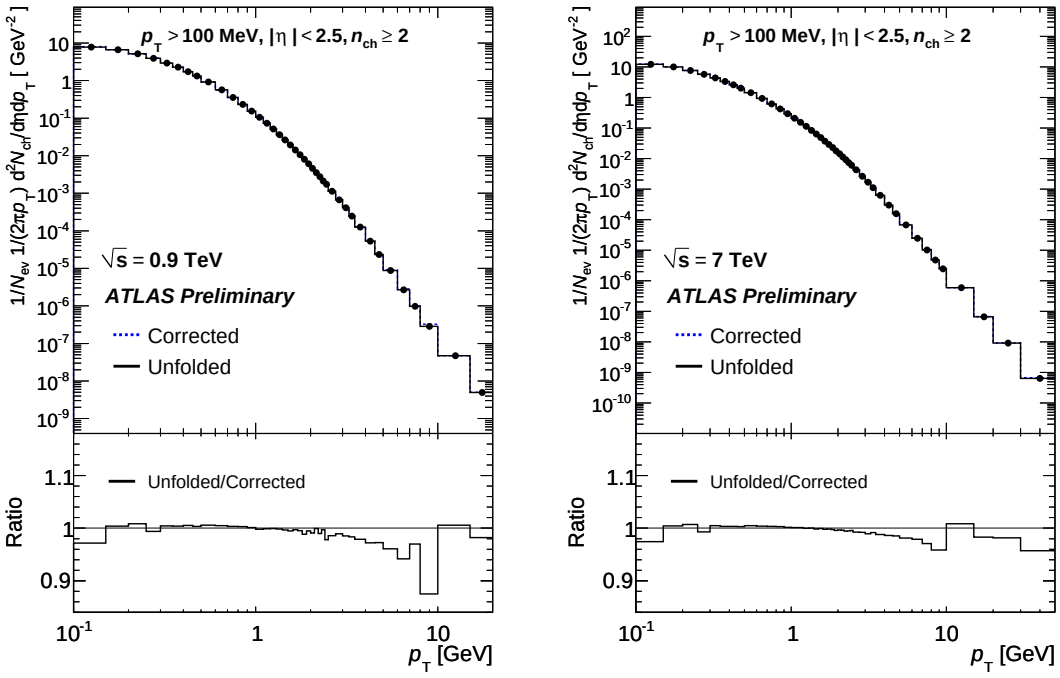

(a) (b)

Figure B.3: p_{T} spectrum before (blue) and after (black) the p_{T} unfolding procedure at $\sqrt{s} = 0.9$ TeV (a) and $\sqrt{s} = 7$ TeV (b). All other corrections have been applied in both cases. The bottom insert shows the ratio of the distributions after over before the unfolding.

B.4 New LO* and LO** Parton Distribution Functions

It is well known by theoretical groups that PDFs extracted at different orders of perturbative QCD have large differences in certain region of distance x. There are two main reasons for these difference: due to the missing higher order corrections in the splitting function between gluon and quarks, and in the cross-sections governing their extraction by comparison to experimental data (mainly from structure functions in deep inelastic scattering). Therefore, due to the large changes in parton distribution, the combinations of parton distribution functions and their accompanying matrix element are important during the cross-section calculation for any physical process [67]. Even though, LO PDFs are supposed to be the automatic choice for use with LO matrix elements (MEs) since those are available in many LO Monte Carlo programs it has been suggested that NLO PDFs may be more appropriate. The main reason for this idea is the claim that NLO cross-section corrections are small, and the main change in the total cross-section changes in going from LO to NLO due to differences in PDFs. Therefore, a new approach was carried out which combines the advantages of both LO and NLO PDFs. First, the α_s of NLO used in LO fit to parton distribution. This modification compensates the lack of partons in LO PDF. Another modification was made to relax the momentum sum rule (summing the momentum of partons) by requiring the automatic momentum conservation of partons. This makes the LO partons more like NLO partons. These modification is called LO* PDFs. These modifications improves the quality of the LO global fit.

After the first set of modifications on LO PDFs (LO* PDFS), another modification was made on LO* PDFs. The standard QCD scale Q^2 was replaced by p_T^2 ($= z(1-z)Q^2$) in α_s dependence on the QCD in quark-gluon splitting function (freezing $\alpha_s(p_T^2)$ at 0.5 as $z \to 1$),i.e change in the scale of α_s for higher distance (x) evolution. This modification is know as LO** PDFs.

Appendix C

C.1 Data and Monte Carlo Samples

900 GeV data were selected for the previous analysis with $p_{\mathrm{T}} > 500$ MeV [5]. In this analysis, the primary vertex is reconstructed using a beam spot constraint. Luminosity blocks (LB) were selected with a stable beam. The luminosity blocks with no beam spot are excluded. In 7 TeV runs, the LBs were selected by requiring all inner tracking detectors to flagged as green in the offline data quality monitor.

Lists of both 900 Gev and 7 TeV runs with LBs are shown in Tables C.2 and C.1 repectively.

For 7 TeV data, a total of 10,066,072 events passed all event selection cuts, and 209,809,430 tracks were selected after all track selection cuts. There were a total of 357,523 passed events in 900 GeV data with 4,532,663 selected tracks.

Around 10 million MC events were used for 900 GeV with the baseline of mc09_900GeV.105001.py
In the 7 TeV case, around 40 million MC events were produced

Run	Luminosity Block
152166	206-300
152214	159-202
152221	5-167
152345	128-207
152409	124-716
152441	309-671
152508	196-261

Table C.1: Data runs and good luminosity blocks used for comparisons of tracking quantities between data and simulation for $\sqrt{s} = 7$ TeV runs.

Run	Luminosity Block
141749	22-100
141811	126-165
142149	65-87
142154	22-35
142165	134-257
142166	38-96
142171	217-229
142174	8-47
142189	140-147
142191	7-36, 141-233
142193	33-153
142195	11-54
142383	260-282

Table C.2: Data runs and good luminosity blocks used for comparisons of tracking quantities between data and simulation for $\sqrt{s} = 0.9$ TeV runs.